Eivind Nicolay Dybdahl

Structural and temporal evolution of the Porsgrunn-Kristiansand Fault Complex

Master's thesis in Geologi Master
Supervisor: Espen Torgersen, Per Terje Osmundsen
June 2023

NTNU
Norwegian University of
Science and Technology

Eivind Nicolay Dybdahl

Structural and temporal evolution of the Porsgrunn-Kristiansand Fault Complex

Master's thesis in Geologi Master
Supervisor: Espen Torgersen, Per Terje Osmundsen
June 2023

Norwegian University of Science and Technology
Faculty of Engineering
Department of Geoscience and Petroleum

NTNU
Norwegian University of
Science and Technology

Abstract

The bedrock in southern Norway is old (>900Ma) and is saturated with brittle deformation. One of the most notable structures is the 150 km long Porsgrunn-Kristiansand Fault Complex (PKFC) that presently limits the Bamble Lithotectonic Unit to the NW. Although the PKFC is a well-known structure, little structural data is available. This study therefore aims at characterizing the structural architecture and evolution of the PKFC, using structural analysis and K-Ar geochronology.

The studied section of the PKFC is marked by an undulating, steep (dip: 62 ± 2°), ESE-dipping fault plane (strike: 32 ± 2°). It consists of a high strain fault core bounded by damage zones, with the hanging wall and footwall damage zones having a thickness of 370 - 510 m and 60 - 280 m, respectively. The fault core is a 2.5 - 5 m thick composite brittle structure comprised of 12 juxtaposed, but not coeval, brittle structural facies. The fault core has a fracture frequency exceeding 40 fractures per m^3 and the increased amount of fractures have produced enhanced permeability in the damage zones and part of the fault core. This has caused an increase in hydrothermal alteration with chloritic alteration of biotite and precipitation of carbonate veins occurring frequently.

Age data from the K-Ar geochronology shows that the studied section of the PKFC has experienced significant displacement through several phases of slip in the Mesozoic era, lasting from middle Triassic to early Cretaceous. To conclude the order of formation, a common early faulting event produced a wider zone of deformation, resulting in a coarse grained fault breccia (c. 227 - 224 Ma). Later structural facies 3 (SF3) was formed (<221 Ma), followed by SF7 (<193 Ma), SF9 (152 Ma) and SF8 (122 Ma). Furthermore, an earlier cataclasite forming slip-phase has been uncovered along the studied section of the PKFC, which has tentatively been linked to the post-Sveconorwegian extensional regime and orogenic collapse. Kinematic indicators suggest a strike-slip oriented slip movement during the earlier cataclasite forming slip-phase and a dip-slip oriented slip movement during the later Mesozoic phases of slip.

Finally, a combination of automatic lineament analysis and comparison between resulting K-Ar ages with ages obtained from cross-cutting relationships in the Porsgrunn area suggest that the PKFC consists of two segments; one northern segment, located south of Porsgrunn and one southern segment, located north of Kristiansand. The northern and southern segments are c. 24 km and c. 70 km long, respectively, and both have an approximately NE-SW orientation.

Sammendrag

Berggrunnen i Sør-Norge er gammel (>900 Ma) og sprø deformasjon forekommer jevnlig. En av de mest velkjente strukturene er det 150 km lange Porsgrunn-Kristiansand forkastningskomplekset (PKFK) som grenser Bamble litotektoniske enhet i nordvest. Selv om PKFK er en velkjent struktur, så er lite strukturell data tilgjengelig. Denne masteroppgaven har derfor som mål å karakterisere den strukturelle arkitekturen og evolusjonen til PKFK, gjennom strukturelle analyser og K-Ar geokronologi.

Den utvalgte seksjonen av PKFK har et undulerende og bratt (fall: 62 ± 2°) forkastningsplan som faller mot ØSØ (strøk: 32 ± 2°). Den består av en forkastningskjerne som har gjennomgått betydelig deformasjon og er omgitt av distaldeler. Distaldelen i hengveggen er 370 - 510 meter bred, mens distaldelen i liggveggen er 60 - 280 meter bred. Forkastningskjernen er en 2.5 - 5 meter tykk kompositt-struktur som består av 12 sidestilte strukturelle facies, som er dannet ved ulike aldre. Forkastningskjernen har en sprekketetthet som overskrider 40 sprekker per m^3, hvor dette bidrar til økt permeabilitet i distaldelene og deler av forkastningskjernen. Den økte permeabiliteten forårsaker økt hydrotermal omdanning, hvor klorittifisering av biotitt og utfelling av karbonat-årer opptrer hyppig.

Alders-data fra K-Ar geokronologien viser at den utvalgte seksjonen av PKFK har opplevd betydelig bevegelse gjennom flere bevegelses-faser i den Mesozoiske æraen, fra midten av Trias til tidlig Kritt. Dannelsesrekkefølgen startet med en tidlig bevegelse (227 - 224 Ma), hvor det ble dannet en bredere sone med grovkornet forkastningsbreksje. Senere ble strukturell facies 3 (SF3) dannet (<221 Ma), etterfulgt av SF7 (<193 Ma), SF9 (152 Ma) og SF8 (122 Ma). I tillegg har en tidligere kataklasitt-dannende bevegelse blitt avdekket langs den utvalgte seksjonen av PKFK, som forsiktig har blitt knyttet til post-svekonorvegisk rifting. Kinematiske indikatorer antyder en strike-slip orientert bevegelse under den tidligere kataklasitt-dannende bevegelsen og dip-slip orientert bevegelse under de senere Mesozoiske bevegelsene.

Til slutt har en kombinasjon av lineament analyse og sammenligning av K-Ar aldre med aldre fra kutting av ulike sedimentære og vulkanske lag i Porsgrunn område antydet at PKFK består av to segmenter: ett nordre segment, plassert sør for Porsgrunn og ett søndre segment, plassert nord for Kristiansand. Det nordre segmentet er omtrentlig 24 km langt, mens det søndre segmentet har en lengde på omtrentlig 70 km og begge segmentene er orientert omkring NØ-SV.

Table of Contents

List of Figures

List of Tables

Preface

1 Introduction

This master thesis will combine dating of fault gouge and fault breccia, using K-Ar geochronology, with recording of kinematic indicators and XRD analysis. This is to unravel the structural and temporal evolution of the studied section of the Porsgrunn-Kristiansand Fault Complex (PKFC). The PKFC is a fault complex spanning from Porsgrunn, down to Kristiansand. Previous studies have been conducted on the northern section of the PKFC, with a focus on using the ^{40}Ar/^{39}Ar dating technique on muscovite fish found in mylonites (Mulch et al., 2005; Mulch and Cosca, 2004). However, little research have been done on the southern section of the PKFC. This study therefore aims to provide increased knowledge about this understudied, but very significant fault in the south of Norway.

The chosen study area is located inside the Herefoss granite, as shown in figure 1. The main outcrop that was studied is located at Rislå (6495383 N, 109064 E, UTM zone 33), where a significant amount of the PKFC has been exposed during excavation work (see fig. 2). There has been a special focus on mapping the PKFC fault core at the Rislå outcrop, where different brittle structural facies have been identified. Brittle structural facies refer to juxtaposed domains found within the fault core, characterised by different fault rocks, mineralogical compositions, texture and kinematics (Tartaglia et al., 2020). The brittle structural facies are not necessarily coeval and dating of the various brittle structural facies are pivotal to understanding the structural and temporal evolution of the fault. The mineralogy of samples collected from throughout the fault zone were characterised by optical microscopy in an attempt to study the effects that faulting has on the mineralogy of the Herefoss granite. A combination of scanlines and 3D modelling of the outcrop has also been utilized to map fracture frequencies and orientations within the fault zone. Finally, a step by step model of the evolution of the PKFC, unraveling the timing and slip orientations of previous phases of slip will be presented.
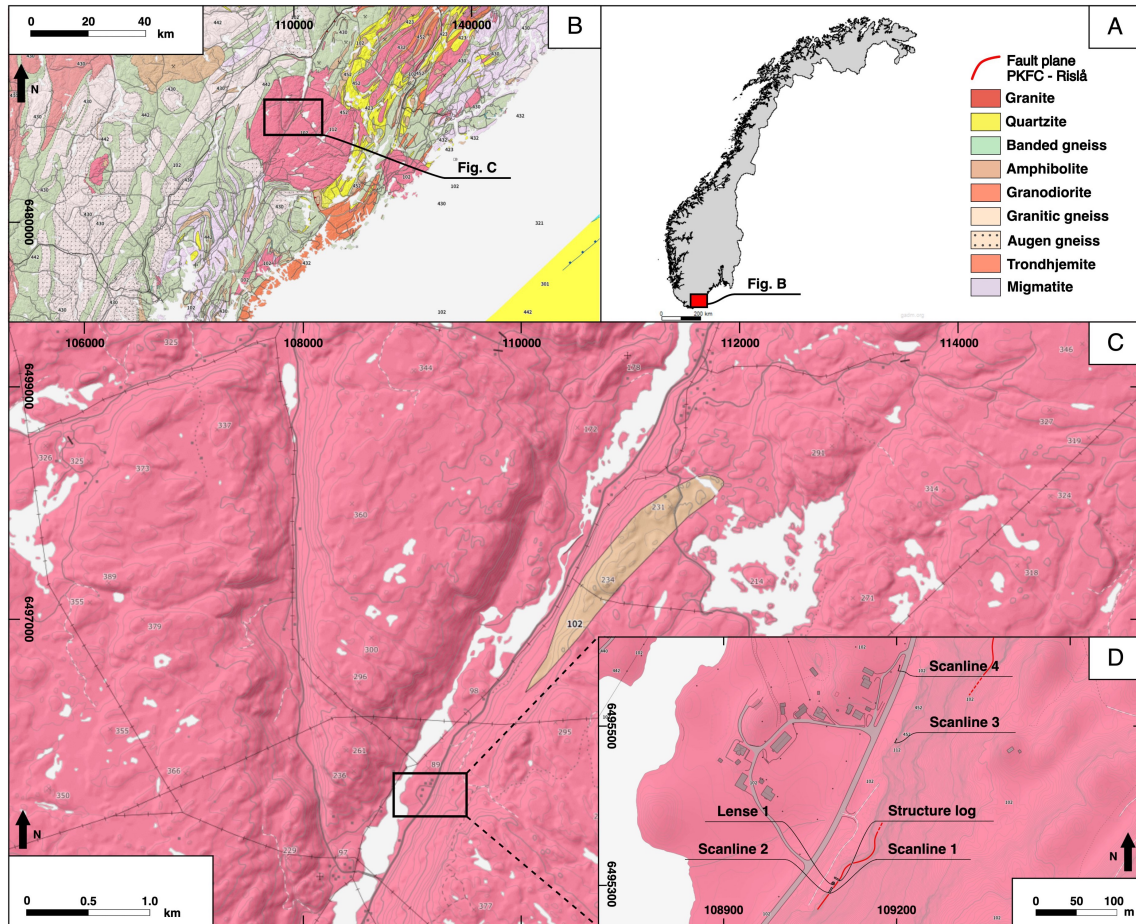
Figure 1: Overview map showing the location of the study area: A) Full map view of Norway, where the location of subfigure B is highlighted with a red square. B) Geological map of Agder, northeast of Kristiansand, with belonging legend shown in subfigure A. The black square indicate the location of subfigure C, inside the Herefoss granite. C) Geological map showing the study area. The Rislå outcrop is marked with a black square and belonging legend is shown in subfigure A. D) Enlarged figure presenting the Rislå outcrop with measured scanlines, fault lense and structure log. The red line indicates the orientation of the PKFC fault plane where measured in the field. For a more detailed map of the Rislå outcrop, see figure 17. Coordinates in UTM zone 33.
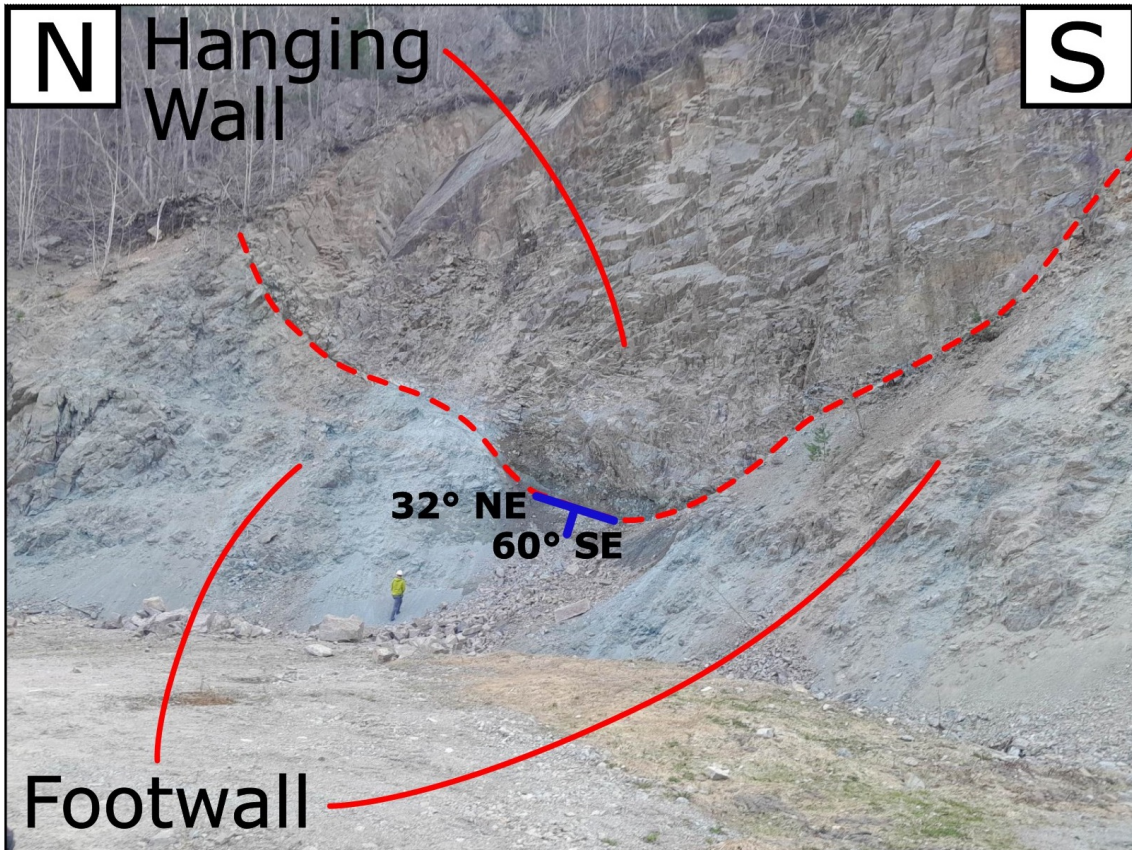
Figure 2: Shows the main outcrop at Rislå, where the fault plane of the PKFC is marked with a red stipled line. The strike and dip of the measured portion of the PKFC has also been annotated. The structure log, scanline 1 and 2 and measured fault lense (see fig. 1 and 17) is located south-southwest of the shown area, right of the picture.

2 Regional geology

2.1 The Herefoss granite

The studied section of the PKFC are located in the center of the Herefoss granite, in the Agder area, northeast of Kristiansand. A large proportion of the mapped locations are located along the Topdalselva topolineament, as shown in fig. 15. The Herefoss granite was formed approximately 900 Ma, as a circular diapiric body, with a diameter of approximately 20 km (Elders, 1963; Nilssen and Smithson, 1965). The Herefoss granite is surrounded by gneisses round the whole of its periphery, with exception of the area north of the granitic body, which contains fine grained granite (Elders, 1963). The Herefoss granite is younger than the surrounding gneisses, which have been folded. In

Figure 3: Example of undeformed granite found inside the Herefoss granite, west of the PKFC.

the general region east of the PKFC, major folds with moderate plunge and steep axial-planes are commonly developed, with a strike parallel to the PKFC. Southwest of the Herefoss granite, a S-shaped fold occurs, covering 40 - 50 square kilometers. The main part of this fold is an open synformal fold, see fig. 4. Minor cross-folds are well developed in the area north of the Herefoss granite, consisting of three generations of folds and lineations. The youngest generation has occurred in connection with faulting which happened after the formation of the Herefoss granite (Elders, 1963), maybe in connection with activation or reactivation of the studied section of the PKCF. There are also some occurences of migmatization of the gneisses (Elders, 1963) and inclusions of gneisses are found both near the border of the Herefoss granite and in the Eastern parts of the granite. These inclusions are less common in the western parts of the granite (Smithson, 1963) and are generally fractured, with no specific orientation. Most of these inclusions belong to the Granulite facies (Elders, 1963). The Herefoss granite is mainly a massive, coarse grained, holocrystaline, porphyric microcline granite with a strong red colour (Elders, 1963; Heldal, 1992). It is characterized by a hypidiomorphic granular texture (Elders, 1963). Microcline constitutes approximately 50 % of the granite and appears as 1 - 5 cm pink crystals with a elongate or tabular, euhedral to subhedral shape (Elders, 1963;

Figure 4: Structural map of the Herefoss granite and the surrounding gneisses. From Elders, 1963.

Heldal, 1992). Some fine to medium grained granite, aplite and dark monzonite appear locally (Heldal, 1992), where the fine grained granite has been formed by cataclasis (Elders, 1963). The main minerals in the matrix are plagioclase, quartz, biotite and chlorite. Locally, the quartz has a dark blue colour, but elsewere the colour is white to grey-blue (Heldal, 1992). The accessory minerals found in the granite are apatite, epidote, alanite, hematite, ilmenite, magnetite, pyrite and titanite (Heldal, 1992).

2.1.1 Mineralogical content and descriptions

Elders, 1963 described the appearance of the different minerals occuring in the Herefoss granite by using microscope and thin sections. These mineralogical descriptions are shown below.

Microcline: Tartan twinning is always present, but can be feebly or patchily developed. Some of the larger grains of microcline are bordered by an irregular rim of plagioclase grains and larger inclusions of plagioclase occur in the microcline, in the form of rounded masses and euhedral crystals. Inclusions of quartz, biotite and less frequently hornblende also occur in the microcline.

Plagioclase: Plagioclase occurs both as inclusions in the microcline and as tabular, subidiomorphic crystals in the ground mass, with sizes of up to 1 cm. Twinning always occurs

14

within the plagioclase, were a combination of albite-, Carlsbad- and pericline twinning is seen. The composition of the plagioclase usually lies between An_{10} and An_{20}, were the inclusions in the microcline have the same composition as the plagioclase in the groundmass. Zoning around inclusions of plagioclase is usually absent or incomplete, were zoning around plagioclase in the groundmass consists of a sharply defined outer rim, 0.1 - 0.2 mm thick. The zonation consists of albite feldspar around a central core of oligoclase.

Quartz: The quartz varies in grain size and can be found as both allotromorphic crystals with sizes up to 3-4 mm and as aggragates of grains about 0.1 mm across. The allotromorphic crystals have an anhedral shape, with a patchy, undulatory extinction. They appear to be formed by recrystallization of more fine grained aggregates, as they contain inclusions of other minerals, as well as smaller quartz grains with a different orientation than the allotromorphic crystals.

Biotite: This mineral occurs as glomerogranular aggregates, normally juxtaposed with sphene, ores and hornblende. Minute inclusions of zirkons with pleochroic halos are normal.

Hornblende: Hornblende appear both as euhedral inclusions in microcline and subhedral crystals in the groundmass. Commonly it appears intergrown with biotite which appears to have replaced it.

Accessory minerals: Most commonly occurs as sphene and ores in the form of euhedral and subhedral crystals of magnetite and skeletal masses of ilmenite.

2.1.2   Varieties within the granite

The Herefoss granite mainly consists of two main parts; the western granite facies (WGF) and the eastern granite facies (EGF), divided by the PKFC. Several other versions of the granite also occur locally, like fine grained red and gray granite and mylonitic granite (Elders, 1963).

The western granite facies: These facies constitute the granite located west of the PKFC and a portion of the granite along the southern boundary, east of the PKFC. Elders, 1963 suggests that the mineralogy of the WGF consists of 45% microcline, 22-23% plagioclase, 20-21% quartz and approximatly 10% ferromagnesian minerals. Biotite is the main constituent of the ferromagnesian minerals, while sphene, ores and hornblende constitute 1-2 % of the rock. The microcline crystals in the WGF are larger than the crystals found in the EGF, often being more than 3 cm long (Elders, 1963).

The eastern granite facies: The EGF are generally more variable than the WGF, with a

more massive appearance and a redder colour. Elders, 1963 suggests that the mineralogy of the EGF consists of 53-55% microcline, 20% plagioclase, 20% quartz and 5% ferro-magnesian minerals, mainly consisting of biotite. Unlike in the WGF, hornblende has not been seen in the EGF (Elders, 1963).

2.1.3 Formation temperature of the Herefoss granite

T. Barth, n.d. suggested a formation temperature of 550° C for the Herefoss granite, while Nilssen, 1961 suggested a formation temperature ranging between 450° C - 600° C. Here, the formation temperatures near the outer bounds of the granite lie within the higher end of the temperature range (Nilssen, 1961). For comparison, T. Barth, n.d. suggested that the gneisses surrounding the Herefoss granite had a formation temperature of 400° C. Nilssen, 1961 concludes that the formation temperature for the feldspars were approximately 500° C, as the microcline is perthitic and usually triclinic. Some transitioning between triclinic and monoclinic has also been seen in the microcline.

2.1.4 The internal structure of the Herefoss granite

T. F. Barth, 1947 suggested that the Herefoss granite is massive, with no indication of flow or foliation. However, later studies preformed by Elders, 1963 have shown that especially the western facies of the granite have a well defined platy parallelism, which occurs in four ways: tabular microcline crystals with parallel homogeneous orientation, parallel clusters of biotite, enclaves arranged in parallel planes and thin layers of granite with a lack of mica (Elders, 1963). The first of these factors is by far the most common too occur in the western facies of the granite. Planar structures also occur in the eastern facies of the granite, but are never strongly developed. There are also no occurrences of parallel tabular microcline crystals in the eastern facies of the granite. In addition, elongation of feldspar and quartz crystals frequently occur, both in the western and eastern facies of the granite.

2.1.5 3D Modelling of the Herefoss granite

Smithson, 1963 produced a 3D gravity model of the Herefoss granite, using Bouguer gravity anomaly maps. The gravity model is composed of a large disc underlain by a smaller disc that is offset to the east (see fig. 5). This gravity model suggests that the Herefoss granite has the shape of a funnel, with a thickness of 2 km at the east and 0.4 km at the west.
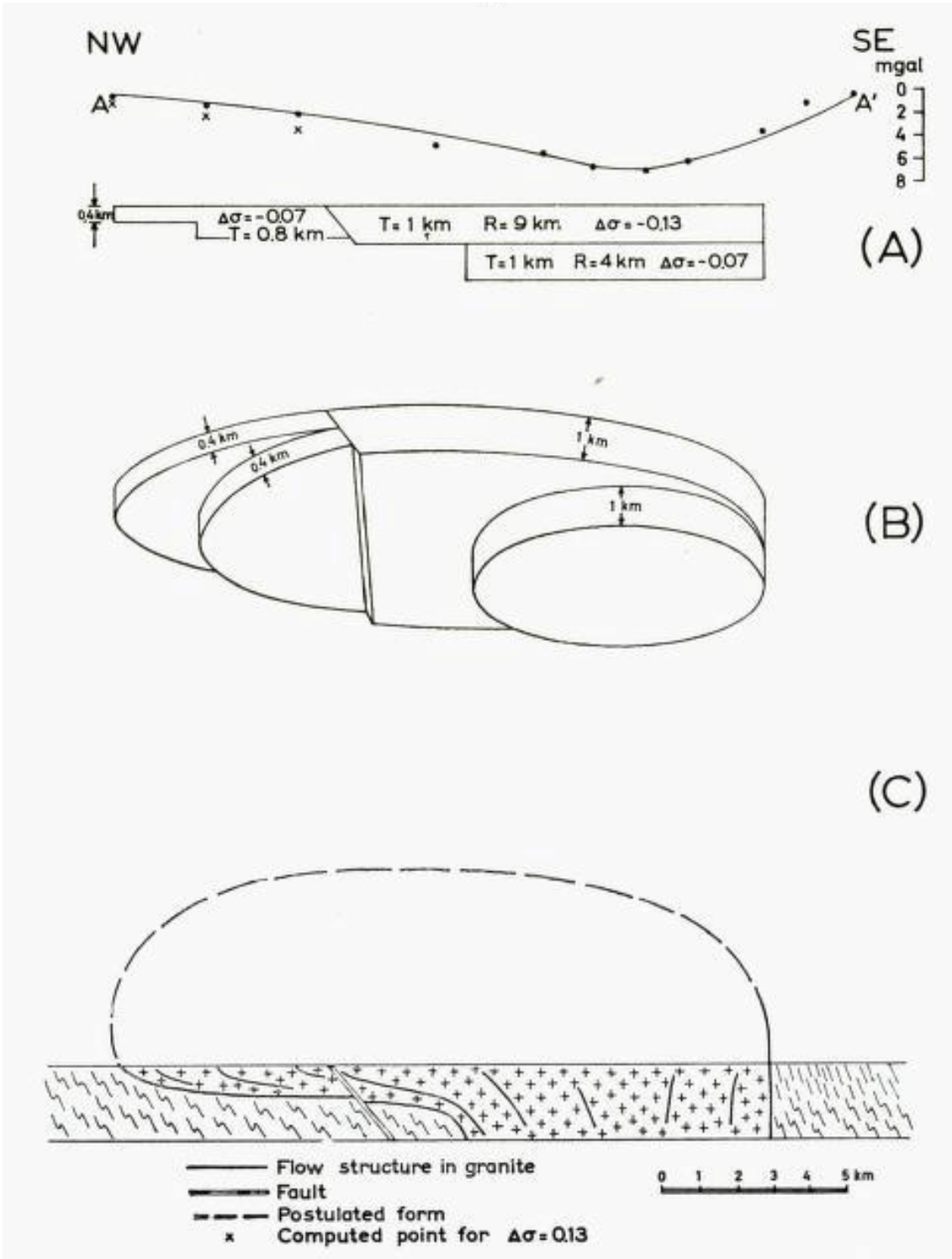
Figure 5: Gravitational 3D model of the Herefoss granite. From Smithson, 1963.

2.1.6 The Herefoss granite and the PKFC

Bugge, 1928 suggested that the Herefoss granite has been only slightly fractured by the southern section of the PKFC and that the main period of faulting is older than the granite. Bugge, 1928 therefore stated that the Herefoss granite has been affected by a relatively small amount of movement and displacement. However, Elders, 1963 stated that there has been a significant amount of displacement in the Herefoss granite and argue that a similar amount of deformation can be found along the PKFC, both within and outside the granite. Elders, 1963 has observed that there are different deformational products inside and outside the granite, but that this is caused by differences in physical properties for the different deformed rocks. The gneisses tend to yield by movement on pre-existing foliation planes and the granite by brecciation and cataclasis (Elders, 1963).

2.2 Regional geology of Porsgrunn and Skien

The Skien-Porsgrunn region consists of a long and narrow (50 km x 2.5 km) belt of Cambro-Silurian sedimentary rocks, juxtaposed to the west by Precambrian bed rock and to the east by Permian–Carboniferous volcanic rocks and plutons (see fig. 6). Proximity to the Permian plutons has caused contact metamorphism within the Cambro-Silurian sedimentary rocks (Rønning et al., 2020). The base of the Cambro-Silurian sedimentary rocks in the Skien–Langesund District is marked by the Stokkevannet formation, formed during early Cambrian age (Nielsen 2011), while Upper Silurian sandstones form the top (Rønning 2020). The Permian–Carboniferous volcanic rocks and plutons to the east mostly consist of basalt, syenite and larvikite (see 6).

Previous work has proposed that the Kristiansand-Porsgrunn Shear Zone (KPSZ) was first activated as a Mesoproterozoic thrust shear zone, associated with Sveconorwegian ($\sim$ 1.1–1.2 Ga) northwestward thrusting of the Bamble block over the Telemark block. It was later reactivated as a Neoproterozoic extensional shear zone, associated with post-Sveconorwegian rifting and orogenic collapse (Mulch et al., 2005). The brittle Porsgrunn-Kristiansand Fault (PKF), which cuts through the Cambro-Silurian sedimentary rocks, has later overprinted the KPSZ related mylonites with a top-to-the-SE movement. The PKF does not cut through the Permian–Carboniferous volcanic rocks and plutons east of the Cambro-Silurian sedimentary rocks (see fig. 6).
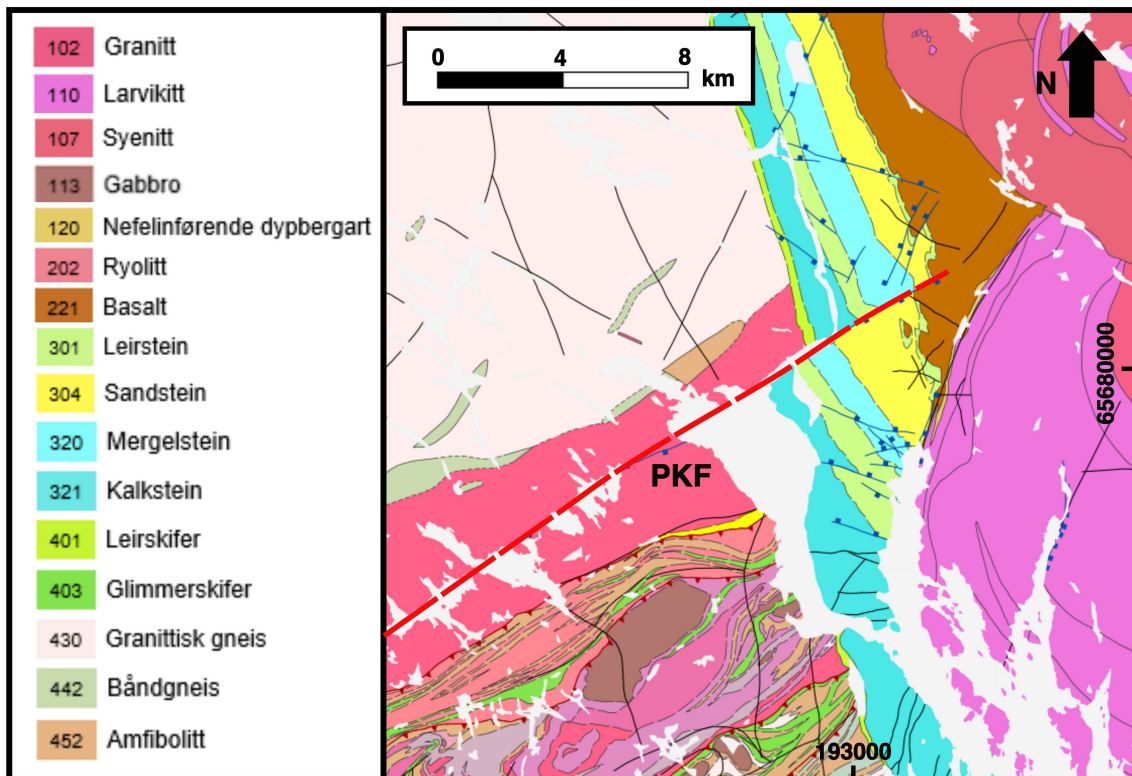
Figure 6: Map of the regional geology of the Skien and Porsgrunn area, with legend shown to the left. The PKF is annotated with a red stippled line. The map sheet is downloaded from NGU.no and the coordinates are in UTM zone 33.

3 Theory

3.1 Lineaments

Lineament is a term for a linear or curvilinear feature, which is identified by remote sensing methods. Lineaments can be found in several types of data, including topographical data, photometric data (e.g. multispectral satellite imagery) and magnetic data. A lineament can either have negative values (valleys) with higher values at the margins, positive values (ridge) with lower values at the margins or be an edge, were the values change gradually perpendicular across the lineament (Torgersen et al., 2021). Several processes can be responsible to form lineaments, both geological, biological and man-made. Topolineaments (lineaments found in topographical data), which are the most frequently mapped, can either be formed as a result of bedrock related factors or area-specific erosion. Examples of bedrock related factors are faults, joint-swarms, fracture corridors, rock contacts, dikes and traces of foliation (Clark and Wilson, 1994; R. H. Gabrielsen and Braathen, 2014; Torgersen et al., 2021), while area specific erosion can be a result of either rivers or glaciers, see fig. 7 (Torgersen et al., 2021).

It is hard to recognize which process or processes that are responsible for creating a lineament, but there are some general trends. Topolineaments associated with foliation are generally wide and shallow, with a mostly parallel orientation (Torgersen et al., 2021). On the other hand, topolineaments associated with faults and dikes are narrow and deep and the orientation can vary. Topolineaments associated with faults also often occur far away from each other (Torgersen et al., 2021). Relatively large, U-shaped topolineaments indicate that it has been formed by a glacier, while V-shaped topolineaments normally are formed by rivers.

When mapping lineaments manually, there are mainly three factors affecting the results. When using a shadow relief, the azimuth of the light source will enhance the lineaments that are perpendicular to the light source, while simultaneously disguising the lineaments that are parallel (Gunleiksrud, 2017). The scale of the map being used will also affect the results, where smaller scale maps enhances smaller sized lineaments and larger scale maps enhances larger sized lineaments (Gunleiksrud, 2017). Also, the skill and background of the operator can affect the results (Torgersen et al., 2021).

The main orientations of mapped lineaments are often presented in a rose-diagram. It is also normal to use a histogram to present the distribution of lineament-lengths within the mapped lineament-population.
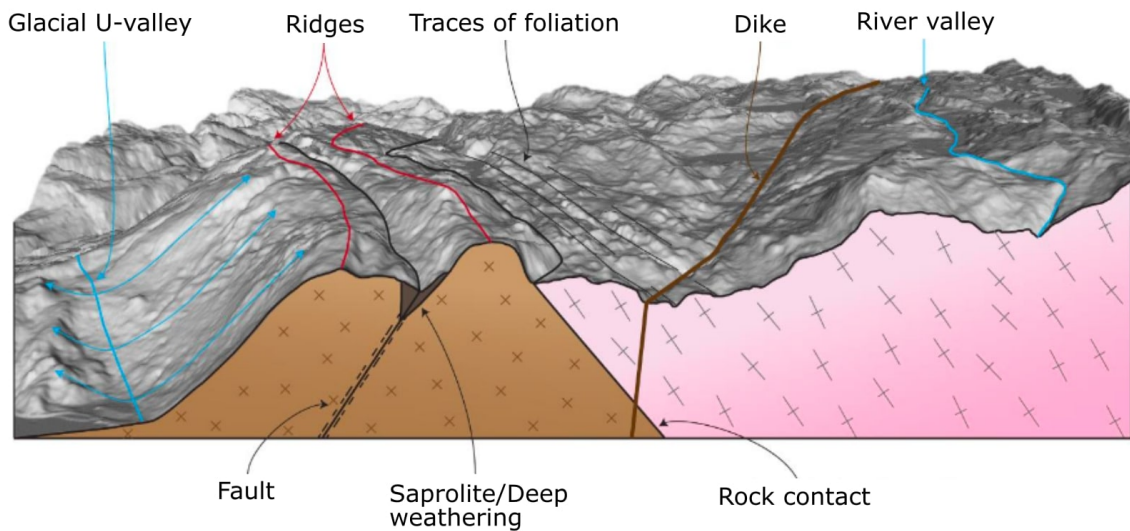
Figure 7: The different lineament forming mechanisms and their associated lineaments. Modified from Torgersen et al., 2021.

3.2   Fracture lineaments and fault architecture

Fracture lineaments consist of zones with markedly enhanced fracture frequency, where the linear depression in the topography most likely is a result of a stress-induced weakness in the bedrock (R. H. Gabrielsen and Braathen, 2014). R. H. Gabrielsen and Braathen, 2014 suggests that fracture lineaments can be subdivided into three types: joint swarms, fracture corridors and faults. Joint swarms and fracture corridors appear often as sub-vertical, long, narrow and tabular zones of fracturing (Ozkaya and Richard, 2006). They have a symmetric fracture distribution, with the highest fracture frequency located in the middle of the fracture lineament and decreasing fracture frequency towards the outer bounds (Braathen and Gabrielsen, 1998). Fracture corridors represent an incipient stage of faulting, where continued increase of stress can lead to accumulation of displacement, resulting in a brittle fault (R. H. Gabrielsen and Braathen, 2014). R. H. Gabrielsen and Braathen, 2014 has defined a documentable 1 m of displacement as the lower limit to classify a fracture lineament as a fault. Inclined faults tend to have an asymmetric distribution of fracture frequency and deformation, with a higher amount of strain located in the hanging wall compared to the footwall (Braathen and Gabrielsen, 1998; R. H. Gabrielsen and Braathen, 2014). Subvertical/steep faults have a symmetric distribution of fracture frequency and deformation (Braathen and Gabrielsen, 1998).

Fracture lineaments can be subdivided into three distinct zones; central parts, marginal and distal parts and outboard parts of general background fracturing (Braathen and Gabrielsen, 1998). When describing fault architecture, these zones are called fault core, damage zones and outer zones, respectively. The outer zone consists of a protolithic rock that

has not yet been deformed and only has experienced some background fracturing, with a fracture frequency normally between 0 - 3 fractures/meter (R. H. Gabrielsen and Braathen, 2014). The damage zones are marked by fracture systems with an elevated fracture frequency (5 - 10 f/m) compared to the background fractures found in the outer zones. The fault core is commonly identified by the appearance of fault rocks and has an even higher fracture frequency (> 10 f/m) (R. H. Gabrielsen and Braathen, 2014). The largest portion of displacement is recorded in the fault core with smaller amounts of displacement recorded in the damage zones. A fault core does not occur within all faults, but is common in faults that have experienced significant displacement and deformation. There is a positive correlation between the amount of displacement recorded in the fault and the thickness of the fault (Z. Shipton and Cowie, 2001; Z. K. Shipton et al., 2006). There is also a positive correlation between the amount of displacement and the rupture length of different faults (Cowie and Scholz, 1992; C. Scholz et al., 1993).

Braathen and Gabrielsen, 1998 and R. H. Gabrielsen and Braathen, 2014 have separated fracture lineaments, including faults, into five zones ranging from A - E. Zone A - B constitutes the center of the fracture lineament and commonly has a width of 5 - 20 meters (max. 30 - 50 m) (Braathen and Gabrielsen, 1998). Zone A and B are typically oriented parallel or subparallel to the trend of the fracture lineament.

Zone A consist of brittly deformed fault breccia and fault gouge, but can also contain mylonite if ductile deformation has occurred (R. H. Gabrielsen and Braathen, 2014). This zone has a complicated structure and consists of a network of fault lenses and shear fractures with different orientations, sizes and morphology. Secondary mineralisation occurs frequently. Zone A requires a significant amount of displacement and shear deformation to form and therefore only occurs within larger faults. Zone A is synonymous with the fault core and it typically has a width from some centimeters to several tens of meters (R. H. Gabrielsen and Braathen, 2014).

Zone B is associated with a high fracture density typically between 10 - 20 fractures/meter, but can increase to 100 fractures/meter or more, depending on the lithology (R. H. Gabrielsen and Braathen, 2014). The fractures are normally oriented either subparallel or with a small angle (10 - 20°) to the fault plane. The majority of the fractures in zone B are shear fractures (mode II), but some tensile fractures can also occur (mode I). Striatons can often be seen on shear fractures, in addition to riedel shears (R. H. Gabrielsen and Braathen, 2014). Mineralisation is often found on the surface of tensile fractures. In zone B, the host rock has been strongly deformed and normally consists of either protocataclasite or protobreccia. The thickness can vary, but is rarely thicker than a few meters (R. H. Gabrielsen and Braathen, 2014).
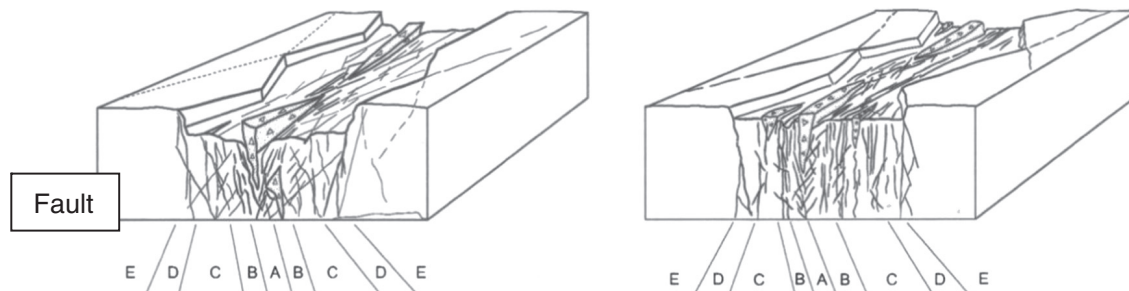
Figure 8: Conceptual sketch of the different zones of a fracture lineament. From R. H. Gabrielsen and Braathen, 2014.

Zone C often has a significantly lower fracture frequency compared to zone B, varying between 2 - 5 fractures/meter (R. H. Gabrielsen and Braathen, 2014). Both shear fractures (mode II) and tensile fractures (mode I) are prominent (Braathen and Gabrielsen, 1998; R. H. Gabrielsen and Braathen, 2014). This indicates that a lower amount of strain and displacement has occurred compared to zone A and B, where shear fractures are dominating. The fractures are mostly oriented subparallel to the fault core/trend of the fracture lineament (Braathen and Gabrielsen, 1998; R. H. Gabrielsen and Braathen, 2014). Mineralization on the surface of the fractures is far less frequent compared to zone A and B, indicating a lower flow of fluids. The border between zone B and C is often abrupt and zone C normally has a thickness between 5 - 50 meters (Braathen and Gabrielsen, 1998; R. H. Gabrielsen and Braathen, 2014).

Zone D has a fracture frequency between 0.5 - 4 fractures/meter and the fracture orientations are less homogeneous compared to zone C (Braathen and Gabrielsen, 1998; R. H. Gabrielsen and Braathen, 2014). Typically two sets of fractures are found in zone D, one subparallel to the fault core/trend of the fracture lineament and one with an angle of 30° - 60° from the fault core (Braathen and Gabrielsen, 1998; R. H. Gabrielsen and Braathen, 2014). Zone C typically defines the topographical border of the lineament and is normally 5 - 10 meters wide (Braathen and Gabrielsen, 1998; R. H. Gabrielsen and Braathen, 2014).

Zone E represents the transition between the fracture lineament, with a higher density of fractures, and the undeformed protolithic rock outside the fracture lineament. It is typically found 50 - 250 meters outside the center of the fracture lineament and is typically 25 - 250 meters thick. Zone E has a fracture density of 1 - 3 fractures/meter and the fractures are dominated by tensile fracturing (mode I) (R. H. Gabrielsen and Braathen, 2014). The orientation of fractures in zone E is inhomogeneous, but typically has an angle 0° - 40° from the fault core/trend of the fracture lineament. Typically no mineralisation is seen on fracture surfaces in zone E.

3.3 Fault rocks

The fault core consist of fault rocks, which have experienced significant strain and deformation. Frictional properties, temperature, effective stress normal to the fault and differential stress are typical factors that decide which fault rocks that are formed (Sibson, 1977). Typical fault rocks are mylonite, cataclasite, fault breccia, fault gouge, crush breccia and pseudotachylyte.

Mylonites are formed in faults deeper than 10 - 15 km, which are called shear zones, where high pressure and temperature produce ductile deformation of the host rock. They are characterised by foliated fabric and can be subdivided into proto- and ultramylonite, depending on the clast/matrix ratio. Protomylonites have a higher portion of clasts, while ultramylonites have a higher portion of matrix.

Fault breccia and *fault gouge* has been formed in faults shallower than 10 - 15 km and is a result of brittle deformation. Sibson, 1977 proposed a classification were fault gouge is defined as an incohesive fault rock with randomly oriented fabric and less than 30% visible fragments comprising the rock. Fault breccia is defined as an incohesive fault rock with more than 30% visible fragments.

Brittle				←*Deformation style*→				**Ductile**		
Frictional flow					←*Dominant deformation mechanism*→		**Plastic flow**			*% matrix and grain-size*
Non-cohesive			Secondary cohesion			Primary cohesion				
			Cemented HB	Indurated HB			*> 50% phyllosilicate*	*< 50% phyllosilicate*		*0-50% matrix*
Hydraulic breccia (HB)	Breccia series	Proto-breccia	Cemented proto-breccia	Indurated proto-breccia	Cataclasite series	Proto-cataclasite	Proto-phyllonite	Proto-mylonite	Blastomylonite	*0-50% matrix*
		Breccia	Cemented breccia	Indurated breccia		Cataclasite	Phyllonite	Mylonite		*50-90% matrix*
		Ultra-breccia	Cemented ultra-breccia	Indurated ultra-breccia		Ultra-cataclasite	Ultra-phyllonite	Ultra-mylonite		*90-100% matrix*
		Gouge	Cemented gouge	Indurated gouge						*Sub-microscopic matrix*
			Pseudotachylyte							

Figure 9: Classification of fault rocks based on deformation style, amount of matrix and cohesion. From Braathen et al., 2004.

Cataclasite is a fault rock that has maintained its primary cohesion during deformation and is formed by a combination of brittle and ductile deformational mechanisms. It consists of clasts surrounded by matrix and is subdivided into proto- and ultracataclasite, similar to mylonites.

Crush breccia is cataclasite with less than 10% matrix and is subdivided into crush breccia, fine crush breccia and crush microbreccia, depending on the grain size. Crush breccia contain clasts > 0.5 cm, fine crush breccia between 0.1 - 0.5 cm and crush microbreccia < 0.1 cm.

Pseudotachylytes consists of glass/devitrified glass and are formed by brittle shearing of intact rock or sliding on existing planes (Sibson, 1977).

3.4 Fault types

R. H. Gabrielsen and Braathen, 2014 has suggested that faults can be subdivided into four types, based on the type of fault rocks and the geometry and distribution of fault rocks found within the fault core. These fault types are listed in table 1, shown below.

Fault type	Description
Type I	Entirely dominated by different types of mylonites.
Type II	Contains brittle deformational products, which are overprinting mylonites.
Type III	Characterized by entirely brittle fault rocks, which contain cemented, non-cemented or partly cemented deformational products.
Type IV	Characterized by the absence of fault rocks.

Table 1: Description of the four fault types suggested by R. H. Gabrielsen and Braathen, 2014, based on fault rock type and geometry and distribution of fault rocks within the fault core.

3.5 Formation and growth of faults

R. H. Gabrielsen and Braathen, 2014 has suggested that development of faults starts with the formation of a joint swarm. With increasing stress over time, this joint swarm will transform into a fracture corridor, characterized by a wider and more intense zone of fracturing. Small pockets of fault rocks can be found in the center of fracture corridors, which are not found in joint swarms (R. H. Gabrielsen and Braathen, 2014). Some strain is recorded in the fracture corridors, but the shear fractures still have a displacement of less than 1 meter. When sufficient strain is accumulated in the central part of the fracture corridor, brecciation and generation of fault rocks commence. This forms a major through-going tabular structure in the middle of the fracture lineament, creating a fault plane. This is where the majority of strain is accumulated. A sketch presenting the evolution from a joint swarm to a fault is shown in figure 10.

Fault growth often begins with the formation of several smaller faults. When these are subjected to increasing stress, the amount of strain will increase, resulting in a repetitive cycle of tip-line propagation (Mansfield and Cartwright, 2001). They will therefore eventually overlap and grow into larger faults with more length and displacement. Therefore, the amount of displacement along a larger fault often has a saw-tooth pattern. The general trend is still that the maximum displacement is recorded in the mid-section along the fault, while the minimum displacement is recorded near the tips (C. Scholz et al., 1993).

Walsh et al., 2002 has suggested an alternative to the propagating fault model, called the constant length fault model. This model proposes that fault lengths are near-constant from an early stage and growth is achieved mainly by increase in cumulative displacement. The propagating fault model however. is characterized by simultaneous displacement accrual and lengthening of the fault by rapid tip propagation, relay breaching and segment linkage (Rotevatn et al., 2019). Rotevatn et al., 2019 has suggested that the propagating fault model describes the early stages of a faults lifespan (first 20 - 30%), while the constant length fault model describes the later stages (later 70 - 80%). The fault length is therefore established during the early stages of the faulting process, while the majority of the displacement accrual occurs during later stages.
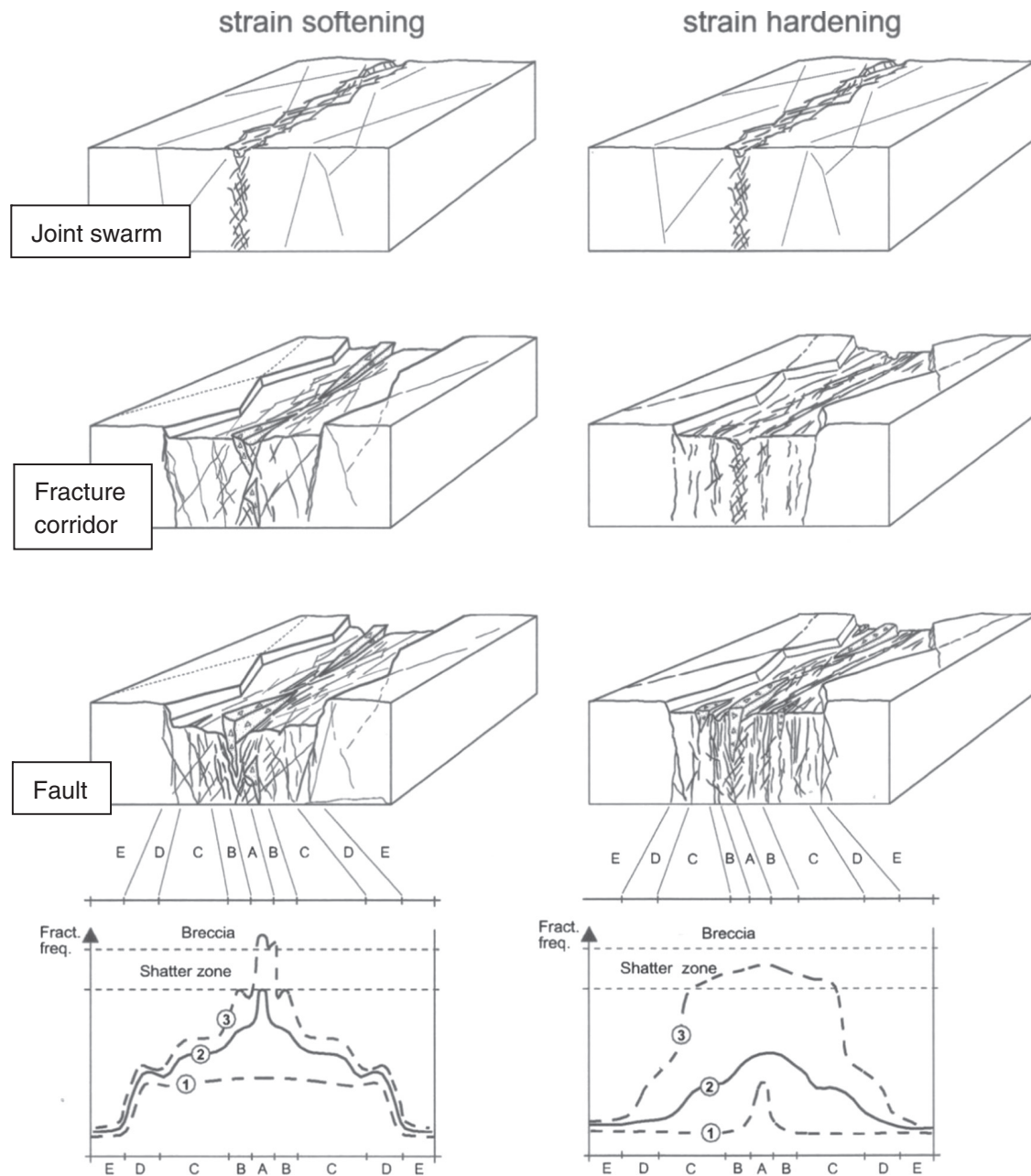
Figure 10: Conceptual sketch of the development of a fault, were a joint swarm is transformed into a fracture corridor and eventually into a fault. The right side shows strain softening and the left side shows strain hardening. The curves (lower part of the figure) shows the fracture frequency along the fracture lineament at different stages. From R. H. Gabrielsen and Braathen, 2014.

3.6 Permeability along faults

Faults have a significant effect on the permeability and hydraulic conductivity of the bed rock (Caine et al., 1996; Evans et al., 1997). Parameters that affect a fault zones permeability, porosity and storativity include lithology, fault displacement, three-dimensional fault zone geometry, deformation conditions, types of subsidiary structures, fluid-rock interactions and the spatial and temporal variability of these parameters (Caine et al., 1996). Faults can act as either a conduit, a barrier or a combined conduit/barrier (Caine et al., 1996), which is dependent on the thickness of the damage zone compared to the thickness of the fault core. Caine et al., 1996 has characterized faults into four categories; localized barriers, localized conduits, distributed conduits and combined conduit-barriers (see fig. 12). A localized barrier consists of a fault core with no damage zones and is typically found as deformation bands in sand stones. A localized conduit has neither a fault core nor a damage zone. They consist of a single shear-fracture and are typically found as small faults. A distributed conduit consists of a network of shear and tensile fractures and are typical in the early stages of faulting. A combined conduit-barrier consists of a fault core wrapped by damage zones, which is often found in larger faults. The fault core is fine grained and has little to no permeability, while the damage zones have a high fracture frequency and significant fractures lengths, which result in high permeability (see fig. 11). Larger faults therefore have anisotropic properties, where the permeability and hydraulic conductivity is high along the fault core, but very low/non existent perpendicular to the fault core (Braathen and Gabrielsen, 2000; Evans et al., 1997). The permeability of the fault is also affected by the orientations of the fractures, as the fractures close to the fault core often have a fault parallel orientation (Braathen and Gabrielsen, 1998; R. H. Gabrielsen and Braathen, 2014).

Permeability in both deformed and undeformed crystalline rocks will decrease with increasing confining pressure, which is found at greater depths in the continental crust (Evans et al., 1997). Evans et al., 1997 has researched the change in permeability with changes in depth for the protolith, the damage zones and the fault core of a fault. It was found that the protholith has a more significant loss of permeability at increasing depths compared to the damage zones and the fault core. This is because the protolith has shorter and more poorly connected fractures that are more easily pressed together. At greater depths, the damage zones therefore work as channels with high permeability between the fault core and the protolith, which has a much lower permeability.
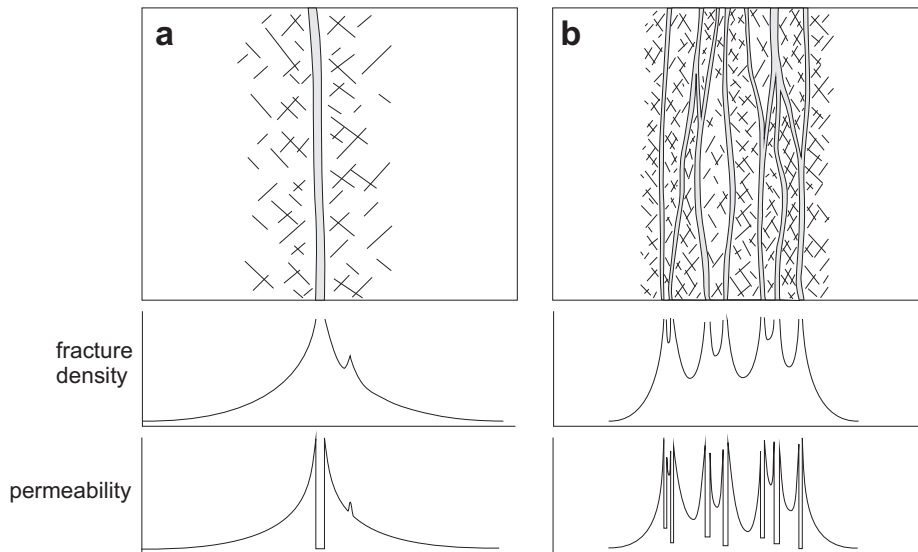
Figure 11: Conceptual sketch showing fracture density and permeability along a perpendicular cross section through a fault. Left side shows an example of a single fault core fault, while the right side shows an example of a multiple fault core fault. From Faulkner et al., 2010.
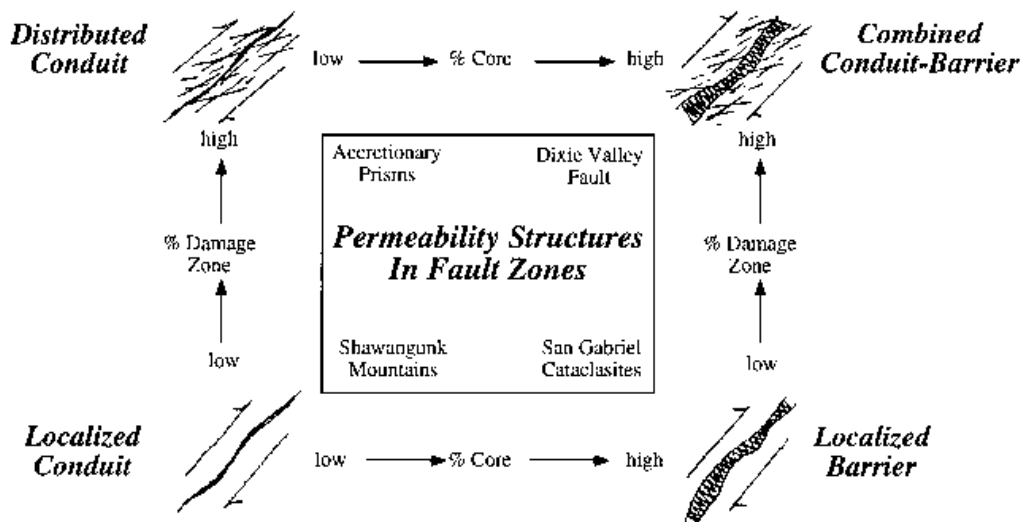
Figure 12: Examples of a localized barrier, a localized conduit, a distributed conduit and a combined conduit-barrier. From Caine et al., 1996.

3.7 Hydrothermal alteration and formation of red feldspar

Brittle deformation and hydrothermal alteration is often closely linked and hydrothermal fluids are normal within larger faults. Because of brittle deformation, fracture frequency is increasing in proximity of the fault, producing higher permeability and easing the flow of hydrothermal fluids. The rheology of the upper 10 km of the crust is greatly influenced by cataclastic processes in feldspar, as feldspar grains are weaker than quartz grains at temperatures below 325°C and at depths of less than 8-10 km (Evans, 1988). Feldspar grains sustain most of the deformation by grain-scale faulting, slip along cleavage-controlled fractures and cataclasis (Evans, 1988). These micro-fractures promote hydrothermal alteration of feldspar to kaolinite (Evans, 1988), where the potassium, sodium, or calcium ions in the feldspar are leached. Syntectonic alteration of the feldspar grains may weaken the fault zones over time and produce foliated textures within the fault zones (Evans, 1988). Quartz is also deformed by micro-fracturing, but to a lesser extent than feldspars. Quartz grains are often healed to form quartz porphyroclasts and mosaics. The quartz sits within a matrix consisting of phyllosilicates, were the size and amount of microcline and plagioclase is decreasing with increased deformation (Evans, 1988).

There is often a direct relation between red feldspars in granitic rocks and hydrothermal activity (Boone, 1969; Plümper and Putnis, 2009) and this reddening phenomenon is often seen in vicinity of fractures. Reddening of feldspar is a result of K-feldspathization of sericite, which is restricted to the altered oligoclase. Submicron sized hematite is then precipitated within the orthoclase pores at the replacement front, which results in the red coloration (Plümper and Putnis, 2009).

Figure 13: Example of reddening of K-feldspar in vicinity of a fracture. From Plümper and Putnis, 2009.

3.8 Sericitic alteration of feldspars

Sericitic alteration occurs in feldspars which have been subjected to hydrothermal alteration (Nesse, 2012), being most common among plagioclase. Sericitic alteration can also occur in orthoclase and microcline. Sericite is made up of very fine graines, typically consisting of muscovite, illite and paragonite, resulting in a brown cloudy appearence on top of the feldspars. Sericitic alteration is typical in vicinity of faults, as the permeability increases within the damage zones and part of the fault core.

3.9 Chloritization of biotite

Chloritization is defined as the formation of clorite as a result of hydrothermal processes or meta-somatic processes. Chloritization of biotite can occur within fault zones and under low-grade metamorphic conditions the reaction can be written as (Parneix et al., 1985):

$$biotite + quartz + H_2O \rightarrow chlorite + orthoclase \tag{1}$$
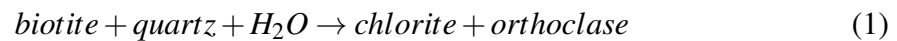
However, in the case of more open geochemical systems, such as hydrothermally altered granites, this reaction becomes more complex, where altered biotite is associated with several alteration products (Parneix et al., 1985). Such products can be green biotite, chlorite, muscovite, sericite, hydromica, kaolinite and other clay minerals, calcite, epidote-zoisite, leucoxene, rutile, pyrite and other sulfides (Schwartz, 1958). The reaction is not a isochemical process, as the fluids introduce new elements and other elements are leached (Parneix et al., 1985).

3.10 Fault lenses

Fault cores of extensional faults at a medium to mature stage of development are dominated by lozenge shaped fault lenses, called horses (R. H. Gabrielsen et al., 2017). These fault lenses have varying lithology and often consist of mildly to strongly deformed country-rock, originating from the hanging wall or footwall. They can also consist of various types of fault rocks, e.g. catalasite, fault breccia, fault gouge and clay smear (R. H. Gabrielsen et al., 2017). These structures are commonly separated by high-strain zones of sheared cataclasite and/or clay smear/clay gouge. They are often stacked on top of each other, forming duplexes. Fault lenses vary considerably in size and often have a width to length ratio between 1/4 and 1/15. Fault lenses formed in sedimentary rocks like limestone, shale and poorly consolidated sandstones are generally thinner, with a lower width/length ratio compared to fault lenses formed in gneisses. There is normally a positive correlation between the length and the thickness of fault lenses and higher displacement faults often produce larger horses (Lindanger et al., 2007). Fault lenses in the cores of extensional faults represent a major uncertainty in fault seal predictions, since they may influence flow paths perpendicular across the fault (Lindanger et al., 2007).

There are several factors which can affect the size and geometry of fault lenses, for example lithology. The width/length ratio is also different between primary (first order) fault lenses and secondary (second order or higher) fault lenses (Lindanger et al., 2007). The geometry of secondary fault lenses is often more varied and is characterized by higher width/length ratios. Secondary fault lenses are formed when primary fault lenses, formed from deformation of the host rock, are sheared and split into several smaller horses.

There are several fault lense forming mechanisms. Examples of these mechanisms are tip-line coalescence, segment linkage, tip-line bifurcation, asperity bifurcation, segment splaying and segment amalgamation (R. H. Gabrielsen and Clausen, 2001). Development of fault horses can be divided into five stages, where several of the previous mechanisms occur (R. H. Gabrielsen and Clausen, 2001):

- The *first stage* produce a through-going fault plane which can be characterized by formation of irregularities and small fault lenses due to tip-line coalescence, segment linkage and in some cases tip-line bifurcation. These irregularities and small fault lenses are gradually destroyed with further extension.

- During the *second stage*, larger irregularities are smoothed by asperity bifurcation, including fault related cut off. Fault lenses formed during stage two are normally formed separately and horse duplexes are rarely formed.

- During the *third stage*, a new generation of fault lenses is formed, either as a result
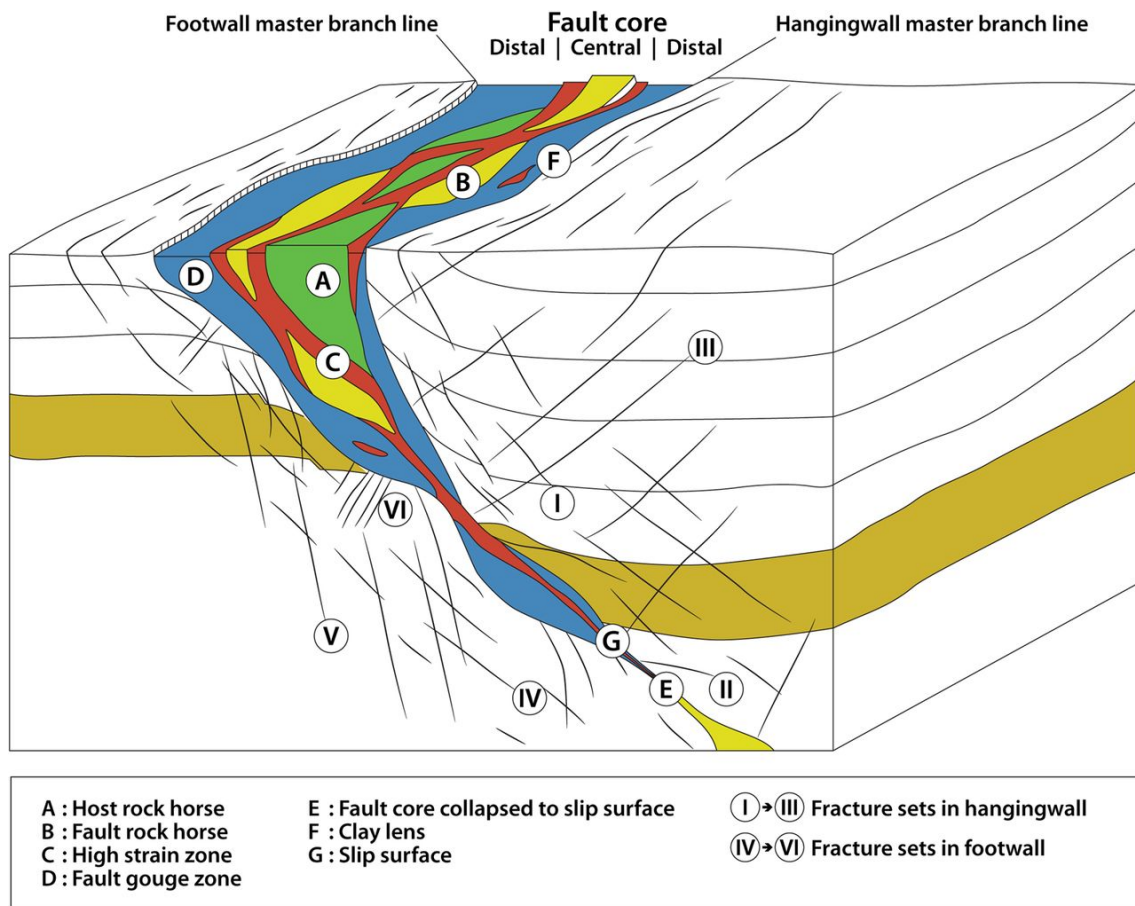
Figure 14: Conceptual sketch of a fault containing fault lenses. From R. H. Gabrielsen et al., 2017

of second or third generation asperity bifurcation or by splaying or coalescence of secondary faults. Fault lense duplexes are more normal during stage three.

- During the *fourth stage*, shearing of individual fault lenses becomes more normal and higher order fault lenses are formed.

- During the *fifth stage*, continued increase in displacement and deformation results in a completely collapsed fault core, where the fault lenses are smeared out, forming a homogeneous mass along the fault plane.

3.11 K-Ar geochronology

K-Ar geochronology is one of the most popular isotopic dating methods (Kelley, 2002b) and is often used to date fault gouge and fine grained fault breccia, unraveling the ages of the different fault slip-periods. It is based on decay of radiometric ^{40}K into ^{40}Ar, were radiometric ^{40}K have a half life of 1250 Ma. 10.48% of the ^{40}K decays to ^{40}Ar by $\beta+$ decay and 89.52% of ^{40}K decays to ^{40}Ca by $\beta-$ decay (Kelley, 2002b). ^{40}K-^{40}Ca dating is not frequently used, as ^{40}Ca is one of the most abundant elements in the crust, making it difficult to measure the amount of radiogenically produced ^{40}Ca in the sample. ^{40}Ar is however a rare trace element and the amount of radiogenically produced ^{40}Ar normally exceeds the amount of trapped ^{40}Ar. A small amount of atmospheric argon can sometimes still be found in the samples and this can be corrected for by using the known atmospheric ^{40}Ar/^{39}Ar ratio of 295.5.

The age of the dated material can be calculated by using the age equation for the K-Ar isotope system, which is shown below (Kelley, 2002b):

$$t = \frac{1}{\lambda} ln \left[1 + \frac{\lambda}{\lambda_e + \lambda_e'} \frac{^{40}Ar^*}{^{40}K} \right] \qquad (2)$$

where t is the time since closure, λ is the total decay of ^{40}K and ($\lambda_e + \lambda_e'$) is the partial decay constant for ^{40}Ar. ^{40}Ar*/^{40}K is the ratio of radiogenic daughter product to the parent ^{40}K.

3.11.1 Spiked and unspiked dating methods

There are two main methods for dating K-bearing clay minerals (Kelley, 2002b): classical spiked K–Ar clay dating and unspiked K–Ar clay dating. When using the spiked analytical method, two aliquots of the same sample are produced; one where the amount of ^{40}K is measured and another one where the amount of ^{40}Ar is measured. Clays are hygroscopic and the samples must be dried. The samples are therefore wrapped in foil of Cu, Al or Mo, weighed and preheated to 80° C for several hours. Afterwards the sample will be weighed again and noble gass spectroscopy will be used to measure the amount of ^{40}K and ^{40}Ar in the sample.

3.11.2   Assumptions for valid dating of clay minerals

To date clay minerals using K-Ar dating, the following assumptions must be satisfied (Zwingmann, 2014):

- The clay minerals must behave as a closed system. The system should not have lost any radiogenic ^{40}Ar produced by decay of ^{40}K.

- The radiogenic ^{40}Ar should only be produced by decay of ^{40}K. No ^{40}Ar should have been incorporated into the mineral after its formation.

- The atmospheric ^{40}Ar should be adjusted to the present-day ^{40}Ar/^{40}Ar value of 295.5.

There have been concerns that preferential loss of radiogenic ^{40}Ar due to grain size reduction give inaccurate results when dating fault gouge, as the age data normally decreases with decreasing grain sizes (Clauer, 2013). However, it has been shown that variations in mineral composition is the cause, as recrystallisation during fault movement produces higher portions of authigenic particles within the finer grain sizes, resulting in younger ages.

4 Methodology

4.1 Field work

Several locations within the study area were mapped with respect to deformational products, orientation of faults and striations, in addition to variations in mineralogy and texture (see fig. 15). When mapping kinematic indicators, joints, non-striated shear fractures and striated shear fractures were measured using a Brunton TruArc 15 compass. Both dip-direction and dip were logged. Kinematic indicators were mapped at locations 1, 5, 8, 13, 15, 16, 20, 21, 22, 23, 24, 27, 28, 31 (see fig. 15). In addition, a total of 19 samples were collected in the study area to examine the variability of mineralogy and texture. The samples were collected at different distances from the center of the fault core, at locations 1, 5, 6, 8, 9, 10, 11, 12, 14, 16, 26 and 29. When mapping the study area, all field notes and measurements were logged using FieldMove on an Apple iPad.

4.2 Sample preparations for K-Ar geochronology

Four samples of fault gauge and fault breccia were collected from among the brittle structural facies found in the fault core. These were used for K-Ar geochronology and had a sample weight exceeding 300 g. Special care was taken to avoid mixing of material from the different brittle structural facies. Preparation of the samples for K-Ar geochronology was performed at the laboratories of the Geological Survey of Norway (Trondheim, Norway), following the routines described by Viola et al., 2018. The samples were gently disintegrated by placing the samples in beakers containing alcohol and performing repeated freezing and thawing cycles. The process takes approximately a month and is performed to avoid artificial grain size reduction and contamination of coarser grained material within the finer sized fractions. The samples were then separated in five grain size fractions ($<$0.1 μm, 0.1 - 0.4 μm, 0.4 - 2 μm, 2 - 6 μm and 6 - 10 μm). Grain size fractions of 2 - 6 μm and 6 - 10 μm were separated in distilled water using Stokes' law, wereas the finer fractions ($<$0.1 μm, 0.1 - 0.4 μm and 0.4 - 2 μm) were obtained by high speed centrifugation.
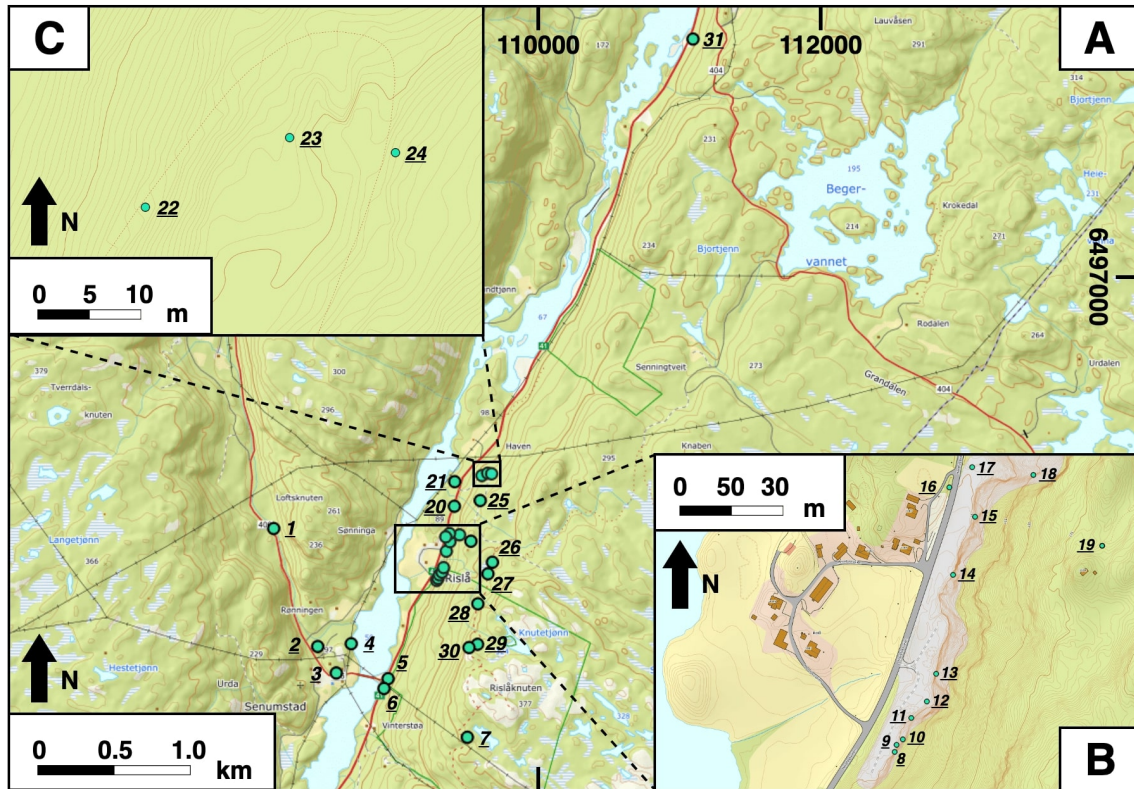
Figure 15: Overview map showing the localities in the study area. The Rislå outcrop has been enlarged in subfigure B and the area around a large quartz vein has been enlarged in subfigure C. A topographical map with contour lines has been used as background and coordinates are in UTM zone 33.

4.3   3D model

A 3D model of Rislå was produced to help present the outcrop, where a drone was utilized to take photos of the outcrop surface. A cloud of three dimensional point data was then imported to CloudCompare, which produced a virtual 3D model. A plugin within Cloud-Compare called FACETS was used to map the outcrop surface, so that the orientations of the different fracture sets could be quantified. The orientations of the fractures were then presented on a stereonet, in addition to presenting models of the outcrop, where the different fracture sets were highlighted.

4.4 Microscopy and mineralogical analysis

A total of 15 collected samples were given to the thin section laboratory at IGP, NTNU, which produced 15 thin sections. The mineralogy of the samples were studied using a Nikon ECLIPSE Ci-POL petrographic optical microscope, in addition to using a Olympus BX51 Fluorescence Optical Microscope for scanning of the thin sections. Several characteristics were used to identify minerals, including grain shape, colour, pleochroism, cleveage, relief, interference colours, extinction angle and twinning. Both mineral descriptions from Sørensen, 2015 and comparisons to example thin sections containing specific minerals were used for mineral identification. Supervisor Per Terje Osmundsen also

Figure 16: Olympus BX51 Fluorescence Optical Microscope used for scanning of thin sections.

provided some useful inputs on how to identify different deformational products, like sericitic alteration and cataclasis. To estimate the percentage distribution of minerals for each sample, scan-images of the thin sections, provided by the Olympus BX51 Fluorescence Optical Microscope, were compared to estimation charts of mineral content for rocks and sediments, provided by Bureau of Reclamation, 1991.

5 Results

This chapter presents the results from the field work at the Rislå outcrop and surrounding areas. Results from the scanlines and the 3D modelling of the outcrop will also be presented, in addition to displaying the results from the mineralogical analysis of the samples, produced using a petrographic optical microscope. The dates acquired from the K-Ar geochronology and the mineralogy of the collected samples acquired from XRD analysis, preformed at NGU, will also be presented. The results will later be discussed within the discussion chapter.
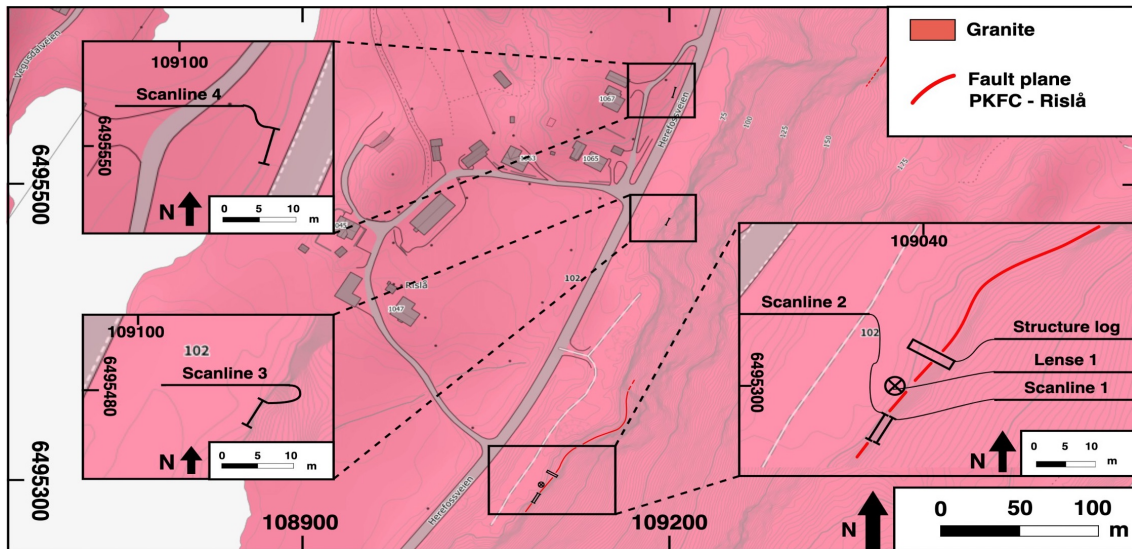
Figure 17: Overview map of the Rislå outcrop, where the locations of the measured scanlines, fault lense and structure log have been marked. See fig. 19 for an overview of the structure log. Figure 23, 24 and 25 show an overview of the variations of fracture frequency and orientations along the scanlines. Coordinates in UTM zone 33.

5.1 Fault geometry, architecture and associated structural facies of the PKFC

As shown in fig. 1 and 17, this study was mainly performed at an outcrop found within the Herefoss-granite (6495383 N, 109065 E, UTM zone 33), located in the Agder area. The fault (PKFC) measured at this outcrop is marked by a relatively undulating, steep (dip: $62 \pm 2°$; n = 3), ESE-dipping fault plane (strike: $32 \pm 2°$; n = 3). Several secondary faults of unknown displacement with development of fault gouge was observed trending approximately north - south (strike: $0 \pm 23°$; n = 2). These secondary faults were less steeply dipping, compared to the fault plane of the PKFC (dip: $25\pm9°$; n = 2). The areas around the PKFC also contain several smaller fault planes with belonging striations.
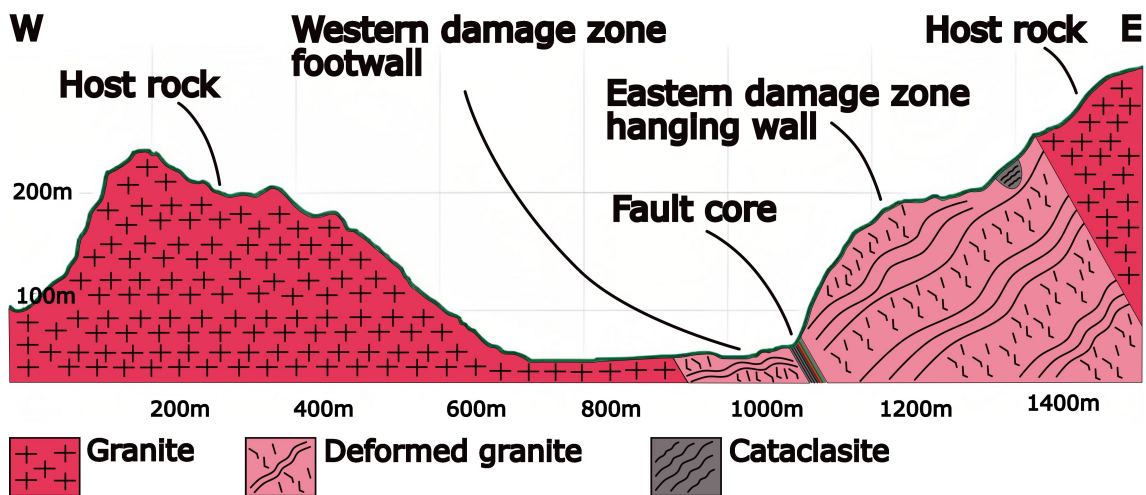
Figure 18: Cross section cutting through the study area, showing damage zones, fault core and undeformed zones of granite. The cross section is oriented west-east and the fault core is not to scale. A more detailed cross section of the fault core is presented in figure 19.

The studied section of the PKFC consists of a single high-strain fault core bounded by damage zones, as shown in fig. 18. The damage zone located in the hanging wall lies ESE of the fault core and has a thickness of 370 - 510 m. It consists of a deformed coarse grained, porphyritic and homogeneous granite, where the K-feldspar crystals has a strong red colour and is weakly foliated at some places (see fig. 20G). The colour of the K-feldspar crystals is gradually transitioning to a light pink colour with increasing distances from the fault core. These K-feldspar crystals are enclosed by hydrothermal quartz, which is gradually disappearing in the distal parts of the hanging wall, away from the fault core. Some matte coloured white plagioclase crystals were also found in the more distal parts of the damage zone. The hydrothermal quartz and the strong red colour of the K-feldspar crystals indicate that the granite has experienced tectonic deformation, as both occurrences are associated with circulation of hydrothermal fluids. There is chlorite mineralisation on the surface of a small portion of the shear fractures and some of the K-feldspar crystals are enclosed by epidote. A large quartz vein in vicinity of the fault core cuts through the hanging wall, with a width of several meters. A zone of cataclasite occurs at the eastern end of the hanging wall, farther away from the fault core, as shown in fig. 18.

The damage zone located in the footwall lies WNW of the fault core and has a thickness of 60 - 280 m. It consists of a deformed coarse grained, porphyritic and homogeneous granite, where the K-feldspar crystals have a strong red colour and are weakly foliated at some places. Unlike the hanging wall, the K-feldspar crystals in the footwall are not enclosed by hydrothermal quartz, even though there still is quartz in the granite. The

40
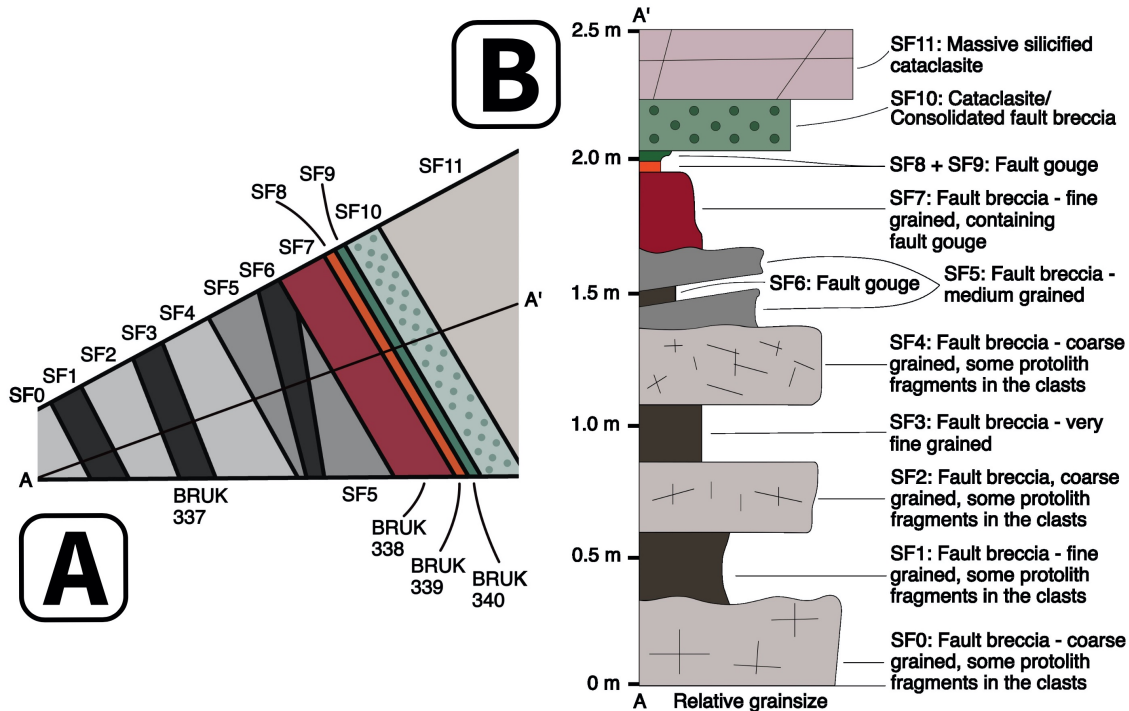
Figure 19: Subfigure A shows a cross section measured perpendicular to the fault plane of the PKFC at Rislå, oriented west-northwest - east-southeast. The cross section consist of 12 brittle structural facies, marked SF0 to SF11. The locations of the samples collected for the K-Ar geochronology and XRD mineralogical analysis (BRUK 337, 338, 339 and 340) have been annotated. The line marked A to A' indicates the orientation of the structure log, shown in subfigure b. The structure log shows the relative grain sizes of the brittle structural facies on the x-axis and the distance along the cross section on the y-axis. Lines and dots are used to represent fractures and clasts, respectively.

strong red colour of the K-feldspar crystals still indicates that the granite has experienced tectonic deformation, even with the lack of hydrothermal quartz (see subchapter 3.7). The amount of biotite throughout the damage zone varies and biotite often encloses the K-feldspar grains. A zone of dark green greyish homogeneous and massive cataclasite is located close to the fault core with epidote mineralisation at the surface of the shear fractures. There are also some occurrences of chlorite within this cataclasite.

The fault core, which is a 2.5 - 5 m thick composite brittle structure is comprised of 12 juxtaposed, but not necessarily coeval brittle structural facies (see fig. 19 and 20). In the middle part of the fault core there are three brittle structural facies with sharp, fault-parallel contacts; uppermost is a zone of greenish grey fault gouge (SF9, fig. 19), in the middle a zone of dark red/orange fault gouge (SF8, fig. 19) and lowermost a zone of dark red/purple fault breccia (SF7, fig. 19). The contact between the greenish grey fault gouge and the overlying cataclasite is sharp, while the contact between the dark red/purple fault

41
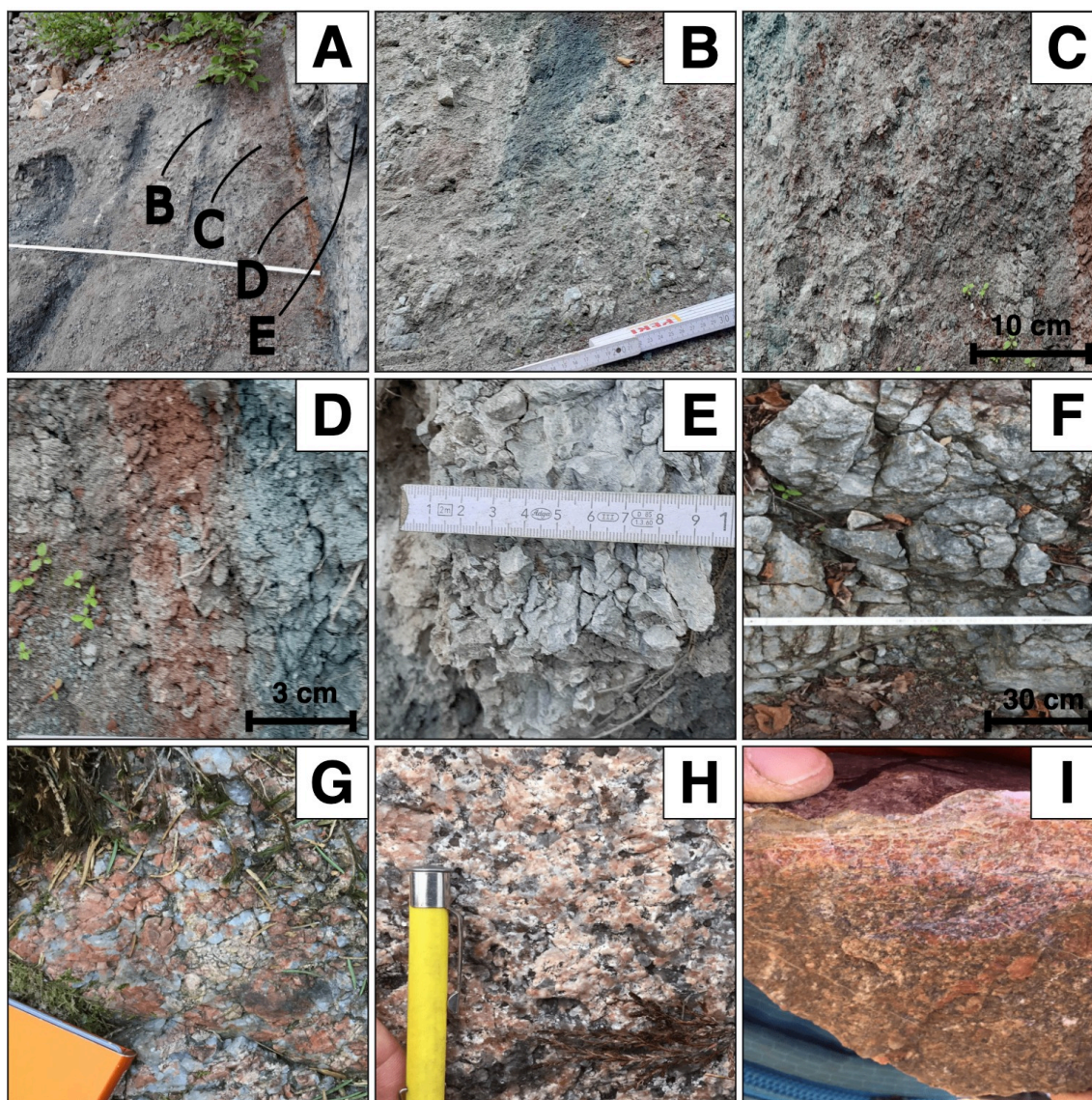
Figure 20: A) Overview photo of the cross section through the fault core of the PKFC, located at the Rislå outcrop, where subfigure B, C, D and E have been annotated. B) Brittle structural facies SF5 + SF6. C) Brittle structural facies SF7. D) Brittle structural facies SF8 + SF9. E) Brittle structural facies SF10. F) Fault lense located in the lower part of the fault core. G) Deformed granite located in the hanging wall damage zone. The feldspar grains are encircled by hydrothermal quartz. H) Undeformed granite found near the edge of the hanging wall damage zone, at Rislåknuta. I) Cataclasite with epidote mineralization found south in the study area, east of Boen brigde.

breccia and the underlying faultbreccia of SF5 is gradual. The zone of greenish grey fault gouge has a width of 1 - 4 cm, while the zone of dark red/orange fault gouge has a width of 1.5 - 4 cm. The zone of dark red/purple fault breccia has a width of 21 - 23 cm and has a clast size of less than 2 cm.

Above the greenish grey fault gouge of SF9, in the upper part of the fault core, there is a 10 - 25 cm thick layer of cataclasite, containing clasts with grain sizes smaller than 2 cm. This brittle structural facies is marked as SF10 in fig. 19 and can also be interpreted as a cohesive breccia. SF11, located above SF10, consists of a light grey to white massive, silicified granite that has been cataclasticly deformed. SF11 continues upwards in the hanging wall and it is unknown exactly where the fault core ends and the hanging wall begins.

The lower part of the fault core alternates between zones of coarse grained and fine grained fault breccia, with the latter containing fault gouge. The zones of coarse grained fault breccia are found in SF0, SF2, SF4 and SF5, see figure 19. They have a light grey colour and the grain sizes of the clasts are decreasing towards the center of the fault core; SF0 contain clasts between 3 - 15 cm, SF2 between 0.5 - 9 cm, SF4 between 0.5 - 12 cm and SF5 smaller than 4 cm. These clasts mainly consist of cataclasite, but some fragments of quartz and K-feldspar from the protolith are still distinguishable. The width of these zones are fairly homogeneous, where SF5 is 24 cm, SF4 is 24 cm, SF2 is 21 cm and SF0 is 25 cm. These coarse grained fault breccias have then been cross cut by several zones of dark, fine grained fault breccias that are found in SF1, SF3 and SF6, containing variable amounts of fault gouge (see fig. 19). The grain sizes of the clasts are decreasing towards the middle of the fault core, with SF1 containing clasts between 1 - 6 cm, SF3 between 1 mm - 8 cm and SF6 smaller than 2 cm. The width of these zones are also decreasing towards the middle of the fault core, where SF1 is 20 cm, SF3 is 17 cm and SF6 is 11 cm. The portion of fault gouge is increasing towards the middle of the fault core. The contacts between the zones of coarse grained and fine grained fault breccia are sharp with exception of the SF0 - SF1 contact, which is gradual. It is also worth noticing that SF6 is cross cutting at a different angle from the other brittle structural facies.

The dark, fine grained fault breccias found in SF1, SF3 and SF6 are not continuous along the strike of the measured fault core and are gradually thinning and dissipating over a distance of 2 - 3 meters towards south. The coarser fault breccias found in SF0, SF2, SF4 and SF5 are simultaneously merging together to form a fault lense, consisting of a fault breccia containing larger clasts compared to the fault breccias mapped along the cross section. The fine grained fault breccia and fault gouge of SF7, SF8 and SF9 are continuous along the strike of the measured fault core, but with some variations in thickness.

5.2 Kinematic indicators in the study area

Joints, non-striated shear fractures and striated shear fractures were measured at several locations around the study area. These were then presented on five stereonets, based on their locations, as shown in figure 21. **Stereonet 1** presents measurements of striated shear fractures measured south in the study area, east of the Senumstad bridge, Birkeland (6494661 N, 108649 E, UTM zone 33). They were measured at a cataclasite with a 2 - 4 mm thick, dark, fine grained layer of epidote mineralisation located on the surface. All striated shear fractures in group 1 were measured in proximity of each other, within a radius of 5 meters. **Stereonet 2** presents measurements of striated shear fractures measured north at the Rislå outcrop (6495530 N, 109139 E, UTM zone 33), see figure 21. Measurements were done both east and west of the Herefoss road and all of the measurements were located west of the PKFC fault core. The striated shear fractures were measured at a deformed, fine grained granite with no visible mineralisations at the surface. **Stereonet 3** presents measurements of striations measured within the PKFC fault core, south at the Rislå outcrop (6495291 N, 109033 E, UTM zone 33). **Stereonet 4** presents measurements of joints, non-striated shear fractures and striated shear fractures measured in the terrain north and east of the Rislå outcrop. The measured areas consist of granite with various degrees of deformation. **Stereonet 5** presents measurements of joints, non-striated shear fractures and striated shear fractures measured at an outcrop north in the study area (6498601 N, 111041 E, UTM zone 33). The majority of the fractures (11 fractures) were measured at a cataclasite located north at the outcrop, containing small inclusions of fluorite. A smaller amount of fractures (5 fractures) were measured at a pale K-feldspar-rich rock, also containing small inclusions of fluorite, which was located west at the outcrop.

In general, the measured striated shear fractures are dominated by subhorizontal and oblique oriented striations, while there still are some occurrences of subvertically oriented striations. Downstepping generally indicate a sinistral oriented slip movement. The majority of the measured shear fractures presented in **stereonet 1** are dipping northeast to southeast and the striations are dominated by subhorizontal and oblique orientations (see fig. 21). The majority of the measured striated shear fractures presented in **stereonet 2** are dipping west and the striations are dominated by subhorizontal orientation where downstepping on three of the striated shear fractures indicate sinistral slip movement. **Stereonet 3** presents striations measured in the fault core of the PKFC, where three striations were measured within the cataclasite located in the hanging wall, at SF10 and SF11, with a subhorizontal orientation. A subvertically oriented striation was measured within the fault gouge, at the SF8/SF9 contact (see fig. 19). The measurements presented in **stereonet 4** are dominated by joints, non-striated shear fractures and striated shear fractures dipping east, with a smaller group of striated shear fractures dipping west. The striated

shear fractures are dominated by subhorizontal and oblique orientation, where downstepping on one of the striated shear fractures indicate sinistral oblique slip movement. The measurements presented in *stereonet 5* are dominated by striated shear fractures dipping west to northwest, with a smaller group of joints and shear fractures dipping northeast. The majority of the striated shear fractures have subhorizontally oriented striations, where downstepping on one of the striated shear fractures indicate sinistral oriented slip movement. Some subvertically oriented striations were also measured, but were only found within the cataclasite (see fig. 21).
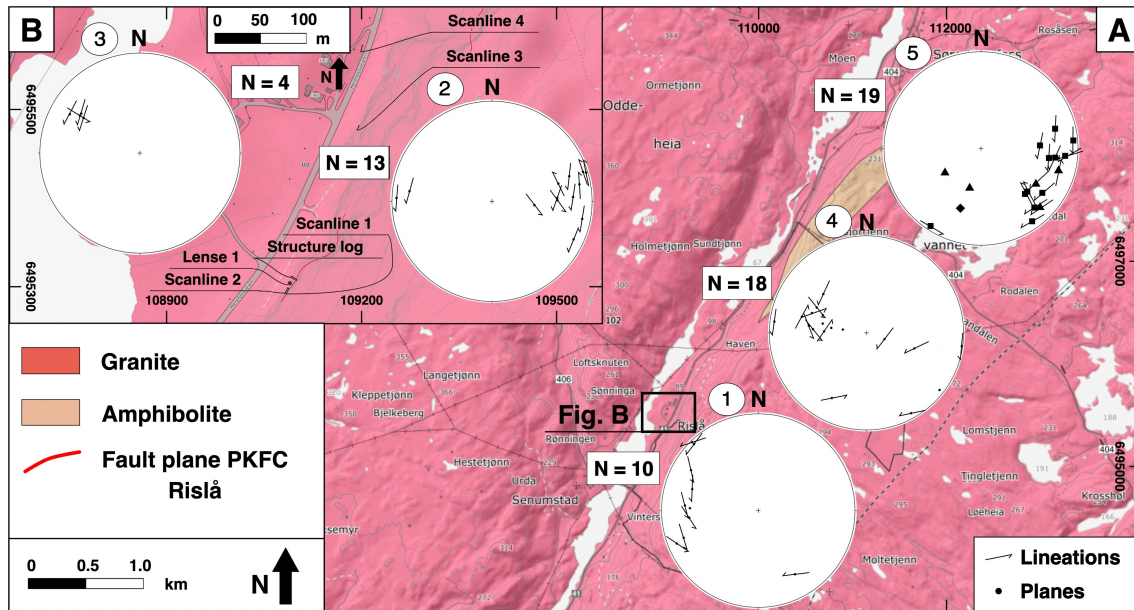
Figure 21: Stereonets 1 - 5 plot the dominant orientations of joints and non-striated shear fractures (dots) and striated shear fractures (dots with slip-linear line): 1) Striated shear fractures measured south in the study area (6494661 N, 108649 E, UTM zone 33). 2) Striated shear fractures measured north at the Rislå outcrop. Measurements were done both east and west of the Herefoss road and all of the measurements were located west of the PKFC fault core. 3) Striations measured within the PKFC fault core, south at the Rislå outcrop. 4) Joints, non-striated shear fractures and striated shear fractures measured in the terrain north and east of the Rislå outcrop. 5) Joints, non-striated shear fractures and striated shear fractures measured at an outcrop north in the study area (6498601 N, 111041 E, UTM zone 33). Fractures measured at a cataclasite, north at the outcrop, are marked with squares, while fractures measured at a pale K-feldspar-rich rock, west at the outcrop, are marked with triangles. The measured contact between the cataclasite and the K-feldspar-rich rock is marked with a diamond.

5.3 Methodology and results of the measured scanlines and faultlense

Four scanline groups were measured with the intent of mapping variations in fracture frequency and orientations at increasing distances westwards of the hanging wall. In addition, the frequency and orientations of fractures in a fault lense located in the lowermost part of the fault core were measured. Scanline 1 was measured 0.49 m east of the SF9/SF10 contact, in the uppermost part of the fault core. It was measured on SF11 in the lowermost part of the hanging wall (see fig. 19) and has a distance of 1.1 m from scanline 2. Scanline 2 was measured on the lower part of SF10, adjacent to the SF9/SF10 contact. The fault lense was measured 1 m west of the SF9/SF10 contact, parallel along the fault core to SF1, SF2 and SF4 (see fig. 19). Scanlines 3 and 4 were measured further north at the Rislå ourcrop (see fig. 17) and have a shortest distance of 25 m and 42 m from the SF9/SF10 contact, which was calculated using trigonometric triangles.
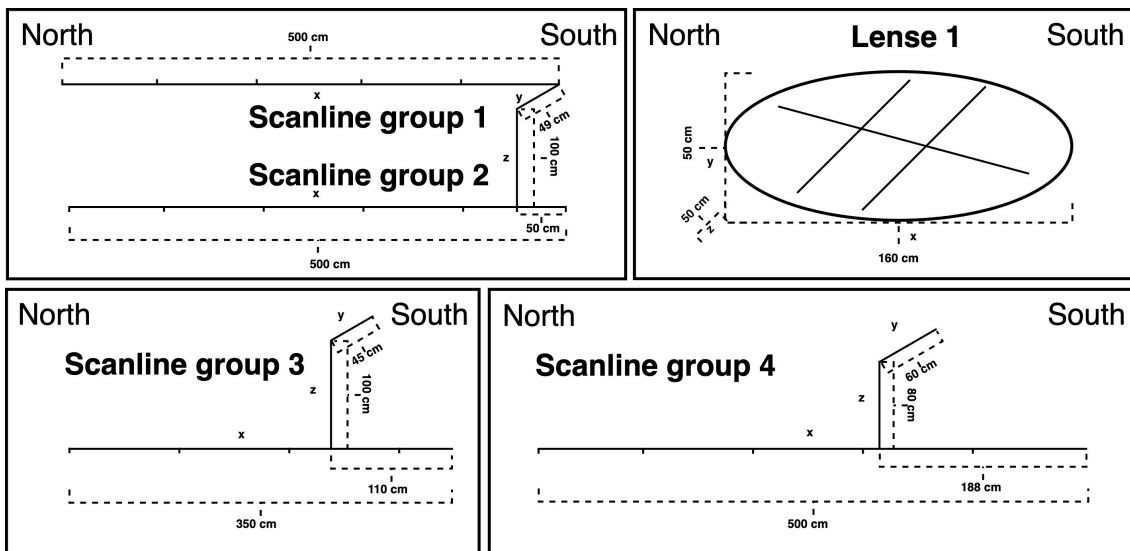
Figure 22: Overview figure showing the different lengths and orientations of the scanlines within the different scanline groups. The x, y and z-orientated scanlines are annotated with x, y and z, respectively.

Each scanline group was measured in three directions, x, y and z, so that the amount of fractures per m^3 could be calculated. The x-oriented scanlines of scanline group 1 and 2 were oriented parallel to the fault core of the PKFC, with a strike of $32° \pm 2°$. The x-oriented scanlines of scanline group 3 and 4 were oriented $77°$ northeast/ $257°$ southwest and $20°$ northeast/ $200°$ southwest, respectively. The y-oriented scanlines had a $90°$ angle in relation to the x-oriented scanlines and scanlines 1 + 2, 3 and 4 (y-orientation) were oriented $122°$ southeast/ $302°$ northwest, $167°$ southeast/ $347°$ northwest and $110°$ southeast/ $290°$ northwest, respectively. The z-oriented scanlines had a vertical orientation, with a dip of $90°$. The different lengths and relative orientations of the scanlines within the

46

scanline groups are shown in figure 22. The starting points of the x-oriented scanlines (0 cm) are located at the southern end. The longest scanline-orientation (x-orientation) were aligned parallel to the fault core because of the steep morphology of the outcrop, which made measurements of longer scanlines perpendicular to the fault core both infeasible and potentially dangerous. The measured fault lense is 1.6 m in x-direction (NNE-SSW), 0.5 m in y-direction (ESE-WNW) and 0.5 m in z-direction (vertical), as shown in figure 22. The fault lense was used to measure both the amount of fractures per m^3 and fracture orientations, while no scanline was measured because of its smaller size.
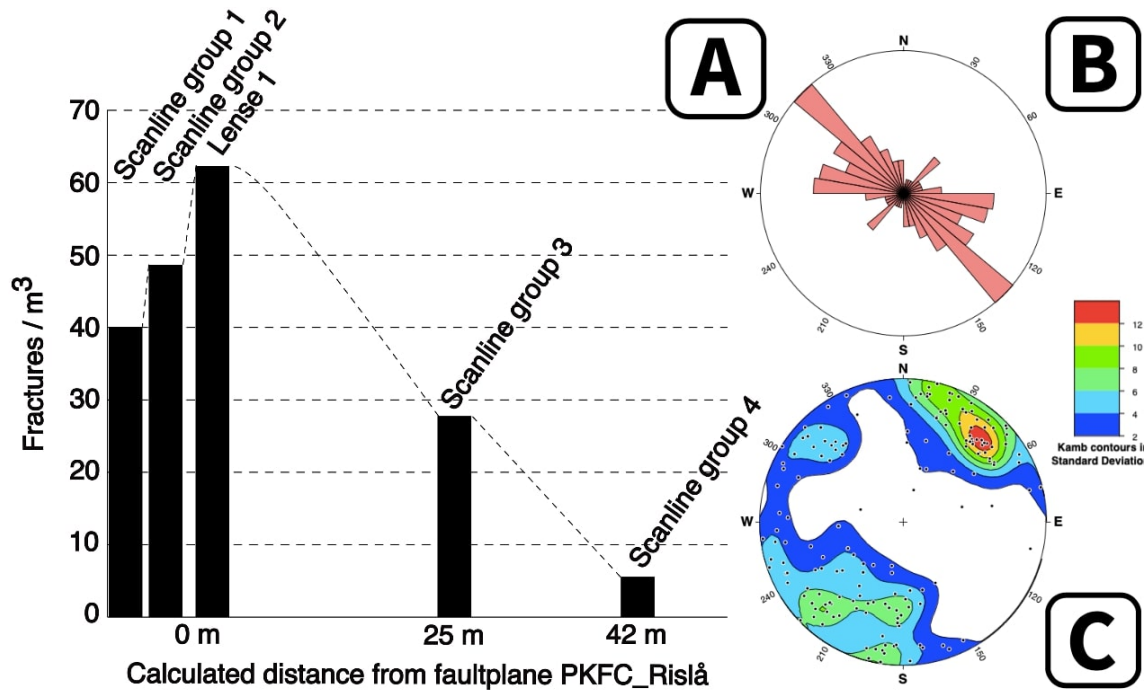
Figure 23: Subfigure A shows distance from the SF9/SF10 contact on the x-axis, while measured amount of fractures per m^3 is shown on the y-axis. The five bars represent the amount of measured fractures per m^3 at the measured scanline groups and fault lense. Subfigure B shows a rose diagram with the percentage distribution of strike of fractures at the measured scanlines and fault lense. Subfigure C shows a contour plot with the orientations of fractures at the measured scanlines and fault lense.

The measured scanlines and fault lense have uncovered a general trend of decreasing fracture density with increasing distances from the middle and lower parts of the fault core, as shown in figure 23A. The highest fracture frequency was recorded at the fault lense, in the lower part of the fault core. The fault lense consists of SF0, SF2 and SF4 merged together, as SF1 and SF3 are thinning and dissipating south of the cross section (see fig. 19). The fracture frequency is rapidly decreasing in scanline 1 and 2 in the upper part of the fault core, located in the hanging wall, that were measured on SF11 and SF10, respectively. The fracture density is also decreasing in scanline 3 and 4, although less
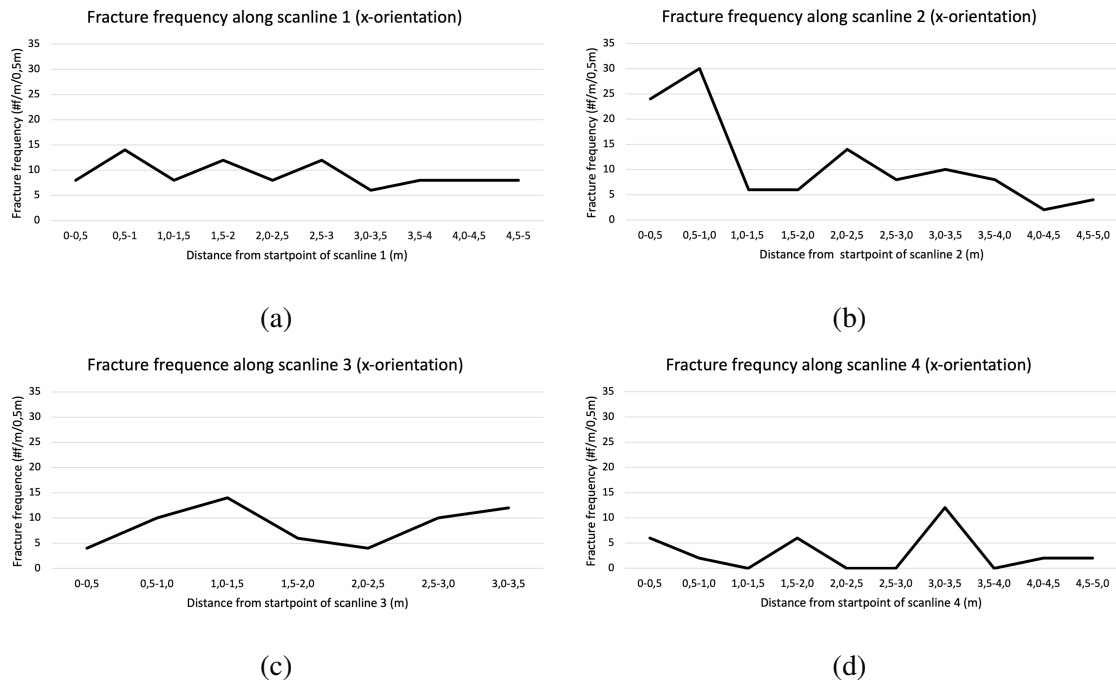
Figure 24: Plots of scanlines (x-orientation) that show meters from the starting point on the x-axis and frequency of fractures per meter given in intervals of 0.5 m on the y-axis. All the scanlines were recorded trending NNE-SSW, which is parallel with the fault core, and the starting points are located at the southern end.

rapidly. As shown in subfigure 23B and 23C, the fractures are mainly oriented northwest - southeast, with a main orientation of fractures trending 310° - 320° NW to 130° - 140° SE. However, figure 25 shows that the main orientations of fractures for scanline 1 and 4 are trending west - east. Figure 24 shows variations in fracture frequency along the measured x-oriented scanlines. The fracture frequencies along scanline 1, 3 and 4 are fairly homogeneous, while scanline 2 has a higher fracture frequency at the southern end of the scanline.

(a) (b) (c) (d)

(e)
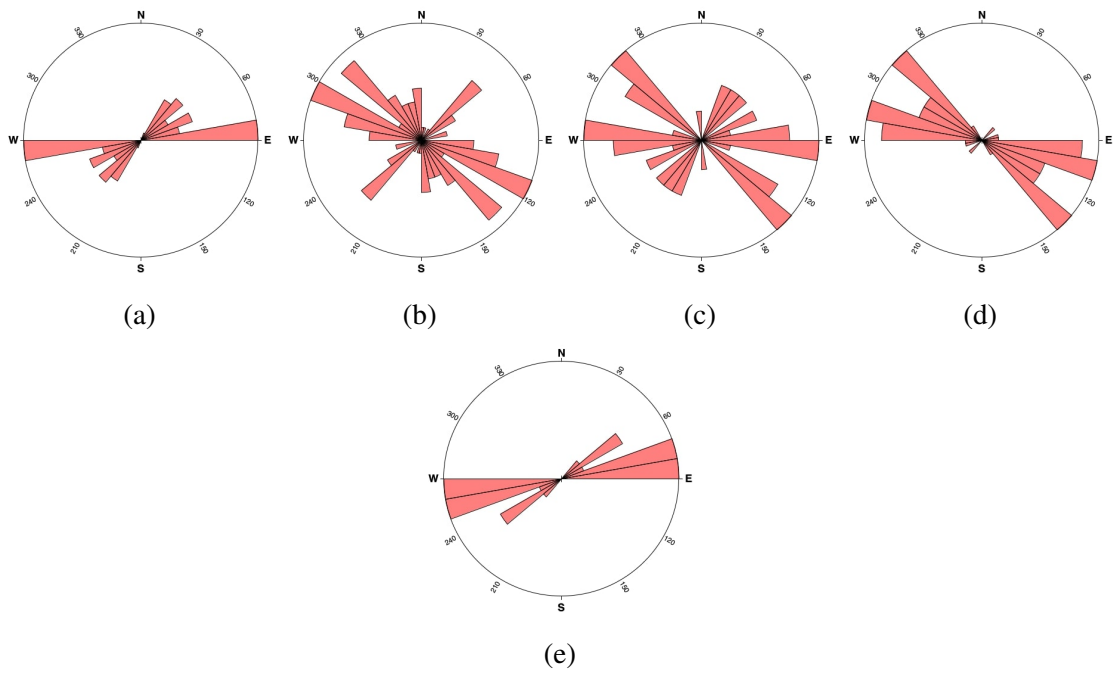
Figure 25: Rose diagrams showing the percentage distribution of strike of measured fractures at the scanline groups and fault lense: (A) Scanline 1, (B) Scanline 2, (C) Fault lense 1, (D) Scanline 3, (E) Scanline 4.

49

5.4   3D modelling and digital fracture mapping of the Rislå outcrop

This subchapter will look at the fracture orientations within the fault core by digitizing fractures, using a 3D model. This model was produced from images of the outcrop, shot by a drone. The fracture orientations will then be compared to fracture orientations found in similar studies within the discussion chapter.

A rose-diagram produced in CloudCompare, using the FACETS plugin, is presented in figure 26. The rose-diagram shows the dominant dip-directions of the measured fractures at the outcrop, where the red lines indicate a dominant dip-direction 291° towards west-northwest (stippled line, see fig. 26) and a dominant strike 201° south-southwest (fully drawn line, see fig. 26). The mean dip of the measured fractures are 65°. The number of fractures within an area of dip-direction is indicated by different colours, where white and blue indicate a lower number of fractures and green, yellow and red indicate a higher number of fractures. This is shown on the scale at the bottom of figure 26.
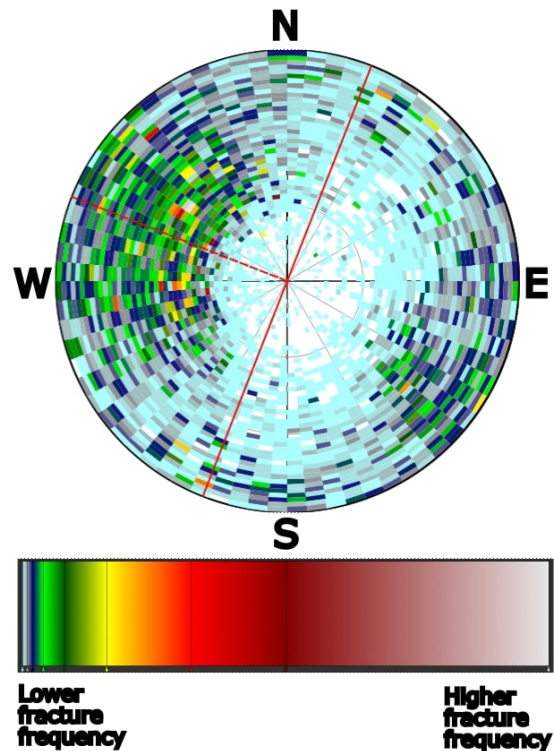
Figure 26:   Rose-diagram indicating the dominant dip-directions of the measured fractures at the outcrop. The colour scale at the bottom of the figure indicates the relative amount of fractures per area of dip-direction.

A specific area of the outcrop were selected for 3D modelling, where a significant amount of the hanging wall is exposed. The exposed area contains several distinctive fracture sets, creating distinguishable planar surfaces which can be mapped using the FACETS plugin. It is therefore valid to assume that these planar surfaces represent the different fracture sets at the outcrop. The rosediagram in fig. 26 shows that the majority of fractures are oriented subparallel to the fault core, with a very small amount of fractures oriented subperpendicular to the fault core. This is also shown in figure 27, were fractures oriented subperpendicular to the fault core are highlighted in subfigure A and fractures oriented subparallel to the fault core are highlighted in subfigure B.
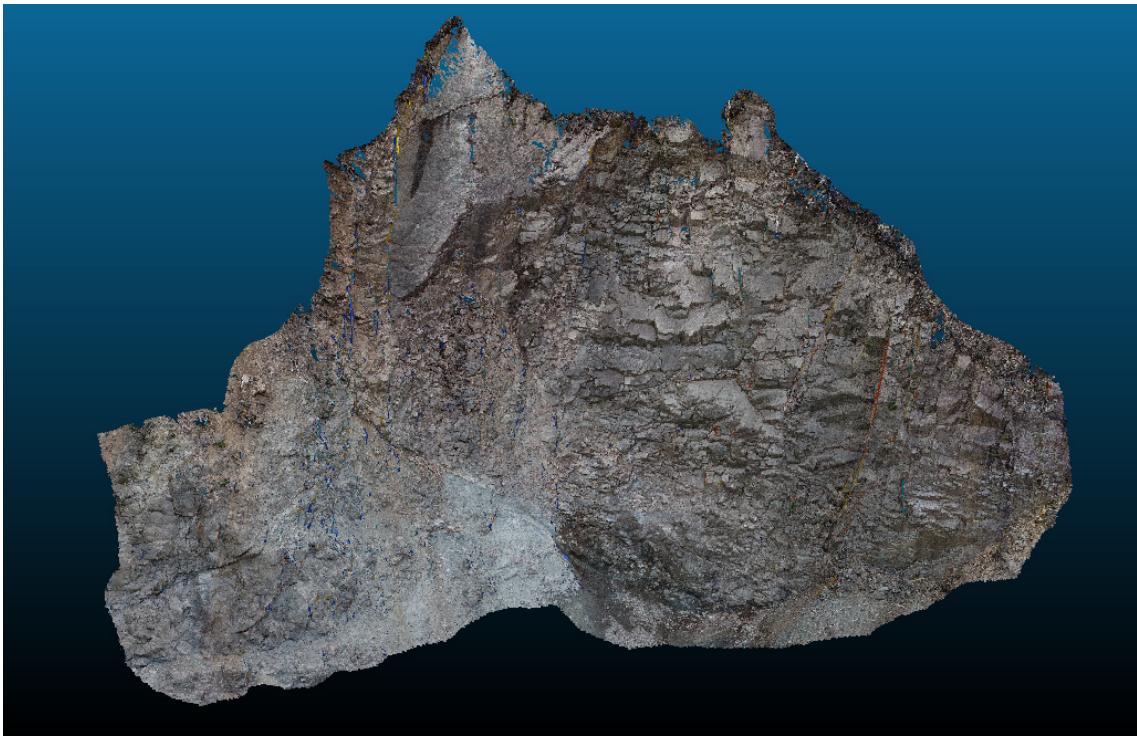
(a)
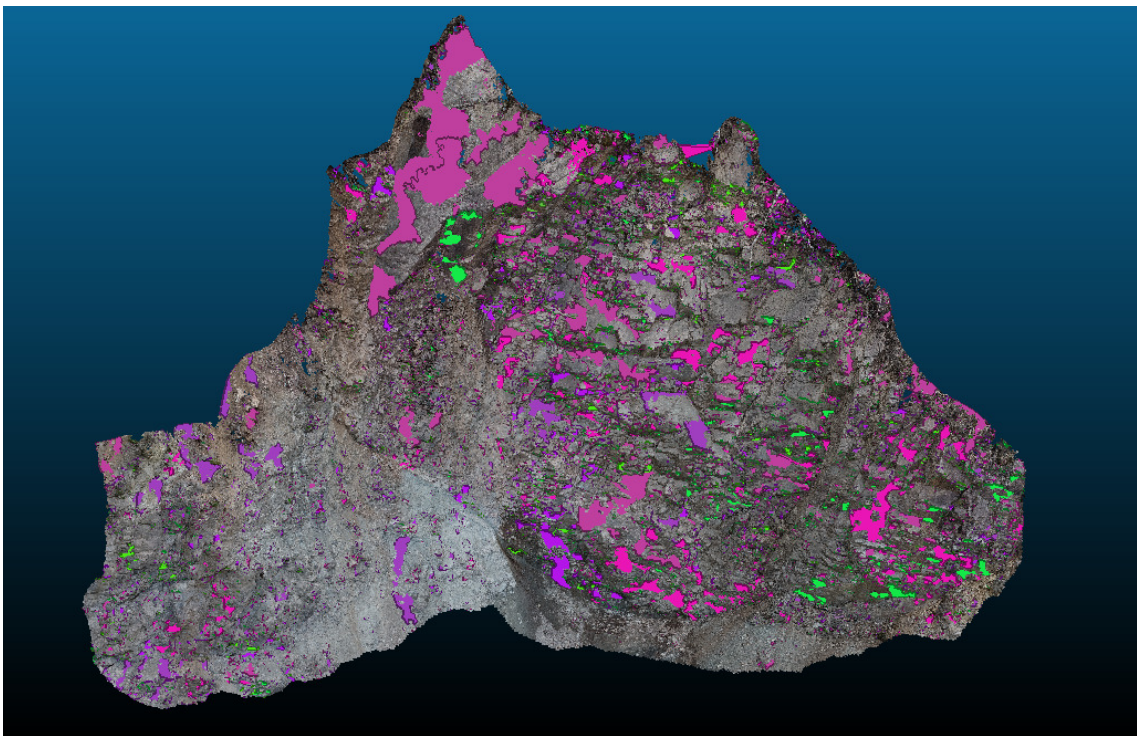
(b)

Figure 27: (a) Fractures subperpendicular to the fault core have been highlighted.(b) Fractures subparallel to the fault core have been highlighted. As shown above, a significantly larger portion of the fractures in the fault core are oriented subparallel with the fault core, compared to fractures oriented subperpendicular to the fault core.

5.5 Lineament populations within the Herefoss granite and surrounding gneisses

Lineament patterns along the Topdalselva topolineament were mapped manually, using vertical derivative filtered topographic maps presented in ArcGIS Pro. This produced a total of 1500 lineaments, using four different scales, which were presented using rose diagrams (see fig. 28). The two smallest scales of 1:20 000 and 1:50 000 were used to produce 500 lineaments each, while the two largest scales of 1:100 000 and 1:120 000 were used to produce 250 lineaments each. Maps with a resolution of 10 m were used together with the three smallest scales, while a resolution of 50 m was used together with the largest scale. As mapping lineaments with smaller scales is more time consuming, the smallest scale was only used for lineament mapping within the Herefoss granite. The three larger scales were used for mapping within both the Herefoss granite and the surrounding gneisses. Two dominant lineament-orientations were found within the study area; one NNE-SSW oriented trend and another WNW - ESE oriented trend (see fig. 28).
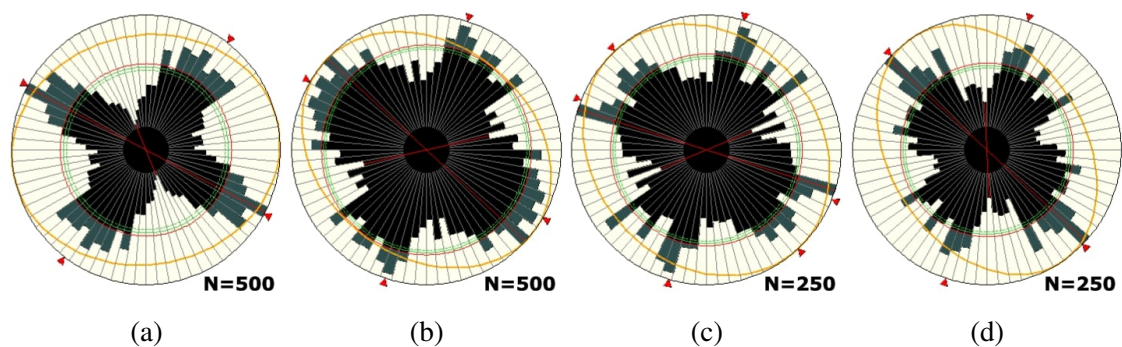
Figure 28: (a) Rose-diagram showing the orientations of lineaments mapped using a 10 m resolution map and a scale of 1 to 20 000. (b) Rose-diagram showing the orientations of lineaments mapped using a 10 m resolution map and a scale of 1 to 50 000. (c) Rose-diagram showing the orientations of lineaments mapped using a 10 m resolution map and a scale of 1 to 100 000. d) Rose-diagram showing the orientations of lineaments mapped using a 50 m resolution map and a scale of 1 to 120 000.

5.6 Optical microscopy analysis

This subchapter will describe the general trends of the mineralogy found in the study area. The mineralogy of the undeformed host rock (Herefoss granite) will be presented, in addition to analysing how the mineralogy changes with varying distances to the fault core. This will help to highlight the effects that faulting has on the mineralogy of the Herefoss granite. Different forms of deformation, like micro-brecciation and cataclasis, will also be presented.

5.6.1 Mineralogy of the host rock

Microscopical analysis of the host rock unveiled a mineralogy of quartz, ortoclase, plagioclase, microcline, biotite and hornblende in both the Western and the Eastern Facies of the Herefoss granite, as shown in figure 29. Muscovite was only found in the Eastern Facies. The Western Facies has a significantly larger percentage of microcline compared to the Eastern Facies and also contain somewhat more biotite and hornblende. On the other hand, the Eastern Facies have a significantly higher percentage of ortoclase and plagioclase. It was observed a large amount of sericitic alteration of feldspars in both the Western and the Eastern facies of the host rock, indicative of hydrothermal alteration. The biotite in the Eastern Facies has been partly chloritized, while the biotite in the Western facies is apparently unaltered.
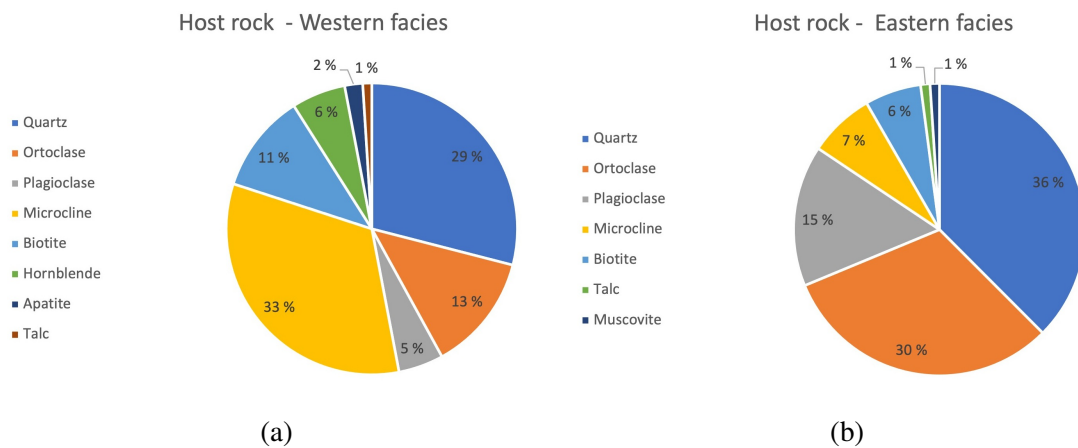
Figure 29: (a) Sector diagram presenting the mineralogy of the Western Facies of the Herefoss granite, with legend shown to the left. (b) Sector diagram presenting the mineralogy of the Eastern Facies of the Herefoss granite, with legend shown to the left.

5.6.2 Variability of mineralogy across the fault zone

Eight samples with varying distances to the middle part of the fault core were chosen to analyse variations in mineralogy across the fault zone, as shown in figure 30 and 31. END 18 (scanline 4) is located 42 meters west of the SF9/SF10 contact, while END 19 (scanline 3) is located 25 meters west of the SF9/SF10 contact. END 7 is located 8 meters west of the SF9/SF10 contact, END 6 lies 6 meters west of the SF9/SF10 contact, while END 5 and END 17 are located in the lower part of the fault core (see fig. 31). END 3 and END 4 are located in the upper part of the fault core.

Even though biotite is relatively abundant within the Herefoss granite (see fig. 29), it is generally lacking within the fault zone. Some biotite is found in END 18 (scanline 4) and END 19 (scanline 3), but the biotite here has been partly chloritized. For the other samples located within the fault zone, the biotite has been completely chloritized and only chlorite is found. Chlorite is however lacking within the hangingwall, with no chlorite found within samples END 3 and 4. There are very small amounts of feldspar in the hanging wall, with only a small amount within END 3 (SF10) and no feldspars within END 4 (SF11). The quartz content of the samples generally lie between 20% and 40%, while END 4 (SF11) has a much higher quartz content of c. 95%, as a result of silification. END 3 (SF10) is the only sample containing matrix and consists of a combination of clasts from the protolith and surrounding matrix. The matrix is deformed to such a degree that the minerals can not be distinguished using an petrographic optical microscope. Carbonates are found both in proximity and within the fault core, but are disappearing in END 18 (Scanline 4) and END 19 (Scanline 3), further away from the fault core. A large calcite vein was found in END 6, while smaller amounts of calcite was found within END 4 (SF11) and END 5 (SF0). Twinning of the e-plane occurs in the calcite, where thin twinning is slightly dominating, but also with a significant portion of thick twinning. Thin twinning appears as thin black lines when viewed parallel to the twin plane, while thick twinning viewed in the same way has a microscopically visible width of twinned material between the black lines (Ferrill et al., 2004).
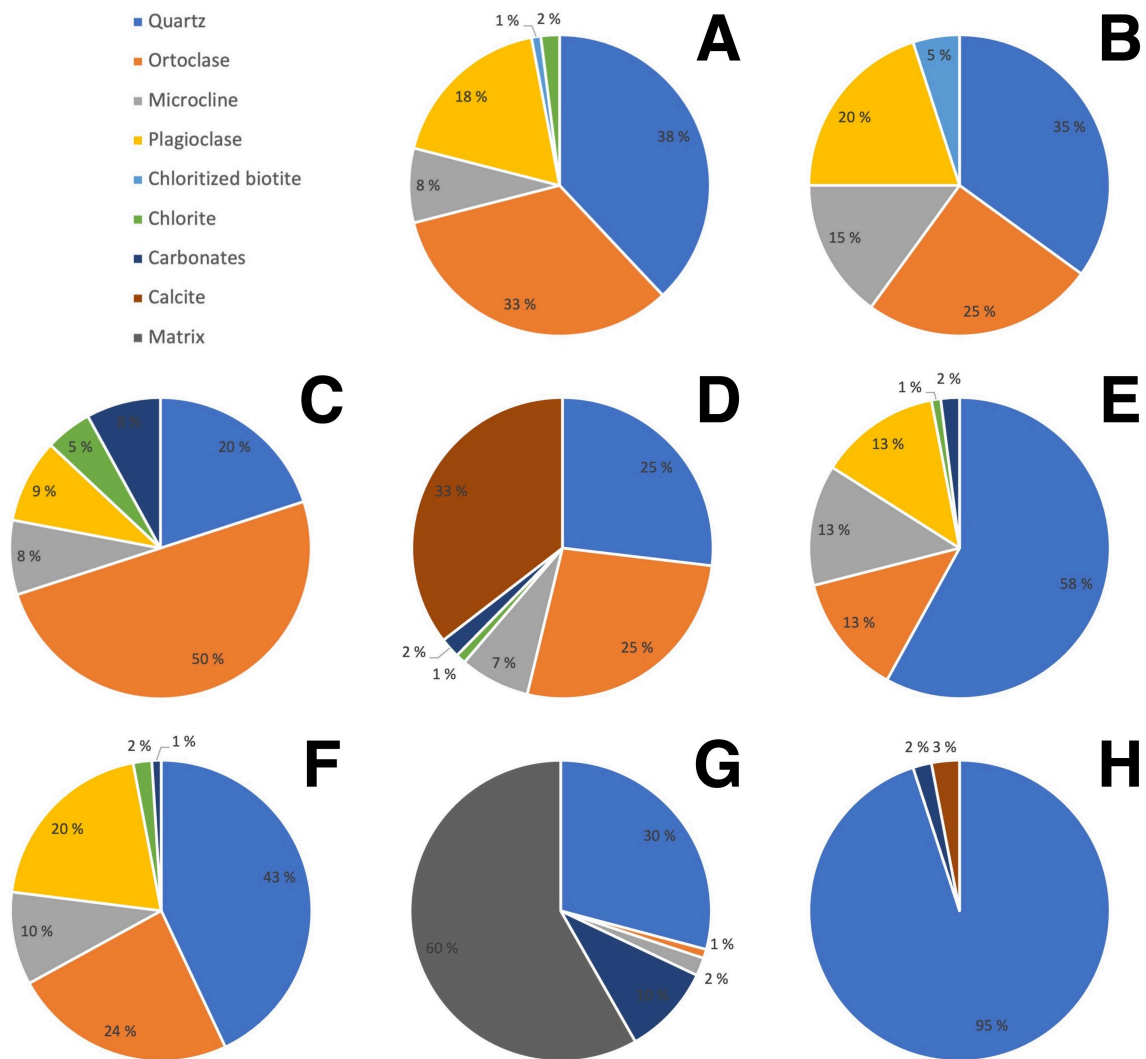
Figure 30: Mineralogical composition of the 8 samples located across the fault zone. A) END 18/scanline 4, B) END 19/scanline 3, C) END 7, D) END 6, E) END 5/SF0, F) END 17/SF4, G) END 3/SF10, H) END 4/SF11. Overview map of the locations of the samples is presented in figure 31.

5.6.3 Sericitic alteration of feldspars

The amount of sericitic alternation of feldspars throughout the fault zone is relatively homogeneous, with a slightly larger amount of sericitic alteration in the host rock, compared to the samples collected from the fault core and the damage zones. The amount of sericitic alteration within END 4 (SF11) is much lower, which probably is caused by high amounts of quartz and very low amounts of feldspars, as a result of silification. Estimating the amount of sericitic alteration within END 3 (SF10) is hard, as the matrix makes it difficult to detect sericitic overgrowth. The plagioclase crystals have generally undergone more sericitic alteration compared to the K-feldspars crystals, even though seritic alteration also is detected within both ortoclase and microcline. An example of sericiticic

55
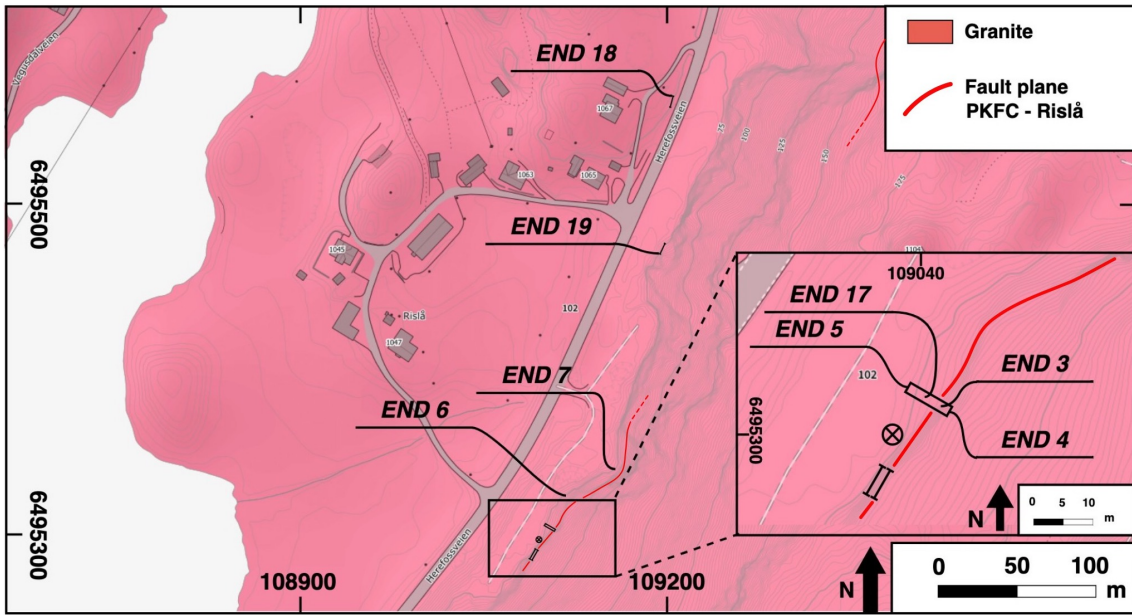
Figure 31: Overview map of the locations of the samples presented in figure 30.

alteration is shown in figure 32C.

5.6.4 Clasts of matrix confined by younger matrix

Several occurrences of clasts consisting of matrix, located within younger surrounding matrix was found in END 3 (SF10), as shown in figure 32D. These matrix clasts contain fragments of quartz and carbonates.
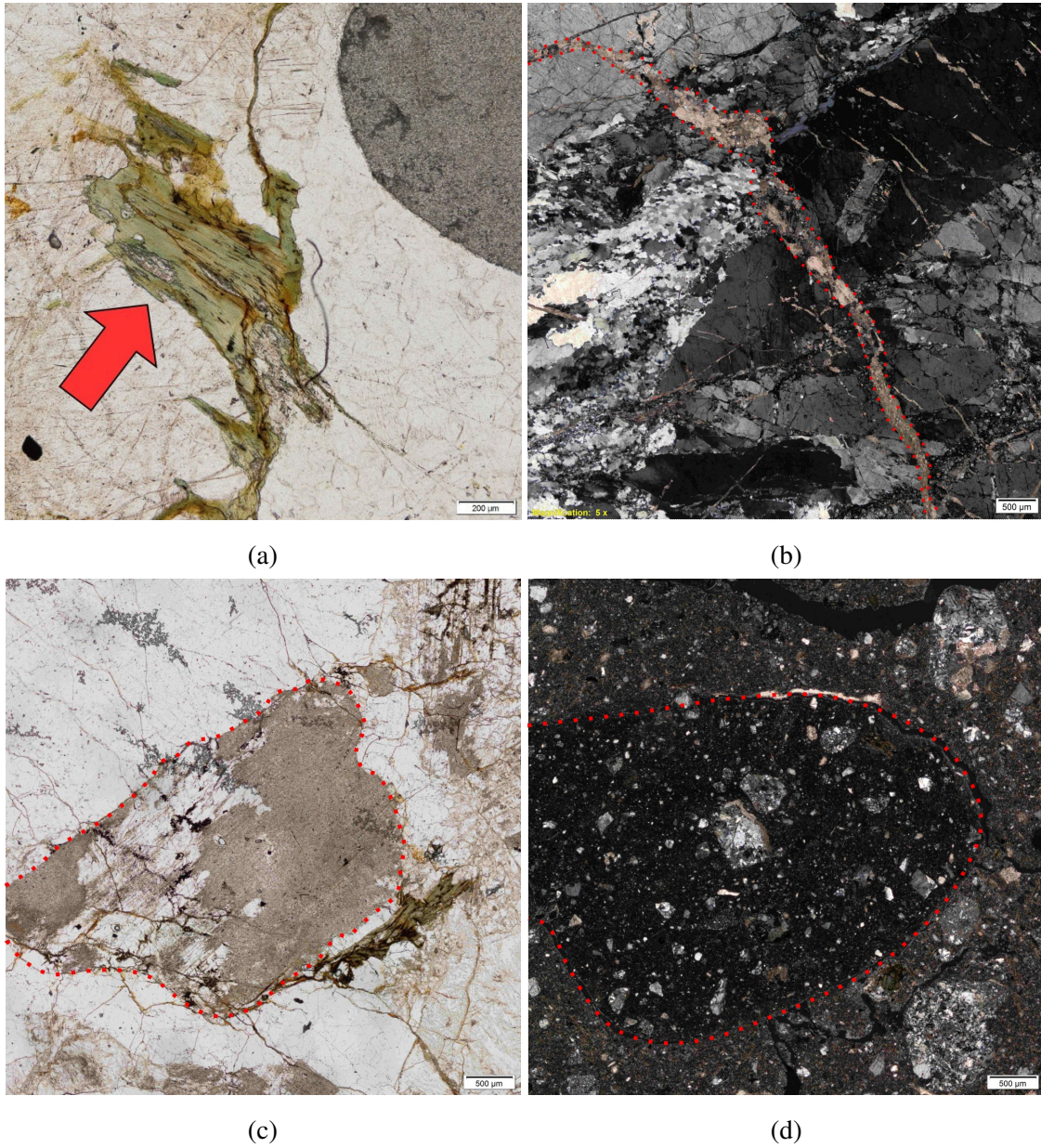
Figure 32: a) Chloritized biotite in END18/scanline 4. b) Carbonate vein in END 7. c) Sericitic alteration in END 12. d) Clast of matrix located within younger surrounding matrix in END 3/SF10.
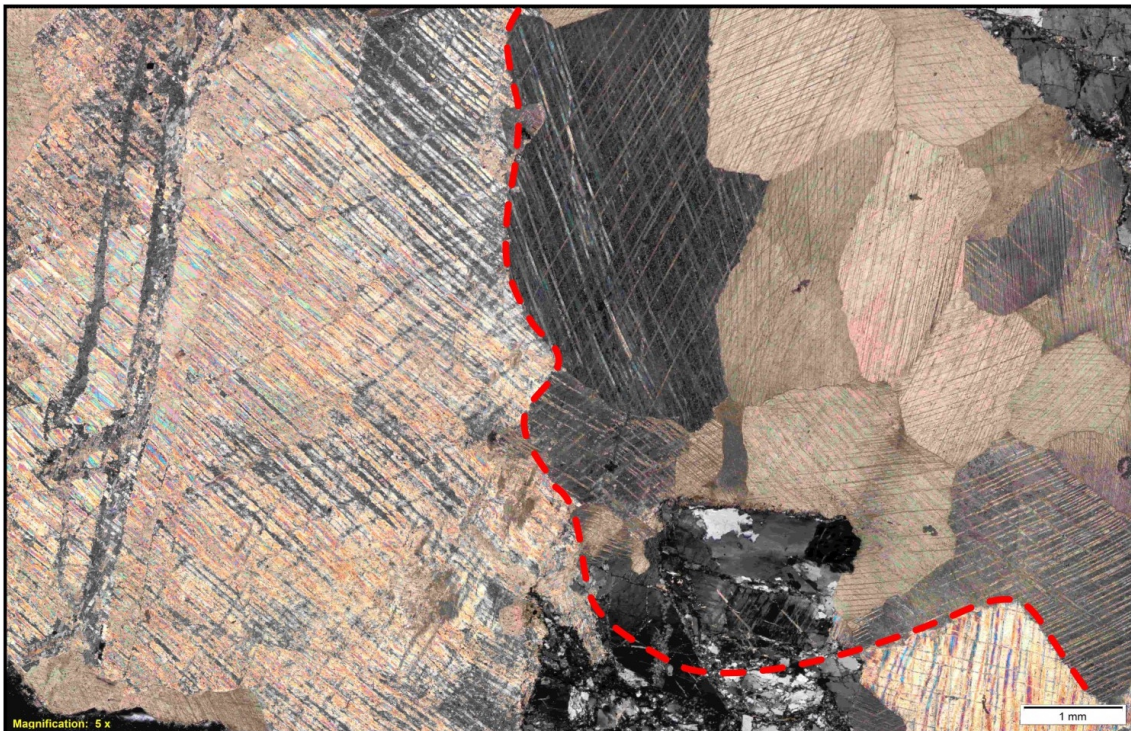
Figure 33: Twinning of the e-plane in a calcite vein located in END 6. Thick twinning is shown left of the red stippled line, while thin twinning is shown right of the red stippled line.

5.6.5 Micro-brecciation and ductile deformation of quartz

Micro-brecciation and ductile deformation of quartz grains occurs frequently within the samples found in the fault zone. The quartz grains are however completely undeformed within END 1 (Host rock, Western Facies), while they become gradually more deformed and recrystallized closer to the fault core with significantly reduced grain sizes. The quartz found in END 12 (Host rock, Eastern Facies) is less deformed with larger grain sizes, but some deformation do still occur. Examples of micro-brecciation and ductile deformed recrystallized quartz are shown in figure 34.

(a)   (b)
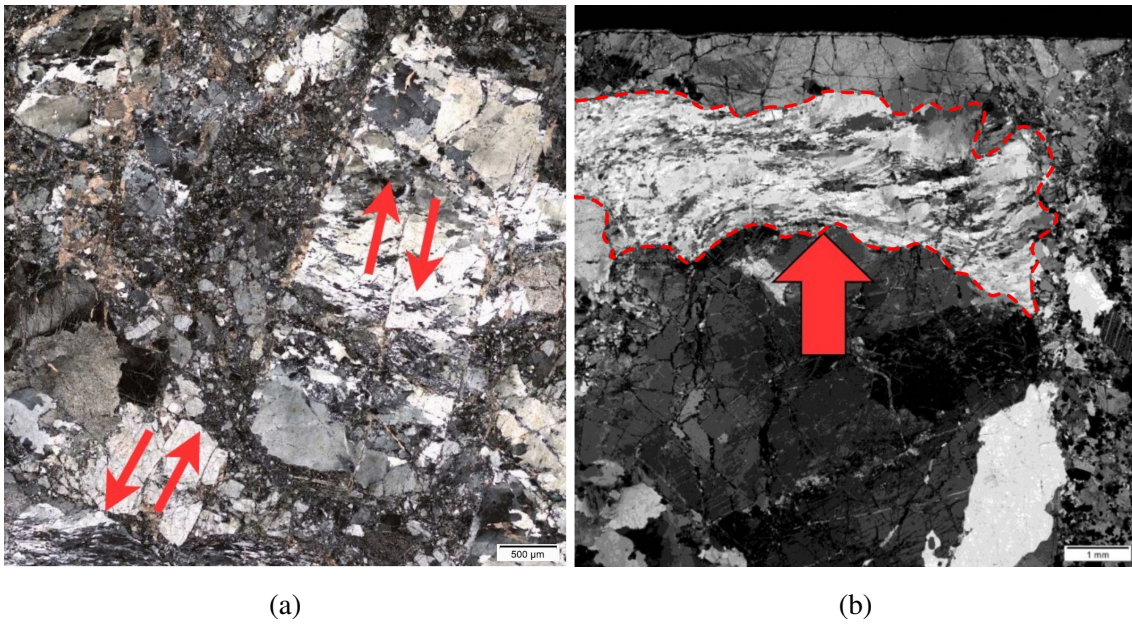
Figure 34: (a) Brecciation within END 5 with both dextral and sinistral displacement, marked with arrows. (b) Cataclastic deformation of quartz, marked with a red arrow and stippled line.

5.6.6 Key mineralogical descriptions

Sample name	Location	Key mineralogical descriptions
END 1	1	Sericitic alteration of feldspars occurs frequently.
END 2 (SF2)	10	Several smaller carbonate veins are found, with one large carbonate vein cutting through half of the thin section. Some sericitic alteration occurs with chloritization occuring in the same area of the thin section, located mostly along microfractures.
END 3 (SF10)	10	Contains a large portion of matrix, with aggregates of host rock minerals occurring frequently. Sericitic alteration of feldspars occurs and carbonates are found frequently.
END 4 (SF11)	10	Very fine grained quartz grains are abundant and several carbonate veins cut through the rock. Some areas of calcite also occurs and there is little sericitic alteration.
END 5 (SF0)	10	Several areas containing calcite, in addition to some carbonate veins. Sericitic alteration is abundant. There are some occurrences of chloritization.
END 6	11	Chloritization is abundant, typically occuring along micro-fractures. There are areas of cataclasis, where the quartz-grains have a reduced grain size. A large vein of calcite cuts through the thin section.
END 7	12	Chloritization is abundant, typically occuring along micro-fractures. Carbonates occurs frequently along microfractures.

Table 2: Key descriptions of the different mineralogical occurrences within the thin sections from the collected samples. See figure 15 for overview of the sample locations.

Sample name	Location	Key mineralogical descriptions
END 8	12	Chloritization of biotite is abundant. Long bands of deformed, fine grained quartz occurs.
END 9	6	Cataclasite: chloritization of biotite seems to have removed the biotite entirely. Large areas of matrix appears to be epidote, as the sample rock has a green coloured surface.
END 10	5	Cataclasite: contains a large portion of fine-grained, deformed quartz and dark matrix consisting of epidote.
END 11	26	Cataclasite: a large quartz-vein cuts through the thin-section. Sericitic alteration of feldspars is prominent outside the quartz vein.
END 12	29	Sericitic alteration of feldspars occurs frequently.
END 17 (SF4)	10	Sericitic alteration is relatively abundant and there are some occurences of chloritic alteration of biotite. Smaller carbonate veins occurs frequently, while one larger carbonate vein cuts through the thin section.
END 18	14	Sericitic alteration is relatively abundant and there are some occurences of chloritic alteration of biotite. No carbonates are found.
END 19	16	Small patches of sericitic alteration occurs frequently and chloritic alteration of biotite also occurs frequently. No carbonates are found.

Table 3: Key descriptions of the different mineralogical occurrences within the thin sections from the collected samples. See figure 15 for overview of the sample locations.

5.7 XRD results: mineralogy of the fault gouge and the fine grained fault breccias in the fault core

XRD analysis was preformed to find the mineralogical composition of the samples collected from SF3, SF7, SF8 and SF9 (see fig. 19), called BRUK 337, 338, 339 and 340, respectivly. BRUK 337 and 338 contained quartz, K-feldspar, plagioclase, illite/muscovite, chlorite, smectite and jarosite, while BRUK 339 lacked plagioclase (see fig. 35). BRUK 340 lacked both plagioclase and jarosite. Smectite was generally abundant in all the samples. BRUK 337 contained the most chlorite, while BRUK 339 and 340 containing the least amount of chlorite, indicating that the chlorite content is decreasing upwards in the fault core. BRUK 339 and 340 have a higher K-feldspar content compared to BRUK 337 and 338, indicating that the K-feldspar content is increasing upwards in the fault core. The illite/muscovite content of BRUK 337 is much lower than the other samples, which have a more similar percentage of illite/muscovite. BRUK 339 and 340 have a higher quartz content compared to BRUK 337 and 338, indicating that the quartz content of the samples is increasing upwards in the fault core.

In all the samples the main trend of the chlorite content is to increase with decreasing grain sizes, as shown in figure 36 and table 4. Smectite and illite/muscovite also has a general trend of increasing amounts with decreasing grain sizes, although the smectite is decreasing again in the finest fractions of BRUK 338. The illite/muscovite content is decreasing with decreasing grain sizes in BRUK 337. The jarosite content is increasing with decreasing grain sizes. The quartz, K-feldspar and plagioclase content is decreasing with decreasing grain size in all the samples.
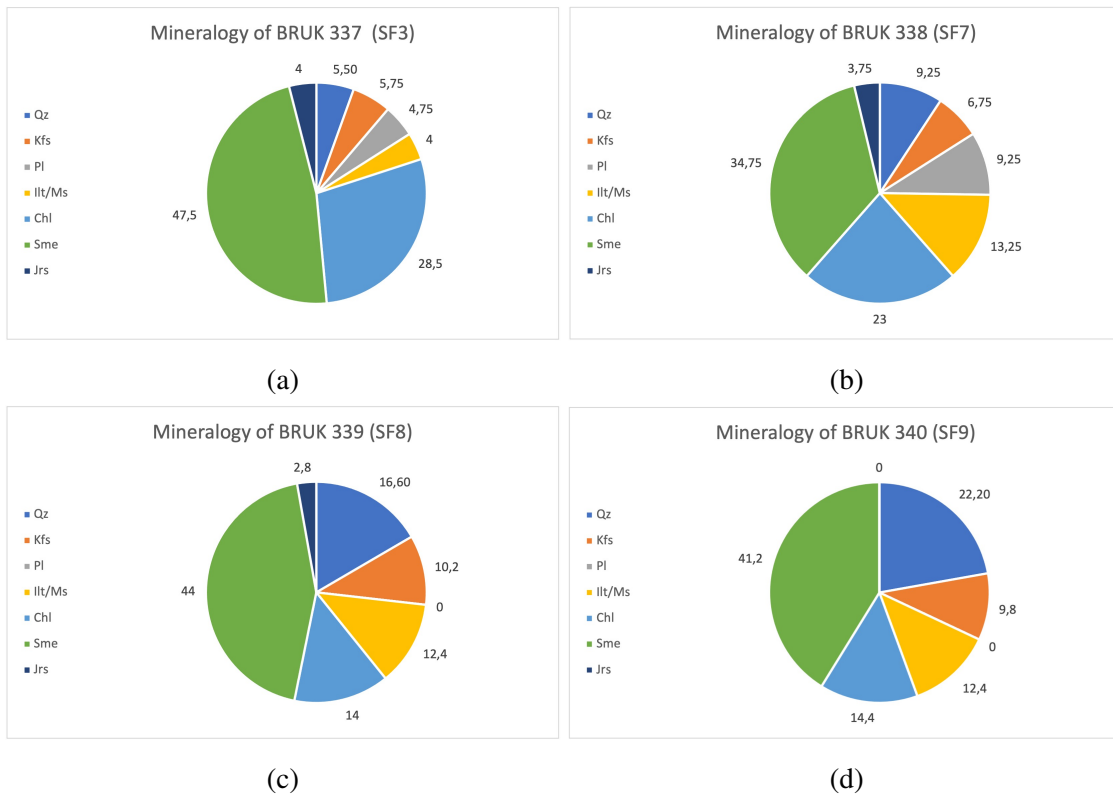
Figure 35: (a) Average mineralogy of BRUK 337 (SF3) (b) Average mineralogy of BRUK 338 (SF7) (c) Average mineralogy of BRUK 339 (SF8) d) Average mineralogy of BRUK 340 (SF9)
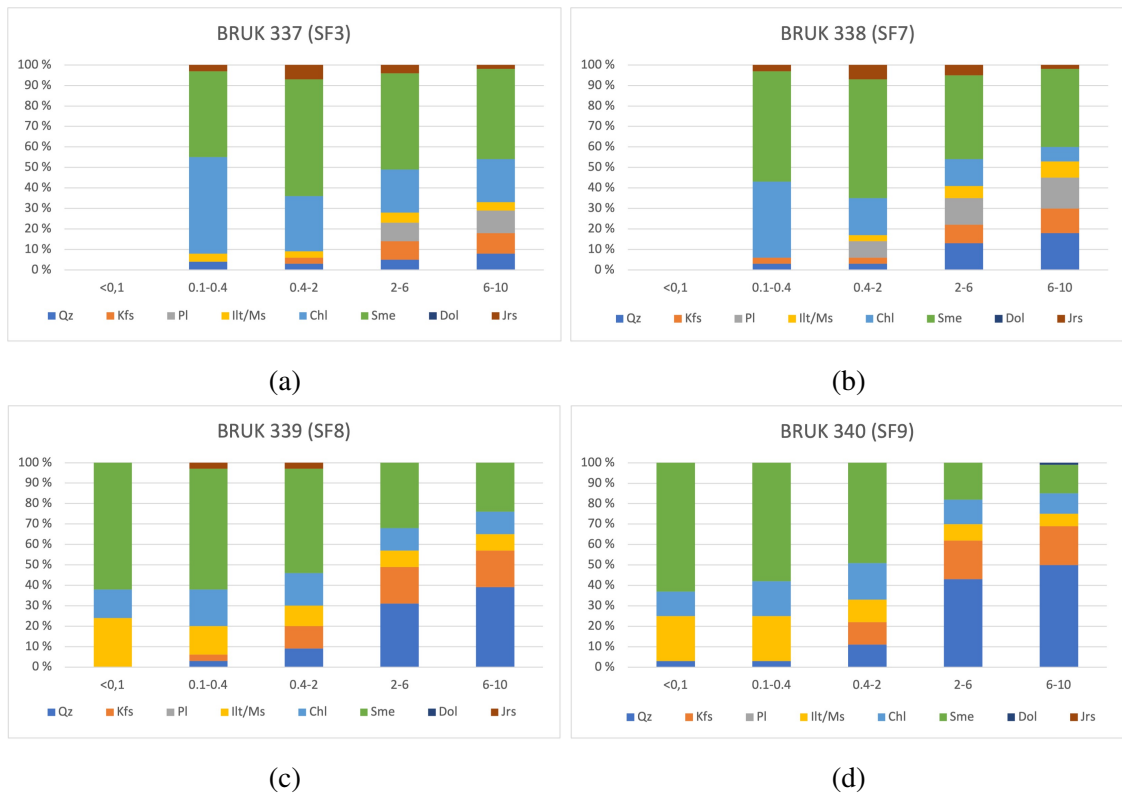
Figure 36: (a) Mineralogy per fraction of BRUK 337 (SF3) (b) Mineralogy per fraction of BRUK 338 (SF7) (c) Mineralogy per fraction of BRUK 339 (SF8) d) Mineralogy per fraction of BRUK 340 (SF9)

Sample ID	Size fraction [µm]	Qz	Kfs	Pl	Ilt/Ms	Chl	Sme	Jrs
BRUK 337	<0.1							
(SF3)	0.1 - 0.4	<5			<5	45-50	40-45	<5
	0.4 - 2	<5	<5		<5	25-30	>55	5-10
	2 - 6	5	9	9	5	21	47	4
	6 - 10	8	10	11	4	21	44	2
BRUK 338	<0.1							
(SF7)	0.1 - 0.4	<5	<5	Traces	35-40	>50	<5	
	0.4 - 2	<5	<5	5-10	<5	15-20	>50	5-10
	2 - 6	13	9	13	6	13	41	5
	6 - 10	18	12	15	8	7	38	2
BRUK 339	<0.1				20-25	10-15	>55	5-10
(SF8)	0.1 - 0.4	<5	<5		5-10	15-20	>50	<5
	0.4 - 2	9	11		10	16	51	3
	2 - 6	31	18		8	11	32	
	6 - 10	39	18		8	11	24	
BRUK 340	<0.1	<5			20-25	10-15	>60	
(SF9)	0.1 - 0.4	<5			10-15	15-20	>50	
	0.4 - 2	11	11		11	18	49	
	2 - 6	43	19		8	12	18	
	6 - 10	50	19		6	10	14	

Table 4: XRD-data from the four samples of fault gouge/fault breccia collected in the fault core. Mineral name abbreviations are using the GSWA standard.

5.8   Results from the K-Ar geochronology

K-Ar geochronology was preformed on samples BRUK 337, BRUK 338, BRUK 339 and BRUK 340, collected from SF3, SF7, SF8 and SF9, respectively (see fig. 19). These samples consist of fault gouge (SF8, SF9) and fine grained fault breccia (SF3, SF7). The results from the K-Ar geochronology is shown below in figure 37 and table 5. The age data from the K-Ar geochronology have a trend of decreasing ages with decreasing grain sizes, as shown in figure 37. The reason for this inclined trend and how these age data can be interpreted will be discussed later in the discussion chapter.
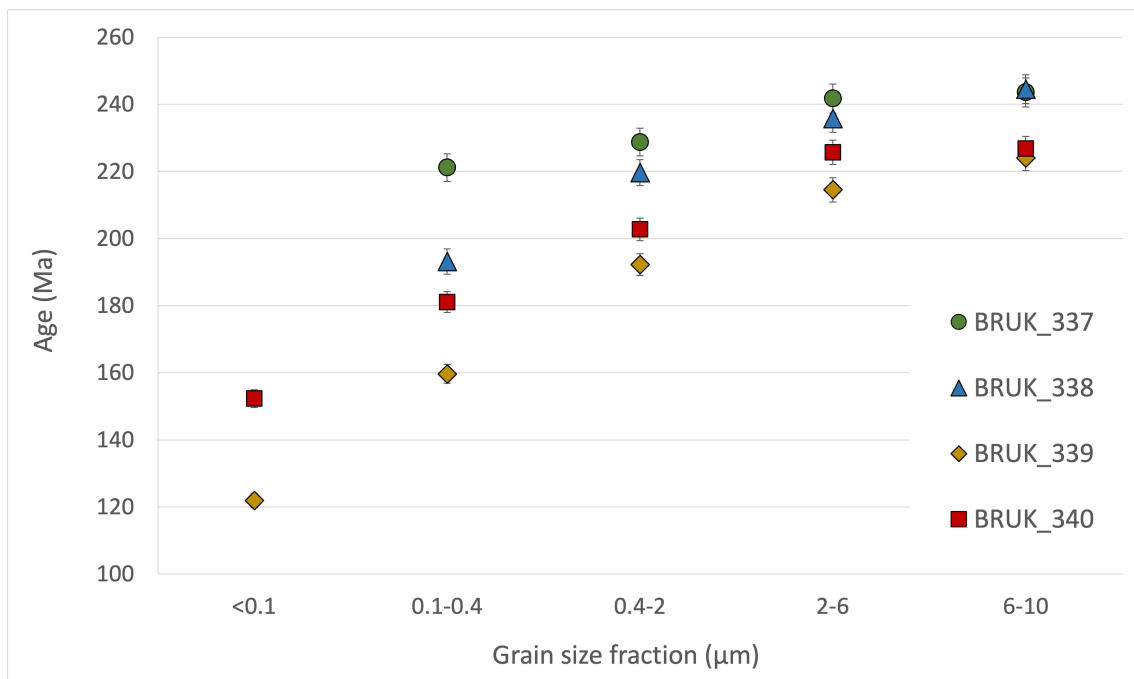
Figure 37: Data plot of the age data from the K-Ar geochronology.

Sample ID	Size fraction [μm]	K [%]	^{40}Ar [mol/g]	^{40}Ar [%]	Age [Ma]	σ [Ma]
BRUK 337 (SF3)	<0.1					
	0.1 - 0.4	0.56	2.304E-10	87.3	221.1	4.1
	0.4 - 2	0.88	3.701E-10	84.5	228.7	4.1
	2 - 6	1.16	5.183E-10	91.2	241.7	4.3
	6 - 10	1.38	6.253E-10	95.5	243.6	4.3
BRUK 338 (SF7)	<0.1					
	0.1 - 0.4	1.08	3.802E-10	90.4	193.2	3.8
	0.4 - 2	1.35	5.482E-10	90.7	219.7	3.9
	2 - 6	1.59	6.944E-10	94.5	235.8	4.1
	6 - 10	1.73	7.834	97.4	244.5	4.3
BRUK 339 (SF8)	<0.1	2.01	4.518E-10	67.8	121.9	2.2
	0.1 - 0.4	2.00	5.924E-10	78.6	159.6	2.8
	0.4 - 2	2.24	7.890E-10	87.0	192.2	3.3
	2 - 6	2.63	1.039E-09	93.6	214.5	3.6
	6 - 10	2.74	1.135E-09	95.6	224.0	3.8
BRUK 340 (SF9)	<0.1	2.05	5.648E-10	77.7	152.3	2.6
	0.1 - 0.4	2.26	7.451E-10	84.1	181.1	3.1
	0.4 - 2	2.81	1.046E-10	91.0	202.7	3.3
	2 - 6	3.29	1.371E-10	96.1	225.7	3.6
	6 - 10	3.21	1.343E-09	96.7	226.7	3.6

Table 5: Age data from K-Ar geochronology of fault gouge and fault breccia collected from the fault core of the PKFC.

6 Discussion

Present day exposure of faults only represents the end result of faulting, whereas faults often have a protracted and heterogeneous history with several phases of slip. During these different slip-phases, a number of different fault rocks will be produced as a result of comminution and in situ neocrystallization of the host rock. Dating of these fault rocks is therefore important to uncover the history of the fault, providing a date for the different faulting events. Furthermore, it is vital that the obtained K-Ar ages are interpreted correctly to provide an accurate conceptual model of the evolution of the fault. An approach for how to interpret K-Ar ages in relation to previous faulting history will therefore be described below, before a conceptual model of the evolution of the studied section of the PKFC will be presented.

6.1 Interpretations of the K-Ar dates

All dated samples from the PKFC show inclined trends within the "age vs. grain size" curves obtained from the K-Ar geochronology, where the finer grain sizes produce lower ages compared to the coarser grain sizes (see fig. 37). These inclined trends have also been observed within other K-Ar geochronological studies of fault-related rocks (Aldega et al., 2019; Bense et al., 2014; Davids et al., 2013; Pevear, 1999; Tartaglia et al., 2020; Torgersen et al., 2015; Torgersen et al., 2014). There have been concerns that this is caused by preferential loss of radiogenic ^{40}Ar due to particle size reduction. It has, however, been shown that an occurrence of proportionally more authigenic particles in progressively smaller size fractions is the cause of the inclined "age vs. grain size" curves, where the finest fractions consist of mostly authigenic particles (Clauer, 2013). In previous fault-dating studies, there have also been occurrences of different fractions containing a mixture of different authigenic particle generations, formed during different faulting events (Torgersen et al., 2015; Torgersen et al., 2014). Within these studies, no $2M_1$ detrial illite grains have been identified during XRD analysis and the inclined "age vs. grain size" curves is therefore explained by having different generations of faulting and illite growth, producing different $1M/1M_1$ illite generations. It is normal to interpret these ages such that the ages obtained from the finest fractions represent ages of different slip-phases, while a common age obtained from the coarsest fractions represent an earlier activation of the fault (Tartaglia et al., 2020; Torgersen et al., 2015; Torgersen et al., 2014). The intermediate fractions consist of a mixture of the two populations of authigenic particles and are therefore devoid of any geological significance.

There have been several suggested methods for interpreting the inclined K-Ar age-data. Pevear, 1999 has suggested that by quantifying the amount of detrial and diagenetic illite within each sample fraction, it is possible to use linear extrapolation to estimate the ages of the detrial and authigenic end-members. The amount of detrial and authigenic illite within each sample fraction is quantified using XRD-analysis, by identifying the $1M/1M_1$ authigenic particles and the $2M_1$ detrial particles. However, Torgersen et al., 2014 raised concerns that this method can produce inaccurate age results if either the temperature during faulting was sufficiently high, so that authigenic illite/muscovite became detrial $2M_1$ or if the protolith contain $1M/1M_1$ diagenetic illite/muscovite, like illite in shale. The method suggested by Pevear, 1999 also requires the use of the program WILDFIRE to estimate the portions of authigenic and detrial illite within the different fractions, which we don't have access to. This method will therefore not be used to constrain the ages of the different faulting events within this study.

Instead this study will adopt the age attractor model (Torgersen et al., 2014), such that the finest fractions are considered mainly composed of authigenic, synkinematic minerals, constraining the last faulting increment. However, even the finest grain size fractions may still include some inherited protolithic minerals (Haines and van der Pluijm, 2008) or different generations of authigenic phases reworked during multiple stages of deformation. Ages obtained from the finest grain size fractions should thus still be considered as maximum ages of faulting, although they provide the best available constraint on the timing of the most recent faulting events (Tartaglia et al., 2020).

The maximum temperature of the samples must be determined to model thermally activated volume diffusion of argon, which can cause artificially age loss. As mentioned within subchapter 5.6, calcite veins were found in both END 4, END 5 and END 6 (see fig. 31). Twinning of the e-plane in the calcite was found, were thin twins are slightly dominating, but with a significant portion of thick twins (see fig. 33). Thin twins dominate below 170 °C and thick twins dominate above 200 °C (Ferrill et al., 2004), which infers that the calcite, combining both thin and thick twins, has experienced a maximum temperature between 170 and 200 °C. Torgersen et al., 2014 has modelled argon diffusion, where the age loss do to thermally activated volume diffusion at different temperatures were modelled for different grain size fractions. This model suggests that during heating-cooling pulses of 5 and 10 Ma to temperatures of 230–240 °C, even very fine-grained illites (<0.1 μm) do not experience more than a 10% resetting of their initial K–Ar age. Very fine-grained illites (<0.1 μm) experience approximately no resetting of their initial K–Ar age at temperatures below 200°C (Torgersen et al., 2014). Thermally induced volume diffusion effects, which could result in resetting of the initial K–Ar age, specially within the finer grain size fraction, are therefore not considered in our conceptual model of the

evolution of the studied section of the PKFC.

6.2   Fault evolution

This subchapter will present a conceptual model of the pre-historic evolution of the studied section of the PKFC, as shown if figure 38. Several indicators suggest that an early phase of slip has occurred prior to the dated Mesozoic faulting events. For example, both END 10 and 11 consist of cataclasite, which is a fault rock formed by a combination of brittle and ductile deformational mechanisms, as explained within subchapter 3.3. Cataclasticly deformed rocks are also found in the coarse grained clasts of the SF0, SF2 and SF4 fault breccias. In addition, several areas of quartz aggregates within the thin sections appear to have experienced ductile deformation and an example of ductile deformed quartz is shown in figure 34b. Ductile deformation occurs at higher temperatures than brittle deformation, where the brittle-ductile transition of quartz occurs at a temperature of 300 °C (Masuda et al., 2019; C. H. Scholz, 1998). This infers that an earlier period of slip has occurred along the studied section of the PKFC, where the host rock has been subjected to higher temperatures compared to the later brittle Mesozoic phases of slip. The cataclasite located in the hanging wall has not been dated during this study and the timing of this early slip-phase is therefore unknown. The slip-phase must, however, have occurred later than the Herefoss granite formation age and earlier than the later brittle Mesozoic phases of slip, providing an age between c. 900 Ma and 230 Ma.

The resulting ages from the K-Ar geochronology have been studied together with kinematic indicators and the anatomy of the fault. They show that the studied section of the PKFC has experienced significant displacement through several phases of slip in the Mesozoic era, lasting from middle Triassic to early Cretaceous. This information has been used to deduce an interpretation of the Mesozoic slip-phase evolution of the studied PKFC section. The common geochronological age (c. 244 Ma) of the coarsest fractions of BRUK 337 (SF3) and 338 (SF7) can either be interpreted as a common early faulting event or as the closure age of the K-feldspars within the Herefoss granite. The closure age marks the time when the K-feldspars have cooled down sufficiently and reached their closure temperature, such that argon retention can begin. The closure temperature of K-feldspar is around 210 °C for 1-μm grains, and 260 °C for 10-μm grains cooling at 10 °C/Ma (Kelley, 2002a). To determine if this obtained age is the closure age of the K-feldspars, a sample of undeformed Herefoss granite should thus be dated by utilizing K-Ar or Ar-Ar geochronology. Obtaining matching ages for the K-feldspars and the coarsest fractions of BRUK 337 and 338 will then confirm this as a closure age. Dating of K-feldspars from an undeformed sample of Herefoss granite has not been preformed dur-

ing this study, but is recommended to do for further work. Within this conceptual model of the evolution of the studied PKFC section, this age has tentatively been interpreted as the closure age of the K-feldspars within the Herefoss granite, as shown in figure 38B.

The common geochronological age (c. 227 Ma - 224 Ma) of the coarsest fractions from BRUK 339 (SF8) and 340 (SF9) is interpreted to represent a common early faulting event within the studied section of the PKFC. This is because only the geochronological age of the coarsest fractions from BRUK 337 (SF3) and 338 (SF7) (c. 244 Ma) can be interpreted as a closure age, as it is highly unlikely for K-feldpars from nearby samples to have two different cooling ages. Also, the fact that the samples have overlapping ages for the coarsest fractions, while the ages of the finest fractions are diverging indicate that the common geochronological age of c. 227 Ma - 224 Ma represent a common early faulting event. This early slip-phase is shown in figure 38C. The ages obtained from the finer fractions represents later separate faulting events. It is probable that this common early faulting event produced a wider zone of deformation, resulting in a light grey, coarse grained fault breccia similar to SF0, SF2 and SF4 (see fig. 19). Strain has then later been localised within narrower zones of deformation, producing tabular facies of finer fault breccias and fault gouge.

The next stage of faulting formed a dark, fine grained fault breccia (BRUK 337/SF3), which has a maximum formation age of c. 221 Ma. No <0.1 μm fraction was obtained from this fault breccia, as there was not sufficient fine material. The finest dated fraction is therefore 0.1 - 0.4 μm, as shown in table 5. This fraction consists of a mixture of authigenic and detrital particles and therefore only provide a maximum age of faulting. The formation of BRUK 337 can be interpreted as a result of continued faulting, after a wider zone of coarse grained fault breccia was formed at 227 - 224 Ma. Continued deformation was then concentrated in a narrower tabular zone of dark, fine grained fault breccia (BRUK 337/SF3). The next stage of faulting formed a dark red, fine grained fault breccia (BRUK 338/SF7), formed at <193 Ma. No <0.1 μm fraction was obtained from this fault breccia either and the obtained K-Ar age therefore only provide a maximum age of faulting. However, the trends of the data-plots presented in figure 37 indicates that BRUK 338 (SF7) was formed approximately simultaneously with BRUK 340 (SF9), which has an obtained age of c.152 Ma from the <0.1 μm fraction (see table 5). The next stage of faulting formed a dark green/blue fault gouge (BRUK 340/SF9) at c. 152 Ma, followed by a later phase of slip, forming a red/orange fault gouge (BRUK 339/SF8) at c. 122 Ma, as shown in figure 38.

Subhorizontally oriented striations were measured at the cataclasite located in the hanging wall, within SF10 and SF11 (see fig. 19), while subvertically oriented striations were measured within the fault gauge at the SF8/SF9 contact. This infers a strike-slip oriented

slip movement during the earlier cataclasite forming slip-phase and a dip-slip oriented slip movement during the later Mesozoic phases of slip. This is further proven by internal cross-cutting relationships between the two populations of striations, were subvertically oriented striations in the fault gouge are observed cross-cutting subhorizontally oriented striations in the cataclasite. This implies that the dip-slip oriented movement occurred after the strike-slip oriented movement.

To conclude the order of slip-phases for the studied section of the PKFC, an early cataclasite forming slip-phase with strike-slip oriented slip movement occurred between c. 900 Ma and 230 Ma. Later, a common brittle faulting event produced a wider zone of deformation, which resulted in the formation of a light grey, coarse grained fault breccia at c. 227 - 224 Ma. Afterwards the deformation was concentrated in a narrower tabular zone of dark, fine grained fault breccia (BRUK 337/SF3), formed at <221 Ma. This was followed by the formation of a dark red, fine grained fault breccia (BRUK 338/SF7), a dark green/blue fault gouge (BRUK 340/SF9) and a red/orange fault gouge (BRUK 339/SF8), formed at <193 Ma, 152 Ma and 122 Ma, respectively. The brittle Mesozoic slip-phases, occurring from c. 227 Ma to 122 Ma, had normal dip-slip oriented slip movements that are associated with E-W oriented Mesozoic rifting, as explained within subchapter 6.3.
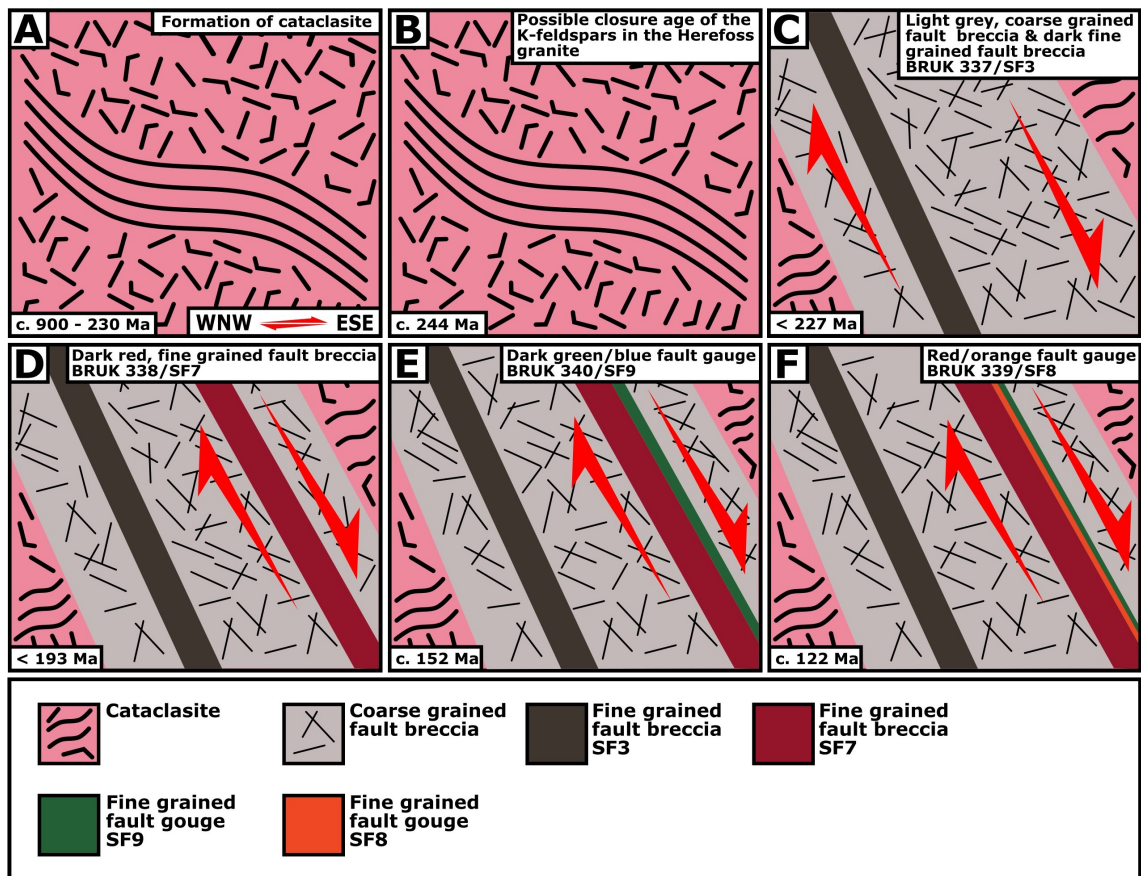
Figure 38: Conceptual model of the prehistoric slip-phase evolution of the studied section of the PKFC. The model is oriented WNW - ENE, perpendicular to the fault core. a) Early activation (c. 900 - 230 Ma) of the studied section of the PKFC, producing cataclasite. b) Possible closure age (c. 244 Ma) of the K-feldspars in the Herefoss granite. c) Formation of a wider zone of light grey, coarse grained fault breccia at c. 227 Ma - 224 Ma, with a normal dip-slip oriented slip movement. Later the deformation was concentrated in a narrower tabular zone, forming BRUK 337 (SF3) at <221 Ma, with continued normal dip-slip oriented slip movement. d) BRUK 338 (SF7) was formed at <193 Ma, with a normal dip-slip oriented slip movement. e) BRUK 340 (SF9) was formed at c. 152 Ma, with a normal dip-slip oriented slip movement. f) BRUK 339 (SF8) was formed at c. 122 Ma, with a normal dip-slip oriented slip movement.

6.3 The evolution of the studied section of the PKFC in relation to Paleozoic and Mesozoic rifting events

This subchapter will compare the different phases of slip along the studied section of the PKFC with various paleotectonic stress orientations during different prehistoric rifting events. The strike-slip oriented movement during the early cataclasite forming slip-phase has tentatively been interpreted to correlate with NNW-SSE oriented extensional tectonic stress associated with Neoproterozoic post-Sveconorwegian rifting and orogenic collapse (Bingen et al., 2008; Bingen et al., 2020). This correlates with the reactivation of the WSW-ENE oriented Kristiansand-Porsgrunn Shear Zone (KPSZ) at 891.2 ± 2.9 Ma to 880.2 ± 2.8 Ma as a top-to-the-SSE extensional structure (Mulch et al., 2005; Mulch and Cosca, 2004). This slip-phase along the KPSZ indicates NNW-SSE orientated extensional tectonic stress and is post-dating the formation age of the Herefoss granite. The age of initiation for the Listafjord– Drangedal Fault Complex, which is a SW-NE oriented structure, is suggested to be Late Proterozoic with a dextral sense of shear (R. H. Gabrielsen et al., 2019). This also correlates with the NNW-SSE oriented extensional tectonic stress during post-Sveconorwegian rifting and orogenic collapse. It is also noteworthy that both of the described shear zones have experienced later reactivations, were brittle extensional-related top-to-the-SE structures overprint older facies of mylonite and cataclasite. This is simular to the evolution of the studied section of the PFKC. It is therefore tentatively interpreted that the SSW-NNE oriented southern PKFC section was activated as a shear zone with a dextral strike-slip oriented slip-movement during Neoproterozoic post-Sweconorwegian rifting. Later it experienced several reactivations during E-W oriented extensional tectonic stress throughout the Mesozoic era. It is, however, recommended for further work that Ar-Ar dating of the cataclasite in the hanging wall is performed, which can provide a date for this early cataclasite forming phase of slip.

Several earlier studies conducted on the northern North Sea (Badley et al., 1988; Færseth, 1996; Odinsen et al., 2000; Ziegler, 1992) suggest that two main stages of rifting postdated the formation of the Caledonian orogen: an earlier stage of Permo-Triassic rifting and a later stage of Mid-Late Jurassic rifting. The tectonic extensional stress had an approximately E(NE)-W(SW) orientation during the first Permo-Triassic rifting stage and an approximately E(SE)-W(NW) orientation during the second Mid-Late Jurassic rifting stage (R. Gabrielsen et al., 1999; Ksienzyk et al., 2016; Scheiber and Viola, 2018). The formation age of BRUK 340 (SF9) (c. 152 Ma), dated to the Late Jurassic Period, coinsides with the second Mid-Late Jurassic rifting stage of the northern North Sea. The studied section of the PKFC was then reactivated, with a normal dip-slip oriented movement. The trend of the curves presented in figure 37 indicates that the formation age of BRUK 338 (SF7) is approximately similar to that of BRUK 340, as mentioned within

subchapter 6.2. Therefore, the formation age of BRUK 338 plausibly coincides with the second rifting stage of the northern North Sea. Extrapolation of the "age vs grain size" curve of BRUK 337 (SF3), presented in figure 37, suggests a formation age of approximately 221 - 190 Ma. This falls in between the two rifting stages, a period which has generally been associated with tectonic quiescence. However, dike-intrusions located in the southwestern Norway, dated by K–Ar and Ar–Ar analyses at 230–210 Ma, have opening modes suggesting that they intruded during continued E–W extension (Ksienzyk et al., 2016; Scheiber and Viola, 2018). Additionally, N–S-striking faults in southern Norway with approximately dip-slip oriented mineral striations show significant fault activity in the Late Triassic (210 – 200 Ma; Torgersen et al., 2015). This indicate that E-W oriented extensional tectonic stress still existed during the Late Triassic in southern Norway. The common faulting event occurring at c. 227-224 Ma, presented in figure 38C, also falls in between the first and the second rifting stage of the northern North Sea and was possibly reactivated by the same Late Triassic, E-W oriented extensional tectonic stress. The last reactivation of the studied PKFC section and formation of BRUK 339 (SF8) occurred at c. 122 Ma, in the Early Cretaceous. This slip-phase post-dates the second Mid-Late Jurassic northern North Sea rifting stage. However, dated faults oriented NNE-SSW indicate a WNW-ESE oriented extensional regime during the Early Cretaceous Period (Ksienzyk et al., 2016). Additionally, Bell et al., 2014 describes an eastward migration of fault reactivation during the second North Sea rifting stage, with the faults closest to the Viking Graben being reactivated first and those farther away from the rift axis reactivated later. It is thus possible that fault reactivation only reached onshore Norway during the Early-Mid Cretaceous. Ziegler, 1992 also found that crustal extension in the North Sea rift was concentrated on the Viking Graben during the Late Jurassic to Early Cretaceous, with a peak in rifting activity at the transition from the Jurassic to the Cretaceous Period. It is therefore a reasonable assumption that approximately E-W to NW-SE oriented extensional tectonic stress still prevailed during the Early-Mid Cretaceous, causing normal dip-slip oriented reactivation of the studied PKFC section at c. 122 Ma.
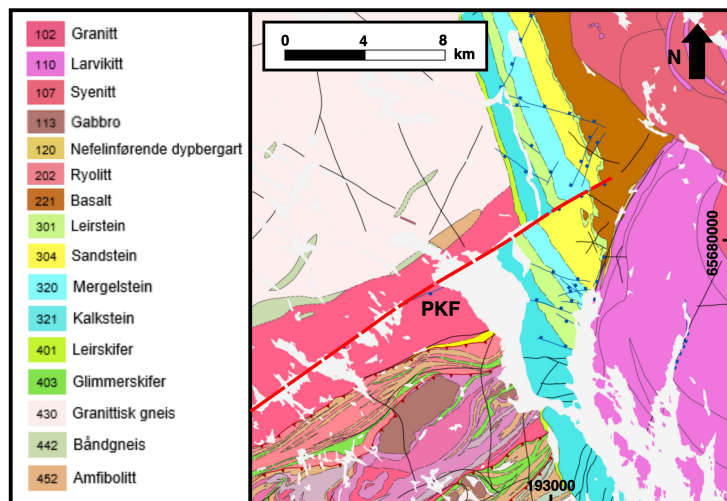
Subvertically oriented striations were measured within the fault gauge at the SF8/SF9 contact, as mentioned within subchapter 5.2 and 6.2. This infers that normal dip-slip oriented slip movements occurred during the later Mesozoic phases of slip, as a result of the prevailing E-W oriented extensional regime. The slip movements of the different slip-phases are shown in figure 38.

6.4 PKFC - A fault complex comprised of two major segments

A combination of automatic lineament analysis and comparison between resulting K-Ar ages with ages obtained from cross-cutting relationships in the Porsgrunn area suggest that the PKFC consists of two segments; one northern segment, located south of Porsgrunn and one southern segment, located north of Kristiansand. Indications of this dual segmentation will be discussed below, while also attempting to locate the extents and orientations of these segments, using analysis of automatic lineaments.

6.4.1 K-Ar geochronology age data and cross-cutting relationships in the Porsgrunn area

The age data from the K-Ar geochronology shows that the southern PKFC segment has experienced significant displacement through several phases of slip in the Mesozoic era, lasting from Middle Triassic to Early Cretaceous (see table 5 and fig. 37). As mentioned in subchapter 2.2, the northern PKFC segment cuts through the long and narrow (50 km x 2.5 km) belt of Cambro-Silurian sedimentary rocks, while the Skien basalts remain unaffected. This is

Figure 39: Map of the regional geology of the Skien and Porsgrunn area, with legend shown to the left. The map sheet is downloaded from NGU.no and the coordinates are in UTM zone 33.

also shown in figure 39. By determining the ages of the Skien basalts and the youngest strata of the Cambro-Silurian sedimentary rocks, cross cutting relationships can be used to estimate an approximate age-interval of when the last slip-phase has occurred along the northern PKFC segment.

The Skien basalts, located in the Skien and Porsgrunn area, were dated by Corfu and Dahlgren, 2008. They dated melilitic tuff containing perovskite, located in the lower parts of the basalts. U-Pb geochronology were used and they obtained an age of 298.9 ± 0.7 Ma for the melilitic tuff. That gives an age of formation between the Asselian

geochronological age, early Permian Period and the Gzhelian geochronological age, late Carboniferous Period.

The Holmestrand Formation makes up the top-layer in the Cambro-Silurian sedimentary rocks in Skien and Porsgrunn and is also the youngest formation in the Ringerike group (Davies et al., 2005). The age of the Ringerike Group and the Holmestrand Formation is somewhat contentious as the possibility of discovering reliable material for dating is limited and a wide variety of ages using different dating methods have been published. However, several previous studies have suggested an age of formation extending from Wenlock to Ludlow, in the Mid-Late Silurian Period (Gudveig Baarli et al., 1999; Plotnick, 1999; Turner, 1999; Worsley et al., 1983). Davies et al., 2005 found that the Holmestrand Formation at Jeløya is Pridoli in age, but also stated that the Ringerike Group is diachronous, being younger to the south, reflecting the fact that its siliciclastic depositional systems were advancing southwards from the Caledonides. It is therefore difficult to compare ages within the same Formation at different outcrops.

By using crosscutting relationships with the attained ages above, an approximate age-interval of the last slip-phase for the northern PKFC segment is given. Slip along the northern segment occurred before the Asselian age, early Permian Period and after the Wenlock/Ludlow age, Mid-Late Silurian Period. Age data from K-Ar geochronology in the southern PKFC segment indicate that several phases of displacement occurred in the Mesozoic era, lasting from middle Triassic to early Cretaceous. In addition, several indicators suggest that an earlier Neoproterozoic cataclasite-forming slip-phase has occurred along the southern PKFC segment. However, as displacement during the Mesozoic era only appears to have occurred along the southern PKFC segment, it is reasonable to assume that the PKFC consists of a northern and a southern segment, which are operating independently of each other.

6.4.2 Extents and orientations of the northern and southern segments of the PKFC

Data collected with OTTO, a digital lineament-mapping software produced by NGU, were used to interpret the extent of the northern and southern PKFC segments. The northern and southern segments are shown in figure 40 and are c. 24 km and 70 km long, respectively. The UTM coordinates of the northern segment spans from 6568139N/194222E in the northeastern end to 6550296N/163544E in the southwestern end. The coordinates of the southern segment span from 6471360N/93588E in the northeastern end to 6515067N/118330E in the southwestern end (UTM zone 33). The extent of these segments are however only an estimate, as the lengths and orientations are based on an interpretation of digital lineaments, which are shown in figure 40B and 40D.

Figure 40: A) Red stipled line indicating the extent and orientation of the northern PKFC segment, with a background map for orientation. B) Otto lineaments from the northern segment area, south of Porgrunn/Skien, used to interpret the extent and orientation of the northern PKFC segment. Red dots indicate the extent and orientation of the northern PKFC segment. C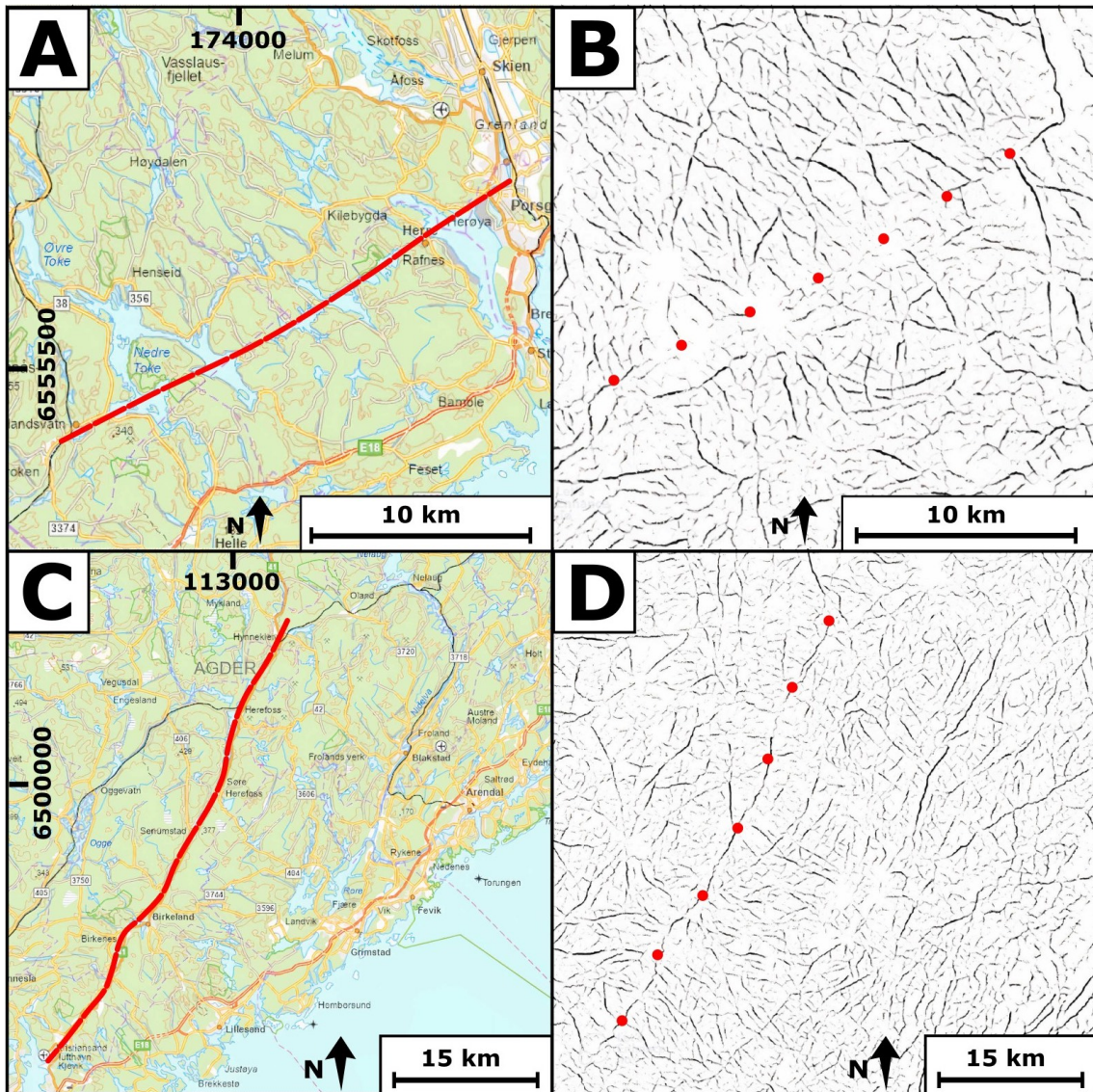) Red stipled line indicating the extent and orientation of the southern PKFC segment, with a background map for orientation. D) Otto lineaments from the southern segment area, north of Kristiansand, used to interpret the extent and orientation of the southern PKFC segment. Red dots indicate the extent and orientation of the southern PKFC segment. Coordinates in UTM zone 33.

6.5   Fracture orientations throughout the fault zone

The fracture frequencies and orientations were mapped with scanlines at varying distances to the SF9/SF10 contact (see fig. 19), in addition to mapping fracture orientations by fracture digitization, using a 3D model. These fracture orientations are shown in the result section in figure 23, 25 and 26. The digitized fractures from the 3D model show a dominant trend subparallel to the fault core of the PKFC, where a much smaller amount of fractures are oriented subperpendicular to the fault core. This is shown in figure 26 and 27. This concurs with the existing literature, were Braathen and Gabrielsen, 1998; Braathen and Gabrielsen, 2000; R. H. Gabrielsen and Braathen, 2014 state that the typical dominant fracture trend within the fault core (Zone A and B) is parallel to the fracture lineament. It is also noteworthy that the majority of the joints, non-striated shear fractures and striated shear fractures presented in figure 21 are oriented subparallel with the fault core of the PFCK. Scanlines 1 and 2, in addition to the measured fault lense, recorded the fracture density and orientations within the fault core. They show a general trend of fractures that are subperpendicular to the fault plane, as shown in figure 25. This trend continues farther away from the fault core, within the fractures measured at scanline 3 and 4, which have an angle between 60° and 90° degrees from the fracture lineament. This is opposite to the general consensus that the main trend of fractures both within and in proximity of the fault core typically is oriented subparallel with the fracture lineament. There are some interpretations that can explain why these results have occurred. One explanation is that the orientation of the longest scanlines were oriented parallel with the fault core, with a north-northeast - south-southwest orientation (x-orientation, see fig. 22). This scanline-orientation was chosen because of the steep morphology of the outcrop, which made measurements of longer scanlines perpendicular to the fault core both dangerous and infeasible. Fractures must intersect the scanline to be recorded, which causes fault parallel scanlines to not record fractures that are parallel with the fracture lineament. Another explanation is that the scanlines don't record the scale of the fracture surface. The fractures oriented subparallel with the fracture lineament generally have a larger fracture surface compared to the subperpendicular fractures, but are still only recorded as one fracture on the scanline.

6.6   Variability of mineralogy across the fault zone

The different mineralogical compositions of the collected samples (see fig. 30), located at different distances from the fault core (see fig. 31) were described within subchapter 5.6. A gradual increase of chloritization of biotite is recorded at decreasing distances to the fault core. This is caused by either hydrothermal processes or meta-somatic pro-

cesses, as explained within subchapter 3.9. As shown in figure 23, the fracture frequency is increasing towards the fault core, which produce higher permeability. The increasing permeability results in an increased flow of hydrothermal fluids, producing an increased amount of hydrothermal alteration. The increasing chloritization of biotite at decreasing distances to the fault core is therefore interpreted as related to increasing fracture frequencies in proximity of the fault. There is no chloritized biotite in END 3 and END 4, located in the hanging wall. One explanation may be the very fine grain sizes of these samples, where the minerals have been crushed down to very fine grained mineral-aggregates. A significant portion of matrix is also found within END 3. These fine grained mineral aggregates and matrix prevent any significant fractures from opening, and are therefore significantly reducing the permeability in the hanging wall. As a result, less hydrothermal alteration occurs, producing less chloritization of biotite. It is also possible that hydrothermal alteration has occurred earlier and that the chloritized biotite has been chrushed as a result of later comminution.

It has been recorded an increasing amount of carbonates at decreasing distances to the fault core. This is natural as carbonate veins commonly are distributed in fault zones as the product of fault-fluid activities (Li et al., 2020). On the other hand, sericitic overgrowth of feldspars are distributed evenly across the fault zone with slightly more overgrowth in END 1 and 12, that consist of undeformed Herefoss granite located farther away from the fault core. This is opposite of what is to be expected, as the highest amount of sericitic alteration should occur in areas with higher fracture frequencies and subsequent permeability (see subchapter 3.8). One possible explanation is that the sericitic alteration predates the faulting that created the observed fault core, and represents an earlier low-grade event in the Herefoss Granite. A combination of deformation, grain size reduction and recrystallization of feldspars have then later reduced the quantity of sericitic overgrowth within the fault core.

7 Conclusions

This master thesis has utilized structural mapping and analysis, XRD mineralogy and K-Ar fault gouge geochronology to unravel the structural and temporal evolution of the studied section of the PKFC. Simultaneously has mapping of the structural architecture of the fault zone been provided. The study concludes with these findings:

- The fault zone consists of a fault core bounded by damage zones, with the hanging wall and footwall damage zones having a thickness of 370 - 510 m and 60 - 280 m, respectively. The fault core is a 2.5 - 5 m thick composite brittle structure with a high frequency of fractures (>40 f/m^3), and is comprised of 12 juxtaposed, but not coeval brittle structural facies.

- Mineralogical analysis, utilizing a petrographic optical microscope and thin sections, has uncovered increased amounts of chloritic alteration of biotite and precipitation of carbonate veins within the fault core. This is a result of increased fracture frequencies and subsequent increase in permeability, producing an increased flow of hydrothermal fluids.

- An earlier cataclasite forming phase of slip has been uncovered along the studied section of the PKFC, which has tentatively been linked to the Neoproterozoic post-Sveconorwegian extensional regime and orogenic collapse. Subhorisontally oriented striations coupled with post-Sveconorwegian extensional tectonic stress have tentativly inferred a dextral strike-slip oriented slip movement during this phase of slip.

- Age data from the K-Ar geochronology shows that the studied section of the PKFC has experienced significant displacement through several phases of slip in the Mesozoic era, lasting from middle Triassic to early Cretaceous. These phases of slip have been linked to Mesozoic rifting, with an approximately E-W oriented extensional tectonic stress producing reactivations of the fault. Subvertically oriented striations coupled with Mesozoic rifting events indicate a normal dip-slip oriented slip movement for these phases of slip.

- A combination of automatic lineament analysis and comparison between resulting K-Ar ages with ages obtained from cross-cutting relationships in the Porsgrunn area suggest that the PKFC consists of two segments; one northern segment, located south of Porsgrunn and one southern segment, located north of Kristiansand. The northern and southern segments are c. 24 km and c. 70 km long, respectively, and both have an approximately NE-SW orientation.

References

Aldega, L., Viola, G., Casas-Sainz, A., Marcén, M., Román-Berdiel, T., & van der Lelij, R. (2019). Unraveling multiple thermotectonic events accommodated by crustal-scale faults in northern iberia, spain: Insights from k-ar dating of clay gouges. *Tectonics*, *38*(10), 3629–3651.

Badley, M., Price, J., Rambech Dahl, C., & Agdestein, T. (1988). The structural evolution of the northern viking graben and its bearing upon extensional modes of basin formation. *Journal of the Geological Society*, *145*(3), 455–472.

Barth, T. (n.d.). Fw,(1956) studies in granites and gneisses. *Skrift. Norsk. Vidensk-Ak. Oslo. I Mat-Naturv. Kl*, (1), 1–35.

Barth, T. F. (1947). The nickeliferous iveland-evje amphibolite and its relation.

Bell, R. E., Jackson, C. A.-L., Whipp, P. S., & Clements, B. (2014). Strain migration during multiphase extension: Observations from the northern north sea. *Tectonics*, *33*(10), 1936–1963.

Bense, F. A., Wemmer, K., Löbens, S., & Siegesmund, S. (2014). Fault gouge analyses: K–ar illite dating, clay mineralogy and tectonic significance—a study from the sierras pampeanas, argentina. *International Journal of Earth Sciences*, *103*, 189–218.

Bingen, B., Nordgulen, O., Viola, G., et al. (2008). A four-phase model for the sveconorwegian orogeny, sw scandinavia. *Norsk geologisk tidsskrift*, *88*(1), 43.

Bingen, B., Viola, G., Möller, C., Vander Auwera, J., Laurent, A., & Yi, K. (2020). The sveconorwegian orogeny. *Gondwana Research*, *90*, 273–313.

Boone, G. M. (1969). Origin of clouded red feldspars; petrologic contrasts in a granitic porphyry intrusion. *American Journal of Science*, *267*(6), 633–668.

Braathen, A., & Gabrielsen, R. (1998). Lineament architecture and fracure distribution in metamorphic and sedimentary rocks, with applications to norway.

Braathen, A., & Gabrielsen, R. H. (2000). Bruddsoner i fjell: Oppbygning og definisjoner. *7*.

Braathen, A., Osmundsen, P. T., & Gabrielsen, R. H. (2004). Dynamic development of fault rocks in a crustal-scale detachment: An example from western norway. *Tectonics*, *23*(4).

Bugge, A. (1928). En forkastning i det syd-norske grunnfjell: Norges geol. *Undersökelse no*, *130*.

Bureau of Reclamation. (1991). Engineering geology field manual.

Caine, J. S., Evans, J. P., & Forster, C. B. (1996). Fault zone architecture and permeability structure. *Geology*, *24*(11), 1025–1028.

Clark, C. D., & Wilson, C. (1994). Spatial analysis of lineaments. *Computers & Geosciences*, *20*(7-8), 1237–1258.

Clauer, N. (2013). The k-ar and 40ar/39ar methods revisited for dating fine-grained k-bearing clay minerals. *Chemical Geology*, *354*, 163–185.

Corfu, F., & Dahlgren, S. (2008). Perovskite u–pb ages and the pb isotopic composition of alkaline volcanism initiating the permo-carboniferous oslo rift. *Earth and Planetary Science Letters*, *265*(1-2), 256–269.

Cowie, P. A., & Scholz, C. H. (1992). Displacement-length scaling relationship for faults: Data synthesis and discussion. *Journal of Structural Geology*, *14*(10), 1149–1156.

Davids, C., Wemmer, K., Zwingmann, H., Kohlmann, F., Jacobs, J., & Bergh, S. G. (2013). K–ar illite and apatite fission track constraints on brittle faulting and the evolution of the northern norwegian passive margin. *Tectonophysics*, *608*, 196–211.

Davies, N. S., Turner, P., & Sansom, I. J. (2005). A revised stratigraphy for the ringerike group (upper silurian, oslo region). *Norwegian Journal of Geology/Norsk Geologisk Forening*, *85*(3).

Elders, W. (1963). On the form and mode of emplacement of the herefoss granite.

Evans, J. P. (1988). Deformation mechanisms in granitic rocks at shallow crustal levels. *Journal of Structural Geology*, *10*(5), 437–443.

Evans, J. P., Forster, C. B., & Goddard, J. V. (1997). Permeability of fault-related rocks, and implications for hydraulic structure of fault zones. *Journal of structural Geology*, *19*(11), 1393–1404.

Færseth, R. (1996). Interaction of permo-triassic and jurassic extensional fault-blocks during the development of the northern north sea. *Journal of the Geological Society*, *153*(6), 931–944.

Faulkner, D., Jackson, C., Lunn, R., Schlische, R., Shipton, Z., Wibberley, C., & Withjack, M. (2010). A review of recent developments concerning the structure, mechanics and fluid flow properties of fault zones. *Journal of Structural Geology*, *32*(11), 1557–1575.

Ferrill, D. A., Morris, A. P., Evans, M. A., Burkhard, M., Groshong Jr, R. H., & Onasch, C. M. (2004). Calcite twin morphology: A low-temperature deformation geothermometer. *Journal of structural Geology*, *26*(8), 1521–1529.

Gabrielsen, R., Odinsen, T., & Grunnaleite, I. (1999). Structuring of the northern viking graben and the møre basin; the influence of basement structural grain, and the particular role of the møre-trøndelag fault complex. *Marine and Petroleum Geology*, *16*(5), 443–465.

Gabrielsen, R. H., & Braathen, A. (2014). Models of fracture lineaments—joint swarms, fracture corridors and faults in crystalline rocks, and their genetic relations. *Tectonophysics*, *628*, 26–44.

Gabrielsen, R. H., Braathen, A., Kjemperud, M., & Valdresbråten, M. L. R. (2017). The geometry and dimensions of fault-core lenses. *Geological Society, London, Special Publications*, *439*(1), 249–269.

Gabrielsen, R. H., & Clausen, J. A. (2001). Horses and duplexes in extensional regimes: A scale-modeling contribution. *Geological Society of America Memoirs*, *193*, 207–220.

Gabrielsen, R. H., Olesen, O., Braathen, A., Faleide, J. I., Baranwal, V. C., & Lindholm, C. (2019). The listafjorden–drangedal fault complex of the agder–telemark lineament zone, southern norway. a structural analysis based on remote sensing and potential field data. *GFF*, *141*(3), 200–215.

Gudveig Baarli, B., Keilen, H. B., & Johnson, M. E. (1999). Silurian communities of the oslo region, norway. *WORLD AND REGIONAL GEOLOGY*, 327–349.

Gunleiksrud, I. (2017). Multiscalar lineament study of the drangedal and nome area using topographic and magnetic data.

Haines, S. H., & van der Pluijm, B. A. (2008). Clay quantification and ar–ar dating of synthetic and natural gouge: Application to the miocene sierra mazatán detachment fault, sonora, mexico. *Journal of Structural Geology*, *30*(4), 525–538.

Heldal, T. (1992). Naturstein i sør-norge: Befaring av grimstad og herefoss granitt, aust-agder.

Kelley, S. (2002a). Excess argon in k–ar and ar–ar geochronology. *Chemical Geology*, *188*(1-2), 1–22.

Kelley, S. (2002b). K-ar and ar-ar dating. *Reviews in Mineralogy and Geochemistry*, *47*(1), 785–818.

Ksienzyk, A. K., Wemmer, K., Jacobs, J., Fossen, H., Schomberg, A. C., Süssenberger, A., Lünsdorf, N., & Bastesen, E. (2016). Post-caledonian brittle deformation in the bergen area, west norway: Results from k–ar illite fault gouge dating. *Norwegian Journal of Geology*, *96*(3), 275–299.

Li, H., You, D., Han, J., Qian, Y., Sha, X., & Xi, B. (2020). The origin of fluid in calcite veins and its implications for hydrocarbon accumulation in the shunnan-gucheng area of the tarim basin, china. *Journal of Natural Gas Geoscience*, *5*(6), 341–353.

Lindanger, M., Gabrielsen, R. H., & Braathen, A. (2007). Analysis of rock lenses in extensional faults. *Norwegian Journal of Geology/Norsk Geologisk Forening*, *87*(4).

Mansfield, C., & Cartwright, J. (2001). Fault growth by linkage: Observations and implications from analogue models. *Journal of Structural Geology*, *23*(5), 745–763.

Masuda, K., Arai, T., & Takahashi, M. (2019). Effects of frictional properties of quartz and feldspar in the crust on the depth extent of the seismogenic zone. *Progress in Earth and Planetary Science*, *6*, 1–8.

Mulch, A., Cosca, M., Andresen, A., & Fiebig, J. (2005). Time scales of deformation and exhumation in extensional detachment systems determined by high-spatial resolution in situ uv-laser 40ar/39ar dating. *Earth and Planetary Science Letters*, *233*(3-4), 375–390.

Mulch, A., & Cosca, M. A. (2004). Recrystallization or cooling ages: In situ uv-laser 40ar/39ar geochronology of muscovite in mylonitic rocks. *Journal of the Geological Society*, *161*(4), 573–582.

Nesse, W. D. (2012). *Introduction to mineralogy*. Oxford Univ. Press.

Nilssen, B. (1961). Noen geologiske undersøkelser av herefossgraniten.

Nilssen, B., & Smithson, S. B. (1965). Studies of the precambrian herefoss granite. *Norsk Geologisk Tidskrift*, 45–367.

Odinsen, T., Reemst, P., Beek, P. V. D., Faleide, J. I., & Gabrielsen, R. H. (2000). Permo-triassic and jurassic extension in the northern north sea: Results from tectono-stratigraphic forward modelling. *Geological Society, London, Special Publications*, *167*(1), 83–103.

Ozkaya, S. I., & Richard, P. D. (2006). Fractured reservoir characterization using dynamic data in a carbonate field, oman. *SPE Reservoir Evaluation & Engineering*, *9*(03), 227–238.

Parneix, J., Beaufort, D., Dudoignon, P., & Meunier, A. (1985). Biotite chloritization process in hydrothermally altered granites. *Chemical Geology*, *51*(1-2), 89–101.

Pevear, D. R. (1999). Illite and hydrocarbon exploration. *Proceedings of the National Academy of Sciences*, *96*(7), 3440–3446.

Plotnick, R. (1999). Habitat of llandoverian-lochkovian eurypterids. *World and Regional Geology*, 106–131.

Plümper, O., & Putnis, A. (2009). The complex hydrothermal history of granitic rocks: Multiple feldspar replacement reactions under subsolidus conditions. *Journal of Petrology*, *50*(5), 967–987.

Rønning, K. J., Bruton, D. L., Harper, D. A., Høyberget, M., Maletz, J., & Nakrem, H. A. (2020). A cambrian-ordovician boundary section in the rafnes-herøya submarine tunnel, skien-langesund district, southern norway. *Norwegian Journal of Geology/Norsk Geologisk Forening*, *100*(1).

Rotevatn, A., Jackson, C. A.-L., Tvedt, A. B., Bell, R. E., & Blækkan, I. (2019). How do normal faults grow? *Journal of Structural Geology*, *125*, 174–184.

Scheiber, T., & Viola, G. (2018). Complex bedrock fracture patterns: A multipronged approach to resolve their evolution in space and time. *Tectonics*, *37*(4), 1030–1062.

Scholz, C., Dawers, N., Yu, J.-Z., Anders, M., & Cowie, P. (1993). Fault growth and fault scaling laws: Preliminary results. *Journal of Geophysical Research: Solid Earth*, *98*(B12), 21951–21961.

Scholz, C. H. (1998). Earthquakes and friction laws. *Nature*, *391*(6662), 37–42.

Schwartz, G. M. (1958). Alteration of biotite under mesothermal conditions. *Economic Geology*, *53*(2), 164–177.

Shipton, Z., & Cowie, P. (2001). Damage zone and slip-surface evolution over μm to km scales in high-porosity navajo sandstone, utah. *Journal of Structural Geology*, *23*(12), 1825–1844.

Shipton, Z. K., Soden, A. M., Kirkpatrick, J. D., Bright, A. M., & Lunn, R. J. (2006). How thick is a fault? fault displacement-thickness scaling revisited.

Sibson, R. (1977). Fault rocks and fault mechanisms. *Journal of the Geological Society*, *133*(3), 191–213.

Smithson, S. B. (1963). Granite studies i. a gravity investigation of two precambrian granites in south norway.

Sørensen, B. E. (2015). Tgb4125 mineralogi Øvingskompendium.

Tartaglia, G., Viola, G., van der Lelij, R., Scheiber, T., Ceccato, A., & Schönenberger, J. (2020). "brittle structural facies" analysis: A diagnostic method to unravel and date multiple slip events of long-lived faults. *Earth and Planetary Science Letters*, *545*, 116420.

Torgersen, E., Redfield, T. F., Svendby, K., & Fabia, K. (2021). Hva skal vi med et lineamentkart?

Torgersen, E., Viola, G., Zwingmann, H., & Henderson, I. H. (2015). Inclined k–ar illite age spectra in brittle fault gouges: Effects of fault reactivation and wall-rock contamination. *Terra Nova*, *27*(2), 106–113.

Torgersen, E., Viola, G., Zwingmann, H., & Harris, C. (2014). Structural and temporal evolution of a reactivated brittle–ductile fault–part ii: Timing of fault initiation and reactivation by k–ar dating of synkinematic illite/muscovite. *Earth and Planetary Science Letters*, *410*, 212–224.

Turner, S. (1999). Early silurian to early devonian thelodont assemblages and their possible ecological significance. *WORLD AND REGIONAL GEOLOGY*, 42–78.

Viola, G., Torgersen, E., Mazzarini, F., Musumeci, G., van der Lelij, R., Schönenberger, J., & Garofalo, P. S. (2018). New constraints on the evolution of the inner northern apennines by k-ar dating of late miocene-early pliocene compression on the island of elba, italy. *Tectonics*, *37*(9), 3229–3243.

Walsh, J., Nicol, A., & Childs, C. (2002). An alternative model for the growth of faults. *Journal of Structural Geology*, *24*(11), 1669–1675.

Worsley, D., Aarhus, N., Bassett, M. G., Howe, M., Mørk, A., & Olaussen, S. (1983). *The silurian succession of the oslo region*. Universitetsforl.

Ziegler, P. (1992). North sea rift system. *Tectonophysics*, *208*(1-3), 55–75.

Zwingmann, H. (2014). Clays and glauconites (k-ar/ar-ar). *Encyclopedia of Scientific Dating Methods*, 1–10.